2016-09

Microwave-photonic architecture for direction finding of LPI emitters: front-end analog circuit design and component characterization

Tan, Chew K.

Monterey, California: Naval Postgraduate School

NAVAL POSTGRADUATE SCHOOL

MONTEREY, CALIFORNIA

THESIS

MICROWAVE-PHOTONIC ARCHITECTURE FOR DIRECTION FINDING OF LPI EMITTERS: FRONT-END ANALOG CIRCUIT DESIGN AND COMPONENT CHARACTERIZATION

by

Chew K. Tan

September 2016

Thesis Advisor: Phillip E. Pace
Second Reader: David C. Jenn

Approved for public release. Distribution is unlimited.

THIS PAGE INTENTIONALLY LEFT BLANK

REPORT DOCUMENTATION PAGE			*Form Approved OMB No. 0704-0188*

1. AGENCY USE ONLY *(Leave blank)*	**2. REPORT DATE** September 2016	**3. REPORT TYPE AND DATES COVERED** Master's thesis

4. TITLE AND SUBTITLE
MICROWAVE-PHOTONIC ARCHITECTURE FOR DIRECTION FINDING OF LPI EMITTERS: FRONT-END ANALOG CIRCUIT DESIGN AND COMPONENT CHARACTERIZATION

5. FUNDING NUMBERS

6. AUTHOR(S) Chew K. Tan

7. PERFORMING ORGANIZATION NAME(S) AND ADDRESS(ES)
Center for Joint Services Electronic Warfare
Naval Postgraduate School
Monterey, CA 93943-5000

8. PERFORMING ORGANIZATION REPORT NUMBER

9. SPONSORING /MONITORING AGENCY NAME(S) AND ADDRESS(ES)
Consortium for Robotics and Unmanned Systems Education and Research (CRUSER) / Monterey, CA

10. SPONSORING / MONITORING AGENCY REPORT NUMBER

11. SUPPLEMENTARY NOTES The views expressed in this thesis are those of the author and do not reflect the official policy or position of the Department of Defense or the U.S. Government. IRB number ____N/A____.

12a. DISTRIBUTION / AVAILABILITY STATEMENT
Approved for public release. Distribution is unlimited.

12b. DISTRIBUTION CODE

13. ABSTRACT (maximum 200 words)

Direction finding (DF) systems are critical components in electronic warfare intercept receivers. Many existing radio frequency DF techniques use a non-linear frequency down-conversion process that generates spurious frequencies that can hide the signals-of-interest. In addition, these systems suffer from a limited bandwidth and poor resolution (e.g., > 2°). To overcome these limitations, a miniature microwave-photonic phase-sampling DF technique is investigated in this thesis. This front-end design uses a combination of integrated optical Mach-Zehnder phase detectors to measure the emitter's phase difference with the largest baseline being 23 cm. The front-end components were characterized to ensure accuracy in the resolved angle-of-arrival (AOA). The front-end design was constructed to be modular in order to facilitate testing and verification of analog components accuracy. Signal processing with a class IV laser required particular attention to ensure that any stray radiation or leakage was isolated. Testing with low probability of intercept (LPI) waveform modulation consisted of using a linear frequency-modulated continuous wave (FMCW) and a phase coded P4 modulation, both at 2.4 GHz, in an anechoic chamber. Measurements were taken to quantify the DF receiver sensitivity was $\delta_R = -62.96$ dBm. It was demonstrated that the system was capable of estimating the AOA for the FMCW signal with a root-mean square (RMS) error of 0.29° at < 1° resolution and a P4 modulation RMS error of 0.32° at <1° resolution.

14. SUBJECT TERMS Direction finding, DF, 1dB compression, photonics, DE-MZM, Mach-Zehnder, direction of arrival, AOA			**15. NUMBER OF PAGES** 125
			16. PRICE CODE
17. SECURITY CLASSIFICATION OF REPORT Unclassified	**18. SECURITY CLASSIFICATION OF THIS PAGE** Unclassified	**19. SECURITY CLASSIFICATION OF ABSTRACT** Unclassified	**20. LIMITATION OF ABSTRACT** UU

NSN 7540-01-280-5500

Standard Form 298 (Rev. 2-89)
Prescribed by ANSI Std. 239-18

THIS PAGE INTENTIONALLY LEFT BLANK

Approved for public release. Distribution is unlimited.

MICROWAVE-PHOTONIC ARCHITECTURE FOR DIRECTION FINDING OF LPI EMITTERS: FRONT-END ANALOG CIRCUIT DESIGN AND COMPONENT CHARACTERIZATION

Chew K. Tan
Military Expert 6, Republic of Singapore Navy
B.E. (Hons), University of New South Wales, 2002

Submitted in partial fulfillment of the
requirements for the degree of

MASTER OF SCIENCE IN ELECTRICAL ENGINEERING

from the

NAVAL POSTGRADUATE SCHOOL
September 2016

Approved by: Phillip E. Pace
Thesis Advisor

David C. Jenn
Second Reader

R. Clark Robertson
Chair, Department of Electrical and Computer Engineering

THIS PAGE INTENTIONALLY LEFT BLANK

ABSTRACT

Direction finding (DF) systems are critical components in electronic warfare intercept receivers. Many existing radio frequency DF techniques use a non-linear frequency down-conversion process that generates spurious frequencies that can hide the signals-of-interest. In addition, these systems suffer from a limited bandwidth and poor resolution (e.g., $>$ 2°). To overcome these limitations, a miniature microwave-photonic phase-sampling DF technique is investigated in this thesis. This front-end design uses a combination of integrated optical Mach-Zehnder phase detectors to measure the emitter's phase difference with the largest baseline being 23 cm. The front-end components were characterized to ensure accuracy in the resolved angle-of-arrival (AOA). The front-end design was constructed to be modular in order to facilitate testing and verification of analog components accuracy. Signal processing with a class IV laser required particular attention to ensure that any stray radiation or leakage was isolated. Testing with low probability of intercept (LPI) waveform modulation consisted of using a linear frequency-modulated continuous wave (FMCW) and a phase coded P4 modulation, both at 2.4 GHz, in an anechoic chamber. Measurements were taken to quantify the DF receiver sensitivity was $\delta_R = -62.96$ dBm. It was demonstrated that the system was capable of estimating the AOA for the FMCW signal with a root-mean square (RMS) error of 0.29° at $<$ 1° resolution and a P4 modulation RMS error of 0.32° at $<$1° resolution.

THIS PAGE INTENTIONALLY LEFT BLANK

TABLE OF CONTENTS

LIST OF FIGURES

THIS PAGE INTENTIONALLY LEFT BLANK

LIST OF TABLES

THIS PAGE INTENTIONALLY LEFT BLANK

LIST OF ACRONYMS AND ABBREVIATIONS

A/D	analog-to-digital
AOA	angle-of-arrival
CW	continuous wave
DC	direct current
DE-MZM	dual-electrode Mach-Zehnder modulator
DF	direction finding
DFB	distributed feedback
ED	envelope detector
E/O	electrical-to-optical
EM	electromagnetic
FMCW	frequency-modulated continuous wave
FOV	field of view
InGaAs	indium gallium arsenide
LiNbO3	lithium niobate
LNA	low noise amplifier
LPI	low probability of intercept
MLP	multilayer perceptron
MWP	microwave-photonic
MZM	Mach-Zehnder modulator
NPS	Naval Postgraduate School
O/E	optical-to-electrical
PD	photodetector
R&S	Rohde & Schwarz
RF	radio frequency
RMS	root-mean square
RSNS	robust symmetrical number system
TDOA	time-difference-of-arrival
VVA	voltage variable attenuator

THIS PAGE INTENTIONALLY LEFT BLANK

ACKNOWLEDGMENTS

I would like to thank my thesis advisor, Professor Phillip E. Pace, for his guidance and patience in imparting his valuable knowledge to me, and always steering me to the right path whenever I faced challenges in the thesis. He would always find time to meet up and discuss my progress despite his busy work schedule. His enthusiasm and passion in research have been an inspiration to motivate me in giving my best in whatever I do.

To the three amazing and experienced laboratory directors, Paul Buczynski, Bob Broadston, and Dr. James Calusdian, they have certainly helped and encouraged me to overcome most of the hardware issues confidently. There is never a hardware defect too huge for them to solve. They provided resources and effort in coaching me on the use of test equipment for measurement and data collection.

These results would not be possible without the use of the Rohde & Schwarz instrumentation and the support from Mr. Berry Carone and Mr. P.B. Balasubramanium. I would like to thank them for their trust and faith in lending us the latest test equipment that my research required.

This work was funded by the Consortium for Robotics and Unmanned Systems Education and Research (CRUSER), Naval Postgraduate School (NPS). With their support, we were able to replace components with better specifications, which resulted in improved system performances.

Special mention goes to my thesis partner, Mr. Ong Chee Kiong, who spent countless hours with me in the laboratory to fix up the hardware and the time in data collection in the anechoic chamber. My partner was always there for me whenever I needed help for this thesis or schoolwork.

Finally, I would like to express my deepest appreciation to my lovely wife, Jacqueline Lu. You have always been my pillar of support when the going gets tough. You were understanding whenever I had to work late in the laboratory, encouraging me whenever I faced a stumbling block during the course of my thesis.

THIS PAGE INTENTIONALLY LEFT BLANK

I. INTRODUCTION

A. DIRECTION FINDING

Direction finding (DF) is used to determine the angle-of-arrival (AOA) of radio frequency (RF) waves by measuring and processing their electromagnetic (EM) parameters. There are widespread applications for DF, such as navigation for vessels and aircraft, determining interference by cellular network operators, and tracking of criminals by law enforcement. For military applications, DF is used for detecting potential threats and for electronic intelligence (ELINT) purposes.

A typical DF system is comprised of an antenna array, RF receiver chain, and signal processor unit. Several DF techniques have been developed in the past to obtain DF information in computing the AOA. The type of DF technique employed influences the complexity of system design, cost of construction, and accuracy. In the following discussion, commonly used DF techniques are reviewed.

1. Time-Difference-of-Arrival DF

Time-difference-of-arrival (TDOA) uses the principle of measuring the differences in the time-of-arrival for a signal to reach different receiving antennas, usually placed several kilometers apart. If the antennas are placed too near to one another, DF computation is inaccurate since the time-of-arrival at the antennas is approximately the same. In addition, other parameters such as the timing accuracy in the receiving system and time synchronization with other receiving sites has an adverse effect of the accuracy of the AOA computation. In advanced TDOA systems, geolocation and clock information from a global positioning system (GPS) are incorporated for synchronization to achieve more accurate DF results [1].

2. Amplitude DF

Amplitude comparison DF systems can be implemented using single or multiple directional antenna elements pointing in various directions. The number of antenna elements required depends on the accuracy and field-of-view (FOV) requirement. This

method measures the strength of the signal amplitudes at the respective antenna elements in estimating the AOA of the emitter [2]. While amplitude DF is the simplest system to implement, the main drawback is its lack of accuracy. Measurements have been reported for an amplitude DF system for receiving signals in the 8- to 18-GHz frequency range with an AOA accuracy of 5° root-mean square (RMS) [3].

3. Phase Interferometry DF

For this technique, several antenna elements are placed at an appropriate spacing and one of the antenna elements serves as a reference while the remaining elements are configured as measurement channels. The AOA of an emitter can be estimated using the phase difference measured between a measurement antenna with respect to the reference antenna [4]. Two different types of phase interferometry methodologies can be implemented. With the antenna elements placed along a straight line or in a circular position, the method is known as linear or circular phase interferometry, respectively [5].

B. MICROWAVE PHOTONICS IN RF DESIGN

The use of photonic devices in telecommunications is common, and research into the applications of microwave-photonic (MWP) in front-end DF system design is becoming more prevalent. Advancement in photonics technology has enabled new techniques in signal processing such as photonic analog-to-digital conversion, microwave photonic delay-line filtering, and optical mixing with direct or external modulation [6]. The advantages of incorporating a MWP design into a RF design are that photonic devices are capable of operating at high frequencies with wide bandwidth and help reduce the size, weight, and power in the overall design of the RF system [7]. In addition, the use of fiber optic cables helps reduce electromagnetic interference from the external environment. In addition, these cables have low attenuation loss [6].

MWP is also being explored for military applications, such as electronic warfare (EW). For a typical EW receiver, DF can be obtained through the use of a long baseline technique by having several antennas placed a great distance apart. The AOA of the emitter can be computed by measuring the phase difference between the different receiving antennas [8]. The use of conventional coaxial cables, however, can result in a

high overall non-linear attenuation in the system, since attenuation from the cables is frequency dependent. As such, the accuracy of the AOA calculation for millimeter wave threats (i.e., 30 GHz) is poor. With the use of a microwave photonic link, consisting of optical components and optical fiber, the attenuation in the system can be minimized for more accurate results. The use of advanced photonic signal processing techniques helps enable a lighter and smaller front-end receiver design, which is essential for a space-constrained airborne system [8].

Research programs were initiated to further develop better designs for key optical components in a microwave photonic link. It was reported that a distributed feedback (DFB) laser was designed to produce 200-mW output power with a low relative noise intensity of −164 dB/Hz. A newly developed photodiode with an output power of 0.75 W and minimum distortion has also been demonstrated [9]. With the superior performance reported, optical components are being considered more seriously for receiver design and are now being deployed in military systems.

C. WIDEBAND MICROWAVE-PHOTONIC DF CONCEPT

The feasibility of incorporating photonic components into a phase-sampled linear interferometry DF receiver to estimate the AOA of an emitter has been demonstrated using a bench test setup [10]. The signals received at both the reference and measurement antenna were sent to the respective arm of a dual electrode Mach-Zehnder modulator (DE-MZM). The RF signals at the electrodes changed the index of refraction of each DE-MZM waveguide. A 1550-nm continuous wave (CW) laser was used as the DE-MZM input source. The change in the index of refraction changed the corresponding propagation of the laser signal used as the input. The magnitude of the optical signal at the output of the DE-MZM corresponds to the phase difference between the two channels. The phase difference is converted to an electrical signal using a photodetector (PD). The optical mixing of the RF signals from the reference and measurement channel using an optical DE-MZM and externally modulated CW laser carrier eliminates the need for RF /intermediate frequency (IF) down-conversion.

The bench test setup incorporated an antenna array composed of four antenna elements, with one reference and three measurement channels. The use of three measurement channels made it possible to achieve a small baseline while resolving the ambiguities from the RF signals received. The ambiguities were resolved using a robust symmetrical number system (RSNS) encoding technique. The RSNS post processing of the phase-difference output was used to compute the AOA [10].

A mock-up photonics DF system was subsequently constructed, and training of a multi-layer perceptron (MLP) network was used for post processing of the phase-difference data to determine the AOA. The system was tested in the anechoic chamber using a 2.4-GHz CW signal, and test results showed that the system was able to detect the AOA with 1° resolution over a 180° field-of-view (FOV) [11].

To address these limitations and examine the application for a tactical signal environment, our research objective was to configure the architecture to measure the AOA of low probability of intercept (LPI) signals. As the detection of LPI signals is challenging, hardware modifications to the previous design had to be carried out to improve the sensitivity of the system. These improvements include modifications for key RF parameters such as system gain, dynamic range, and reducing the overall losses in the design, which is critical for the receiver front-end. In addition, the use of MLP for post processing in the previous design required several sets of data to be recorded in order to train the system for pattern recognition before the AOA could be determined. A new, alternate approach for the back-end processing is also explored to calculate the AOA and reduce the time required for data collection.

D. PRINCIPAL CONTRIBUTIONS

In this thesis, the research and development required to design and test the MWP DF system front-end are documented. The DF system back-end was designed and tested in a companion thesis [12]. This DF system research and development required working closely during the front-end and back-end system integration stage to ensure accurate EM parameter measurements. The seamless integration resulted in a robust and modular hardware construction that is rugged enough for future measurements in a tactical

environment. In addition, the new system design must be stable, both physically and performance wise, to produce consistent data and results.

Initial work consisted of gaining a thorough understanding of DF receiver theory through research and self-directed reading. This was followed by acquiring knowledge of MWP and the principles of electrical-to-optical (E/O) and optical-to-electrical (O/E) conversion for MWP applications. This enabled comprehension of the wideband MWP DF concept developed in [10] and the hardware implementation developed in [11]. Since this thesis research involved hardware that had limited documentation, getting hands-on experience with the antenna system elements enhanced familiarity with the system functions. In addition, a better understanding of the system limitations was obtained before attempting any modification to the hardware.

The DF system development was carried out in a systematic, two-stage process. The first stage, which was conducted in the laboratory using direct signal injection, involved the measurement of the output response of every component used in the system. After setting up the test equipment to give the correct measurement, the measurement results were correlated with the component specifications as well as with theoretically expected results. Much of the initial time was spent in characterizing the performance of each component due to difficulty in accessing the component. This was a result of poor placement of components in the system. Since there is little knowledge of the photonic components being used, much effort was invested into understanding how, for example, an DE-MZM works and how optical measurement should be carried out.

The second stage involved reproducing the results in an anechoic chamber reported in [11]. To tabulate the measurement results, LabVIEW was used. This was the software used previously to record and organize the raw data. Another challenge was to determine how to rotate the pedestal located in the anechoic chamber in order to simulate a 180° FOV for the DF measurement.

As the mock-up MWP DF system was huge, heavy, and unstable, the entire system vibrated as the pedestal rotated. This caused numerous erroneous recordings as the vibrations affected the optical cables and the interconnections between the E/O and

O/E conversion paths. Several RF hardware component failures required transportation of the entire system back to the laboratory for troubleshooting and repair. To obtain the correct sensitivity of the receiver, the low noise amplifier (LNA) gain control had to be adjusted precisely, where the procedure also was not well documented. This caused the measurement results to be different from what were previously presented in [11]. Further investigations concluded that the LNAs had been operating incorrectly in the 1-dB compression region.

The first major contribution of this work was the characterization of all hardware components used in the previous mock-up DF photonics antenna design and the replacement of components with those having better specifications so as to improve the overall sensitivity and gain of the system. Unnecessary components were removed to streamline the design, which further reduced the overall size and weight of the system. Measurements on the DE-MZMs were carried out to establish the required bias voltage for the DE-MZMs to operate in the linear region.

The second major contribution was reconstructing the hardware to improve the overall handling and safety while enhancing both hardware and performance stability. This contribution enabled the hardware to be transported easily for field testing and measurements to be conducted. The entire process took several months due to the integration and testing as well as troubleshooting hardware failures along the way. The performance measurement of a single path channel was carried out in the laboratory, and the output response at different stages of the receiver chain was fully documented. This served as a baseline for future reference. In addition, detailed experimental testing was carried out to establish the 1-dB compression region of the LNAs. The procedure and results are clearly documented in this thesis.

The final major contribution was investigation of the MWP DF system's ability to detect LPI signals in a controlled environment. LPI signals were generated with the Rohde & Schwarz SMW vector signal generator. The programming of the equipment to generate the required complex signals was not straightforward and time had to be invested in learning its functionalities. Detailed screenshots of the signal flow were

captured and are presented. This enabled us to understand how the system performed at the different stages in the receiver chain and to offer recommendations for future work.

E. THESIS OUTLINE

This thesis is not just a follow-on investigation but a description of the development of an innovative microwave-photonic phase sampling linear DF architecture. Due to the scale and complexity of the design, the research was divided into two parts. The design, development, and testing efforts of the front-end microwave photonics circuit design and the system integration with the photonics back-end post processing in [12] is described. Once the entire modified MWP DF system was integrated, performance measurements using LPI signals were conducted.

The initial concept, previous design and its limitations, and the objective of the necessary hardware modifications are discussed in Chapter II. The overall system architecture and functional description are presented in Chapter III. In Chapter IV, the detailed setup and performance measurements of individual components are documented. In Chapter V, a detailed description of how a DE-MZM works and how it is used to compute the phase difference between two channels is provided. The integration of the components to form each functional block of the architecture are discussed in Chapter VI. Also included is the expected output at the various points in the integrated channel and the measured results that were captured. The importance of the LNA cascade in providing sufficient gain for optimal detection of incident signals is also discussed. The test environment, calibration process of system prior to measurement, and how the integrated photonics DF system functioned are described in Chapter VII. Screenshots from the test equipment at the various measuring points were also analyzed and presented in this chapter. Conclusions from this thesis and recommendations for future research on MWP DF design concepts are given in Chapter VIII.

THIS PAGE INTENTIONALLY LEFT BLANK

II. PREVIOUS DESIGNS AND MODIFICATIONS

An overview of the previous MWP DF system and the necessary system modifications to the previous hardware design are discussed in this thesis. These improvements help stabilize the overall performance of the system and offer additional access points for collection of more accurate measurements that enhance our understanding of the system.

A. PREVIOUS DESIGN

The concept of a MWP DF system in detecting the AOA of an emitter was researched, followed by the development of a bench test system. The bench test system was experimentally tested to prove its feasibility. A mock-up system was subsequently developed to further validate this concept in the anechoic chamber.

1. Bench Test Version

The idea of a four-antenna element photonics DF system using RSNS was proposed and validated using simulations. Subsequently, a simple system was configured and experimentally bench tested. The block diagram for the bench test equipment is shown in Figure 1. A sinusoidal CW 2.4-GHz signal was injected directly through the system, and the phase shift at each antenna was artificially created using manual phase shifters. The signals were routed to the DE-MZM, with the reference signal connected to one electrode and a measurement channel to the other electrode [10]. A high power distributed feedback CW laser with 1550-nm wavelength was then sent into the DE-MZM to be externally modulated by the two signals at the electrodes. Since the DE-MZM produced an optical output, it was converted into an electrical signal using an indium gallium arsenide (InGaAs) photo detector (PD) before further processing.

A DC blocking capacitor was used to remove any DC components from the PD's output so that the modulated signals could be extracted. Since the phase difference between the reference and measurement channel was embedded in the signal's amplitude, the signal was passed through a system of two LNAs to achieve the required

amplification. After the amplification, the carrier in the signal was removed after it passed through an envelope detector (ED). In addition, the ED extracted the signal's amplitude to produce a corresponding voltage level. This voltage level was essentially the phase difference between the reference and measurement channel. As the voltage was small due to the conversion process, the signal was further amplified using an instrumentation amplifier before analog-to-digital conversion for post-digital signal processing. The AOA was calculated in the field-programmable gate array (FPGA).

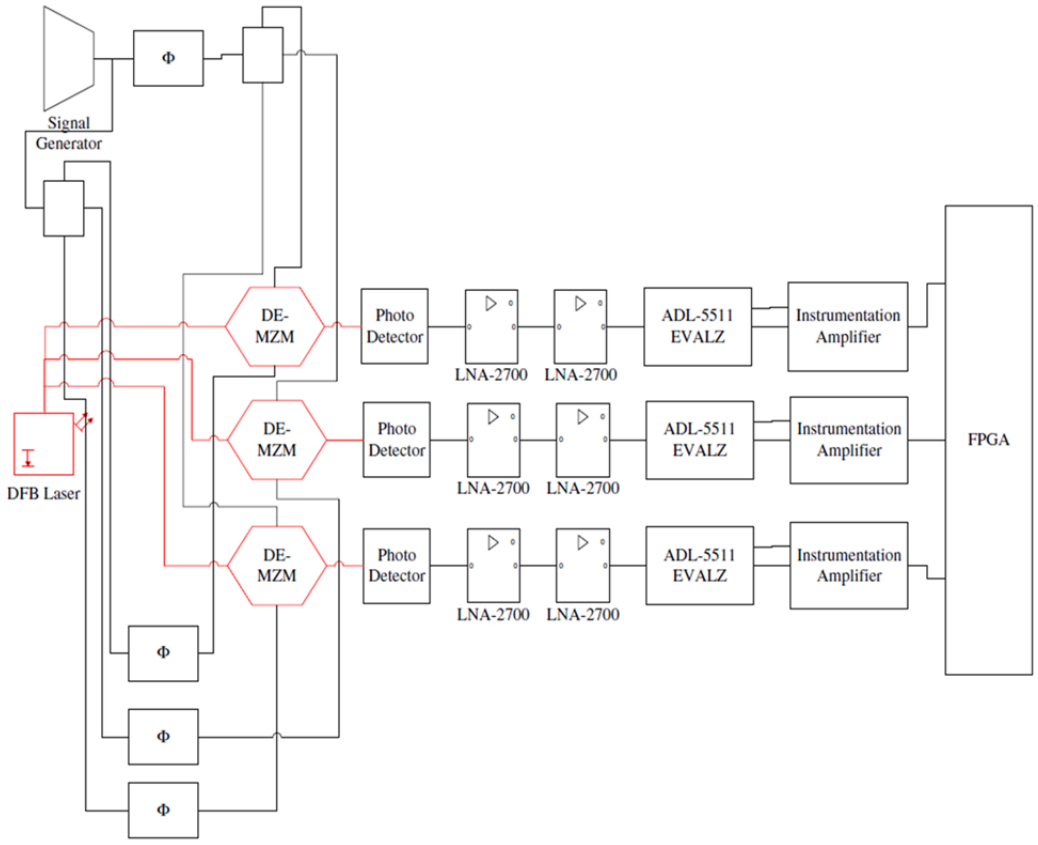

Figure 1. Block Diagram of Bench Test System. Source: [10].

The bench test setup was experimentally tested, and it was concluded that the setup was capable of estimating the AOA of a CW signal [10]. These findings were the inspiration for an actual DF antenna to be built for further research.

2. Mock-Up Microwave-Photonic DF System

The bench test hardware used in [10] was modified to emulate a DF system that could be used for receiving actual RF transmissions and a back-end processing system to collect, compute, and process raw data to quantify the concept further. A mock-up MWP DF system was eventually constructed, as shown in Figure 2, and the detailed explanations of the required modifications made are described in [11]. The complete system underwent testing using a 2.4-GHz CW signal in the anechoic chamber located at the Naval Postgraduate School (NPS). Numerous sets of data were collected over a period of time, and post processing was carried out separately using the concept of neural networks. The research concluded that the mock-up photonics DF architecture combining neural network back-end processing was capable of determining the AOA of a CW signal with a mean error of 0.5°.

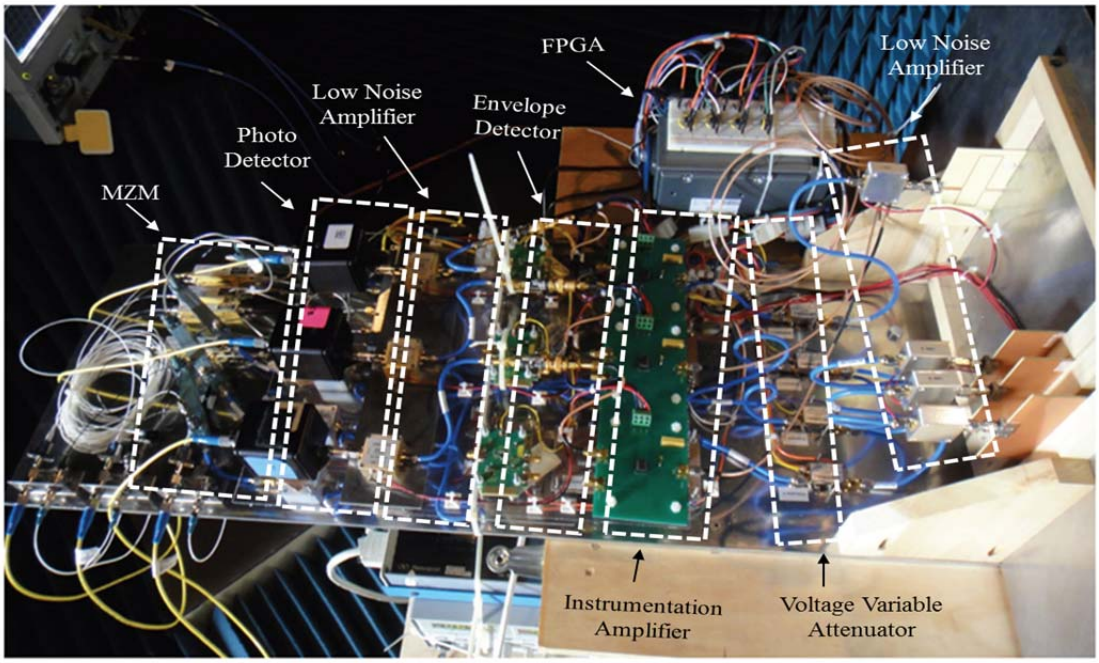

Figure 2. Mock-Up MWP DF System from Previous Design. Source: [11].

B. SYSTEM MODIFICATIONS

As seen from Figure 2, all the hardware components from the previous design were mounted onto one large sheet of aluminum (0.3 m × 0.9 m). The first consideration for using an entire sheet of aluminum was to improve the thermal conductivity so that increasing temperature from the components could dissipate during system tests and so that optical modulation, which is sensitive to temperature, would not cause signal instability. The next consideration was to provide a common grounding point for all components; however, the entire system was bulky in size and physical handling was cumbersome for transportation and when measurements were carried out. Apart from that, when the system was mounted on a pedestal, located in the anechoic chamber, half the aluminum sheet had no support, and the substantial weight of all components mounted on top caused the aluminum sheet to warp. This resulted in the system vibrating whenever the pedestal rotated during measurements. Several components included in the design, which were initially thought to be useful for calibrating the system for better measurement results, were also found to be unnecessary.

The mock-up system design was reexamined and redesigned. Hardware modifications were successfully carried out after several months of effort, and the existing photonics DF system is shown in Figure 3.

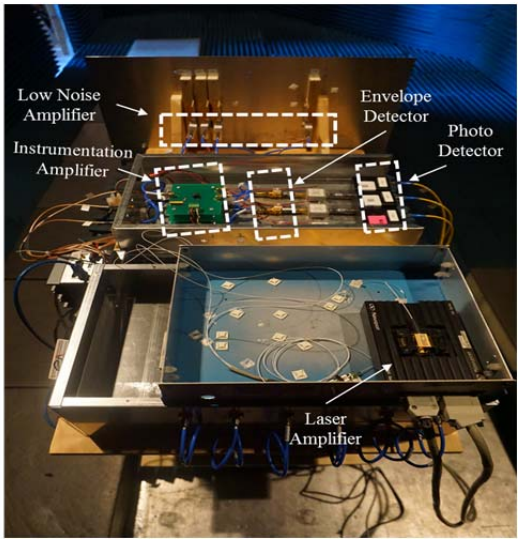

Figure 3. Improved Design of Photonics DF System

The modified photonics DF system was redesigned to achieve the objectives described in the following subsections.

1. Modular Design

The system was redesigned and assembled into four aluminum boxes based on their functionalities. Having a modular design aids in isolating and troubleshooting the circuitry. When a defective component is isolated, only the particular box where the defective component is housed is required to be transported to the laboratory for repair. Removal of a defective component from within the box is also much easier, as compared to the previous design where the entire aluminum sheet had to be lifted up in order to unscrew the component from its position.

For the performance evaluation of each signal path, signals could be tapped and displayed on measurement equipment using the connectors on each box.

2. Improved Safety in Operating the DF System

The operation of the photonics DF system requires the use of Class 4 laser radiation, with output power of greater than 500 mW, operating at 1550 nm. Exposure to such laser radiation can result in permanent eye damage. This consideration motivated us to enclose the laser diode and optical cables in a separate box to prevent any stray laser radiation in the event of breakage in the optical cables.

3. Characterization of DF System

While the specifications for components can be found in data sheets, the information provided usually represents optimal performance measured in the ideal environment. Since all hardware components had to be removed from the previous design, the performance of each component was characterized and recorded at 2.4 GHz. With this data, we were able to trace individual signal paths and better understand the system performance. New components with better specifications were also introduced in the design, which helped further improve the sensitivity and performance of the entire DF system.

4. Removal of Unnecessary Components

In the previous design, it was found that erroneous phase shifts inherent to the system were introduced mostly due to mismatch of individual components and from the four-way power divider. To ensure accuracy of the data collection, phase shifters were included to calibrate the system during each measurement. The circuit design to control the phase shifters was complex, and the calibration process was time consuming. During the redesign process, we carried out measurements to try and establish the exact phase shifts expected; however, after several measurements and trials, we concluded that these phase shifts would not affect the eventual computation of AOA. This was because the phase shift inherent to each channel was consistent and did not change over time; therefore, at each AOA measurement, the same amount of phase shift in each channel was used to compute the exact AOA. As a result, the phase shifters were removed, resulting in an overall streamlined design with a reduced size.

5. Enabling Outfield Testing

By compartmentalizing the components into four aluminum boxes based on their functions, we could easily transport the hardware. Moving forward, this will facilitate outdoor or flight testing.

With the background of the previous designs described along with the necessary modifications to improve the system hardware, in the next chapter we discuss the new innovative system design and the signal flow paths through the DF system.

III. INNOVATIVE SYSTEM DESIGN

An overview of the new system design is provided in this chapter. In addition, a description of signal flow through the system provides an understanding of how the received RF waves at the antenna elements are converted to electrical signals and processed in the receiver chain for eventual conversion to digital signals for AOA processing. The block diagram of the redesigned photonics DF system is based on Figure 4. The system design can be viewed as three stages. The first stage comprises the antenna array, Box 1, and Box 2, which form the RF path. The second stage comprises Box 3, which forms the optical path. The last stage is Box 4, the analog-to-digital (A/D) conversion required for digital signals to be created and processed.

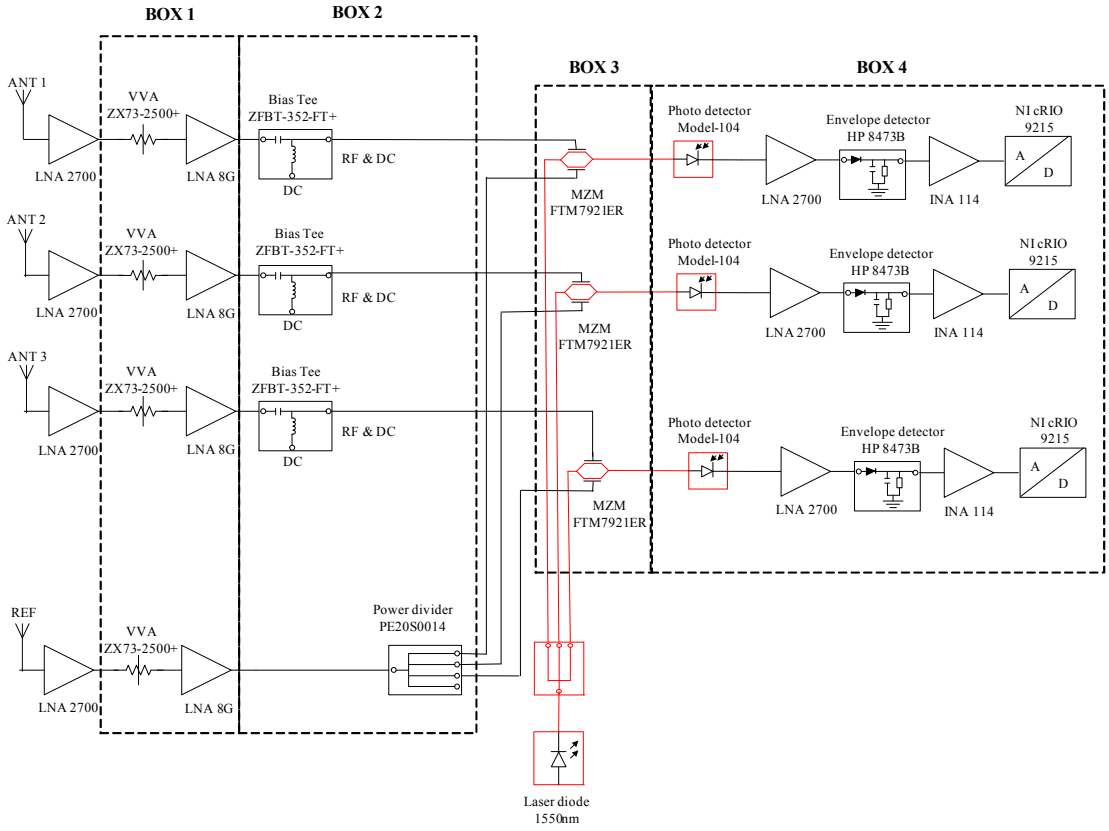

Figure 4. System Block Diagram of Modified Photonics DF System

A. RF SIGNAL PATH

The RF signal path (Box 1 and Box 2) is employed for converting the RF waves incident on the antenna elements into electrical signals. As the received signals are weak, typically in pW or mW, they undergo amplification in order to achieve a viable level prior to processing. Bias voltages are essential to operate the DE-MZM in the linear region for optimal performance. These bias voltages must be added to the signals prior to the electrodes. The detailed description of the DE-MZM is given in Chapter V.

1. Antenna Array

The front-end of the system is made up of the antenna array, which is used to convert RF electromagnetic (EM) waves into electrical signals. From [13], ambiguities in the AOA occur if the distance between adjacent pairs of interferometer elements is greater than $\lambda / 2$, where λ is the wavelength in meters and can be computed using $\lambda = c / f$, c is the speed of light (3×10^8 m/s), and f is the operating frequency in Hz; however, this can be resolved if an additional interferometer element is used. For the antenna design, we adopted an antenna array consisting of four, half-wave ($\lambda / 2$) dipole elements for a reference channel and channel 1, 2, and 3, as shown in Figure 5.

The performance of the antenna during measurement is affected by the surrounding environment, especially reflection of EM waves from the hardware mounted behind the antenna array. To minimize the effect of interference, the antenna array was mounted on a solid aluminum plate (0.3 m × 0.9 m) to act as a ground plane. Since most measurements were carried out at a frequency of 2.4 GHz, the size of the half-wave dipole is 6.25 cm. When the aluminum plate is large compared to the antenna size, it acts as an effective ground plane [14].

The AOA of an emitter can be established using the four array elements [4], [15]. The separation distance between each interferometer antenna element and the reference antenna was computed to be d_1 = 17.77 cm, d_2 = 20.0 cm, and d_3 = 22.85 cm based on the design concept of RSNS system and FOV requirement [10], [11].

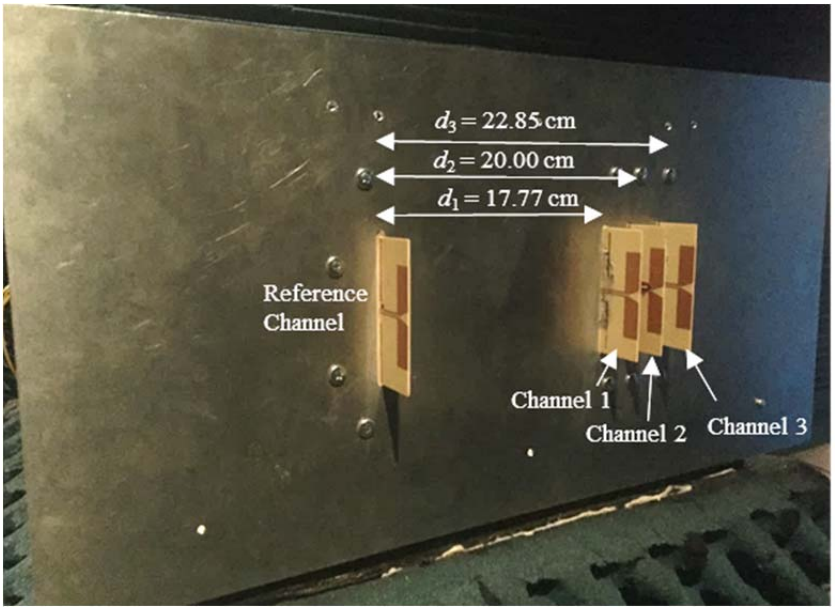

Figure 5. Use of Four Half-Wave Dipole Elements to Form the Antenna Array

In a receiver system, the received signals are typically very low in power, and it is desirable to amplify the signals as well as minimize the noise power introduced into the system. Cables connecting the antenna elements to the LNAs further reduce the signal level before any amplification due to cable insertion loss. The choice of LNAs should provide sufficient amplification yet possess a low noise figure; therefore, the antenna array is designed to minimize losses by directly coupling the antenna elements to the fixed gain LNAs as shown in Figure 6.

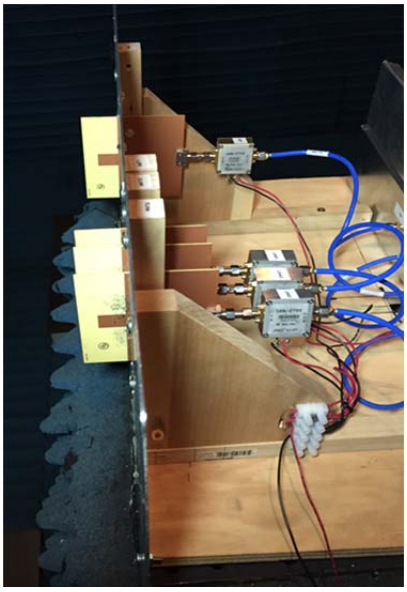

Figure 6. Antenna Array with LNAs Connected Directly to the Output of the Antenna Dipoles

2. Second Stage Signal Amplification

The amplified signals are connected to Box 1, which consists of voltage variable attenuators (VVA) and second stage LNAs to provide additional amplification. Box 1 is shown in Figure 7. The VVAs serve as a control mechanism to vary the gain for the cascade of fixed gain LNAs, and the detailed explanation for such a design consideration is presented in Chapter IV.

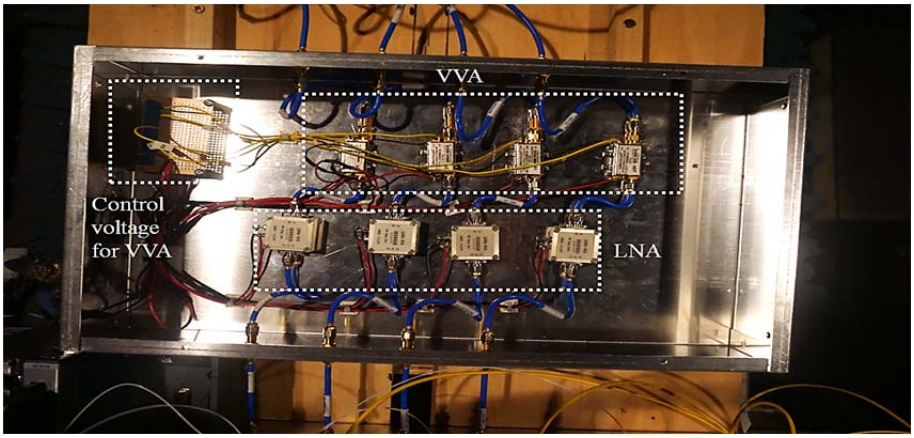

Figure 7. Box 1 Containing VVA and Second Stage LNA

3. Introduction of Bias Voltage

For Box 2, DC bias voltages are added to each of the three measurement channels by adjusting the bias-tee control. Each of the channel outputs is connected to one arm of the DE-MZM. The bias voltage is critical to operate the DE-MZM in the linear region for optimal performance. The reference channel is split into three output channels using a power divider, which is connected to the other arm of the DE-MZM. Box 2 is shown in Figure 8.

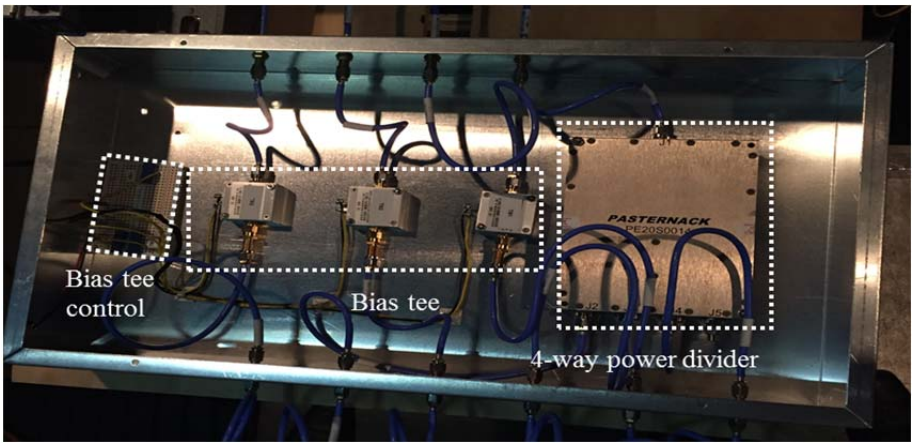

Figure 8. Box 2 Containing Four-Way Power Splitter and Bias Tee

B. OPTICAL SIGNAL PATH

The DE-MZMs are housed in Box 3, which is pictured in Figure 9. A high-power 1550 nm DFB laser generates the optical input to the three DE-MZMs. The laser intensity for each DE-MZM is externally modulated by the reference and measurement channels, which are supplied through the two electrodes. The optical output from the DE-MZM corresponds to the phase difference between the reference and the measurement channels.

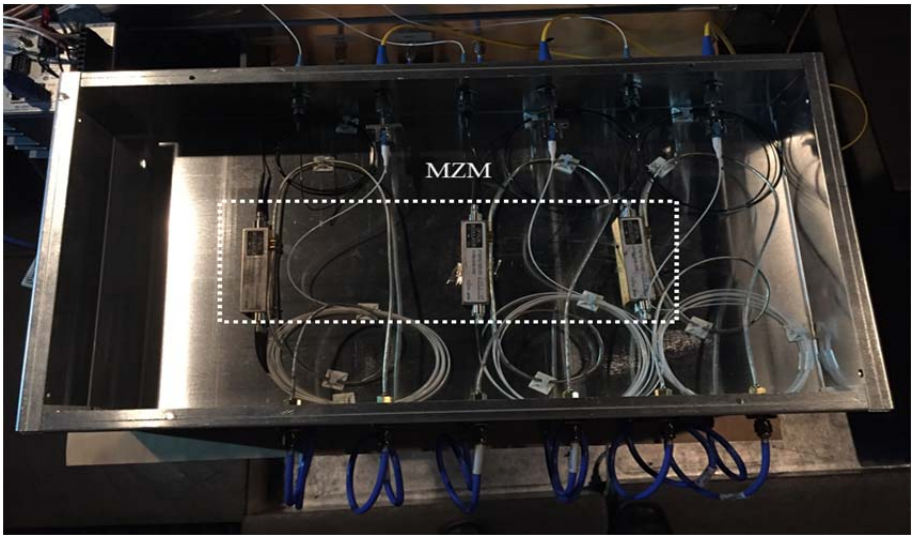

Figure 9. Box 3 Containing DE-MZMs

C. A/D CONVERSION

To further process the received signal, InGaAs photodetectors were used to convert the optical output from the DE-MZM into electrical signals. The signals were then passed through DC blocking capacitors to remove DC components since we are only interested in the phase difference which is embedded in the amplitude of the modulated signals. Amplification of the signal was required before extracting the high frequency carrier using the ED. The conversion process by the ED resulted in decreasing the signal amplitude, so a second stage of amplification was necessary. In addition, the output of the ED has an impedance of 1.3 $k\Omega$. As a result, the instrumentation amplifier (INA 114) was deliberately introduced to amplify the signals as well as carry out impedance matching to 50 Ω. Finally, the signals were sampled using CompactRIO, which has an input impedance of 50 Ω, before they are processed in a standalone computer [12]. The components required to convert the optical signal output of the DE-MZM to digital signals are housed in Box 4 as shown in Figure 10.

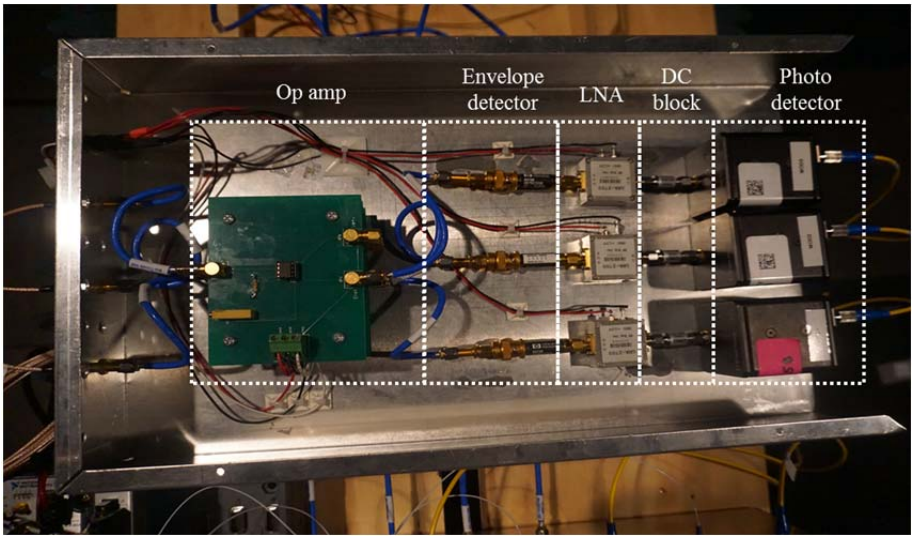

Figure 10. Box 4 Containing Components Required to Convert Optical to Digital Signals

With the understanding of the system architecture, the components used in the system and the performance measurement of each component are discussed in the next chapter. This will provide a better understanding of the characteristics of the components used and how they can be integrated to form the various system functions during the integration phase.

THIS PAGE INTENTIONALLY LEFT BLANK

IV. CHARACTERIZATION OF SYSTEM COMPONENTS

Before any modification was made to the mock-up system from the previous design, a two-stage process was adopted. The first stage involved the characterization of components, and the second stage involved integration of components to form various system functions. Detailed descriptions on the components characterization, the measurement setup required, and the performance of each component as compared to the specifications in the data sheets are provided in this chapter. By understanding each component, we can optimize their performance and integrate them into stages to form the different system functions.

A. TEST EQUIPMENT

The measurement and characterization of individual components was carried out using a Rohde and Schwarz (R&S) SMW200A vector signal generator, R&S FSW signal and spectrum analyzer, and RTO2000 digital oscilloscope, as shown in Figure 11, Figure 12, and Figure 13, respectively. This equipment is state of the art and can provide accurate measurements, especially for high operating frequencies. The SMW200A vector signal generator is capable of generating simple or complex signals in the frequency range of 100 kHz to 20 GHz. The FSW signal and spectrum analyzer offers analysis of signals in the frequency domain from 2 Hz to 26.5 GHz, and the RTO2000 digital oscilloscope offers real-time sampling of signals in time domain with a maximum sampling frequency of 20 Giga samples per second. In the previous tests of the design, the performance of individual components was based on the technical specifications provided by the manufacturers. Limited measurements were carried out due to the lack of test equipment.

Figure 11. R&S SMW Vector Signal Generator. Source: [16].

Figure 12. R&S FSW Signal and Spectrum Analyzer. Source: [17].

Figure 13. R&S RTO2000 Digital Oscilloscope. Source: [18].

B. ANALOG RF COMPONENTS CHARACTERIZATION

Manufacturers provide the data specifications for the components they produce; however, the specifications provided in the data sheets are generally carried out in an ideal laboratory setup, at a specific environmental temperature, and with specialized equipment to measure the components' performance. As a result, data sheets serve as a good reference for a particular component; however, the RF components' performance is frequency dependent, so data specifications provided by manufacturers are usually reflective of specific frequencies. Since the MWP DF system is tested at 2.4 GHz, we characterized the components specifically at 2.4 GHz.

1. RF Cables (PE300-36, 141-3SM+, and 141-6SM+)

A coaxial RF cable assembly consists of a coaxial cable terminated by connectors on both ends and was used to connect the source to the load. Numerous cable assemblies of various lengths were required to interconnect different components and subsystems to form the system. Cable assemblies are an essential part of the system, and high losses from the cables assemblies affect the overall system performance. An RF cable assembly can be categorized as flexible, semi-rigid, or corrugate depending on how it is constructed. The categories of cable offer different mechanical characteristics and performance. The choice of RF cable depends on the application, performance requirements, and cost.

a. Types of RF Cables Used in the Thesis

The three types of RF cables used in this thesis research were PE300-36, 141-3SM+, and 141-6SM+ as shown in Figure 14.

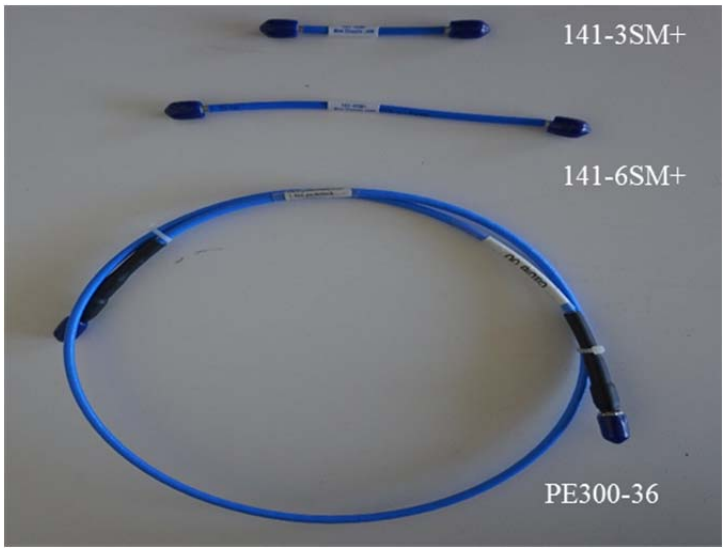

Figure 14. RF Cables PE300-36, 141-3SM+, and 141-6SM+

The PE300-36 is a Subminiature Version A (SMA) Male-to-SMA Male 50 Ω impedance connector terminated RF cable. The cable is 36 inches, or 0.91 m, in length

with a screw type coupling mechanism for its connector interface. This is a flexible cable mainly used for laboratory and integration testing in this thesis.

The 141-3SM+ and 141-6SM+ belong to the 141 series Hand-Flex^{TM} coaxial cables, with lengths of 7.6 cm and 15.2 cm, respectively. These cables are also SMA Male-to-SMA Male 50 Ω impedance connector terminated to allow easy impedance matching. The key feature of these cables is that they are hand-formable semi-rigid with low insertion loss. Several of these cables were used and bent to the required shape for interconnecting components and assembled subsystems.

The specifications provided by the manufacturer for the three cable assemblies are shown in Table 1.

Table 1. Technical Specifications for RF Cable Assemblies PE300-36, 141-3SM+, and 141-6SM+. Adapted from [19], [20], [21].

RF cable model number	Frequency range (GHz)	Insertion Loss (dB)	Voltage Standing Wave Ration (VSWR)	Length (cm)	Category	Manufacturer
PE300-36	DC-18	0.65 at 2 GHz	1.04 : 1	91.00	Flexible	Pasternack
141-3SM+	DC-18	0.15 (max) at 2 GHz	1.15 : 1 (min)	7.60	Semi-rigid	Mini-circuits
141-6SM+	DC-18	0.20 (max) at 2 GHz	1.15 : 1(min)	15.20	Semi-rigid	Mini-circuits

b. Measurement Performance of the RF Cables

To measure the performance of the cable, a 2.4 GHz sinusoidal input signal with a power of 0 dBm was injected into one end of the PE300-36 RF cable. The other end of the cable was connected to the R&S FSW signal and spectrum analyzer to measure the output power in the frequency domain.

Using the R&S RTO 2000 oscilloscope, we observed the time-domain signal and frequency response of the PE300-36 cable as shown in Figure 15. From Figure 15, we observe the measured period of the signal t = 416.75 ps. The test frequency is $f = 1/t$, where f is 2.3995 GHz. The measured peak-to-peak voltage V_{pp} was 0.589 V. The signal output power P_{out} in dBm is [22]

$$P_{out} = 30 + 10\log\left(\frac{V_{pp}^{\ 2}}{400}\right), \tag{1}$$

where V_{pp} is in volts. The output signal power is computed to be −0.62 dBm, which was almost the same as the insertion loss of −0.65 dBm provided in the specifications as indicated in Table 1.

Figure 15. Screenshot of Measurement Results for RF Cable PE300-36 using R&S RTO2000 Digital Oscilloscope at 2.4 GHz with Input Power of 0 dBm

The entire process of measurement was repeated by varying the frequency from 1 GHz to 4 GHz with an increment step size of 1 GHz and input signal power of 0 dBm. The measured power was recorded in Table 2 and plotted against frequency as shown in

Figure 16. From Figure 16, we deduce that as frequency increases, the insertion loss for the cable also increases. As a result, the measured output signal power decreases.

Table 2. PE300-36 Cable Loss against Frequency

Input signal power (dBm)	0	0	0	0
Frequency (GHz)	1	2	3	4
Measure signal output voltage (mV)	590.3	587	571	560
Signal output power measured (dBm), Pout	−0.60	−0.65	−0.89	−1.06

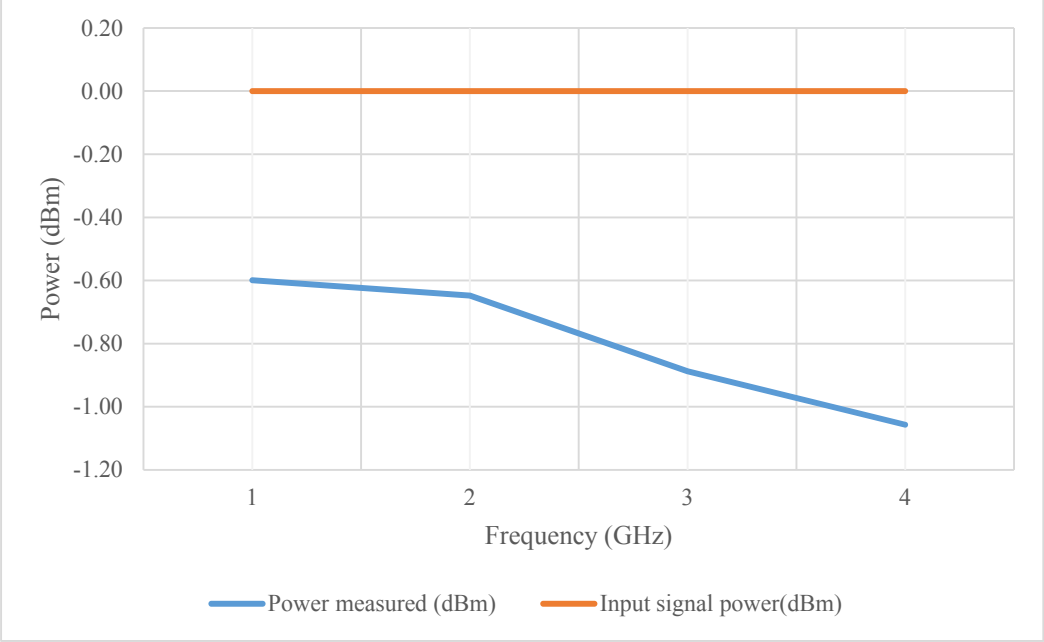

Figure 16. PE300-36 Cable Insertion Loss (dBm) versus Frequency (GHz)

The cable loss measurements were repeated for 141-3SM+ and 141-6SM+ using the same setup and measurement procedure. The frequency range was from 1 GHz to 18 GHz, with an increment step size of 1 GHz and input signal power of 0 dBm. The measured power was recorded and plotted against frequency as shown in Figure 17.

Similar to Figure 16, we see from Figure 17 that as frequency increases, the insertion losses for the RF cables increases. The individual cable loss also is relatively low at 0.1 dBm and 0.06 dBm at 2.4 GHz for 141-6SM+ and 141-3SM+, respectively;

however, for an integrated DF system interconnected by numerous RF cables, accumulation of cable loss affects the overall system performance. During the measurement of the performance of the integrated DF system, we know that the input signal will be low power and on the order of −20 to −30 dBm. The sensitivity of the system is affected if the accumulated cable losses are high.

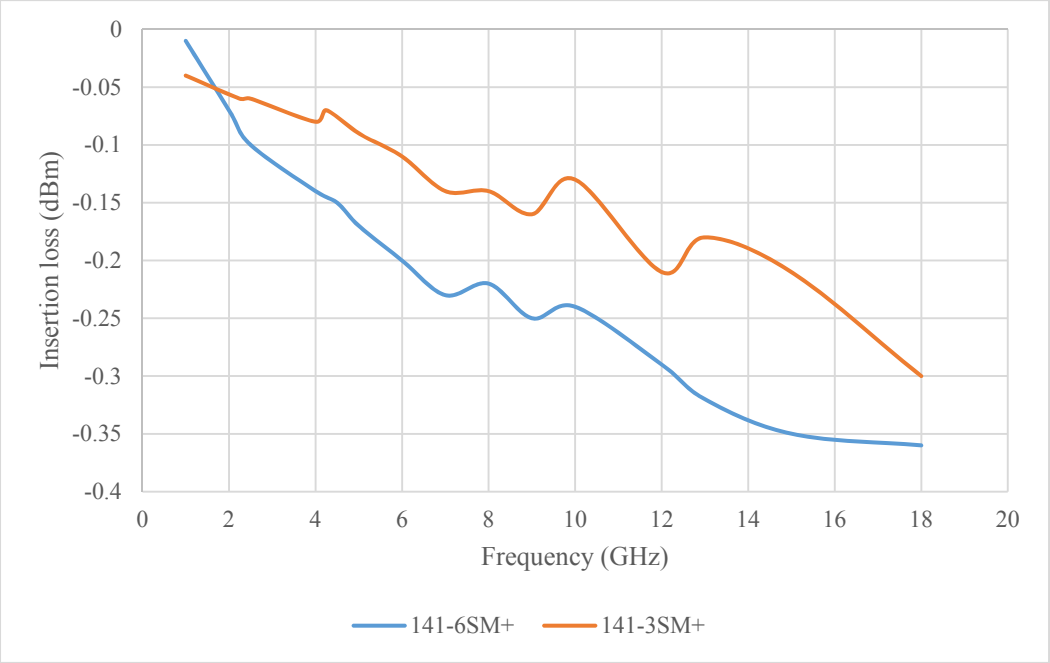

Figure 17. 141-6SM+ and 141-3SM+ Cable Insertion Loss (dBm) versus Frequency (GHz)

During subsequent measurement of individual components, we need to account for cable loss based on the types of cables used by referring to Figure 16 and Figure 17. This allows us obtain accurate characterizations of the component measured. In addition, during integration testing, the signal amplitude at different measurement points can be estimated more accurately if we account for cable losses.

2. Low Noise Amplifier (LNA 2700 and LNA 8G)

The LNA is used at the front-end of the RF receiver to boost the weak signal received after the antenna output since the typical received signal power falls in the range from pW to mW. Both the signal power and noise power are amplified; therefore, it is desirable to have an LNA that provides a sufficiently large gain amplification while possessing a low noise figure (NF). To operate the LNA, we must establish the dynamic range and operate the component in its linear region [23].

a. Types of LNAs Used in the Thesis

Two types of LNA, the LNA 2700 and the LNA 8G as shown in Figure 18, were used in the thesis research. The need to cascade LNA 2700 and LNA 8G for amplification of the received signal after the antenna element is described in Chapter IV.

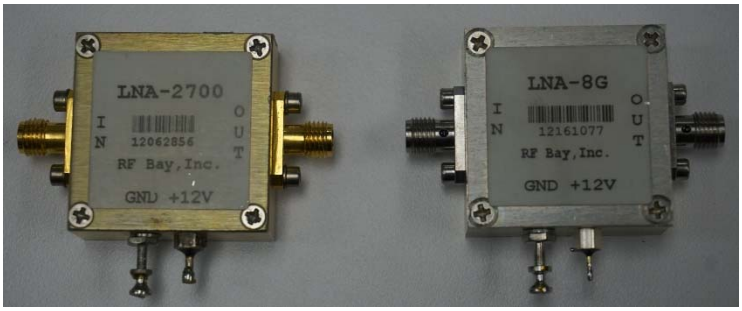

Figure 18. LNA 2700 and LNA 8G

The LNA 2700 operates in the range of 2.2 GHz to 3.2 GHz with a bandwidth of 1 GHz and a nominal NF of 1.7 dB. The LNA 8G operates with a wider frequency range of 1 GHz to 8 GHz with a bandwidth of 7 GHz and a nominal NF of 1.6 dB. The detailed specifications provided by the manufacturer for the two LNAs are shown in Table 3.

Table 3. Technical Specifications for LNA 2700 and LNA 8G.
Adapted from [24], [25].

Component	Frequency range (MHz)	Typical gain (dB)	1dB compression point, P1dB (dBm)	Noise Figure (dB)	Manufacturer	Remarks
LNA 2700	2200–3200	24	10	1.7	RF Bay Inc.	Performance measured at 2.7 GHz.
LNA 8G	1000–8000	25	5.8	1.6	RF Bay Inc.	Performance measured at 4 GHz.

b. Performance Measurement of LNA

The performance measurement setup for the LNA is shown in Figure 19. A sinusoidal input signal with a power of −25 dBm, generated using the R&S SMW200A vector signal generator, was injected into the 141-6SM+ cable and connected to the input of the LNA. The LNA output was connected to R&S FSW signal and spectrum analyzer using the PE300-36 cable to measure the output performance of the LNA.

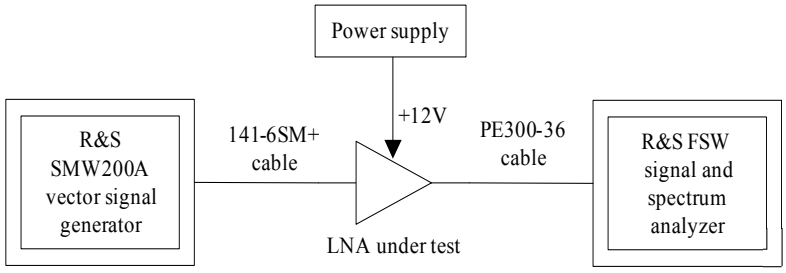

Figure 19. LNA Measurement Setup

The data collected for the LNA 2700 is shown in Table 4. The cable loss for the PE300-36 and 141-6SM+ were extracted using Figure 16 and Figure 17, respectively. The gain for the LNA is computed from

$$LNA\ Gain = P_{out} - P_{in} + CL_{total}\ , \tag{2}$$

where P_{out} is the measured output power, P_{in} is the input power, and CL_{total} is the total cable insertion loss.

Table 4. Data Collected Based on Measurements Carried Out for LNA 2700

Frequency (GHz)	**2.2**	**2.4**	**2.6**	**2.8**	**3.0**	**3.2**
Input power to LNA P_{in} (dBm)	−25	−25	−25	−25	−25	−25
Output power measured after LNA P_{out} (dBm)	−0.75	−1.35	−2.31	−1.86	−1.45	−0.55
Cable insertion loss for PE300-36 (dB)	0.69	0.69	0.75	0.8	0.89	0.89
Cable insertion loss for 141-6SM+ (dB)	0.06	0.06	0.06	0.06	0.06	0.06
Total cable insertion loss CL_{total} (dB)	0.75	0.75	0.81	0.86	0.95	0.95
LNA gain (dB)	25.00	24.40	23.50	24.00	24.50	25.40

The gain for the LNA 2700 is plotted in Figure 20. We see that the gain of the LNA is non-linear and depends on the operating frequency. From Figure 20, the gain was measured to be approximately 24.4 dB at 2.4 GHz, as compared to 24 dB provided in the data specifications as shown in Table 3.

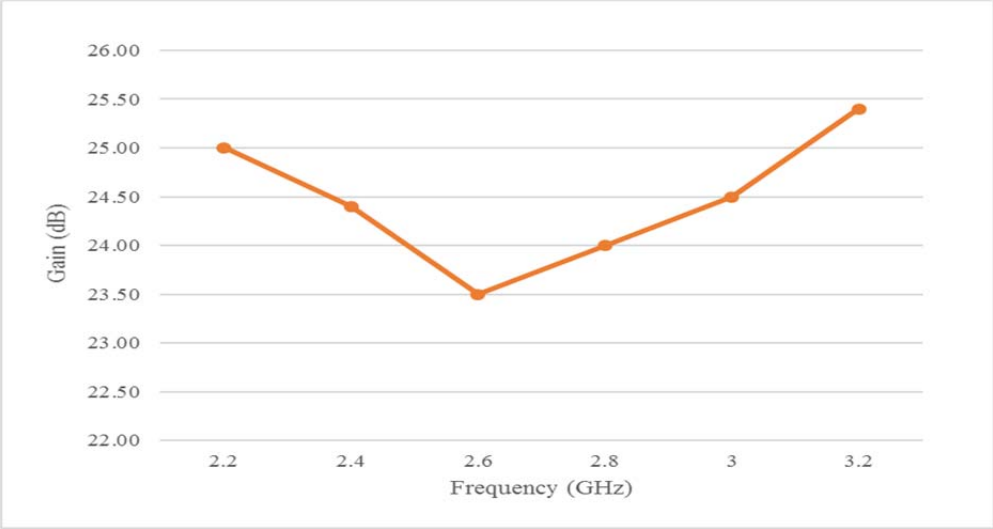

Figure 20. Gain versus Frequency for LNA2700

The entire measurement process was repeated for the LNA 8G, where the data collected is tabulated in Table 5, and the gain performance is plotted as shown in Figure 21. Similarly, the gain of the LNA 8G is non-linear and depends on the operating frequency. From Figure 21, the gain was measured to be approximately 26 dB at 2.4 GHz, as compared to 25 dB provided in the data specifications as shown in Table 3.

Table 5. Data Collected for Measurements Carried Out for LNA 8G

Frequency (GHz)	**1**	**1.5**	**2**	**2.5**	**3**	**3.5**	**4**
Input power to LNA P_{in} (dBm)	−25	−25	−25	−25	−25	−25	−25
Output power measured after LNA P_{out} (dBm)	−2.54	−1.87	0.20	0.28	0.74	−0.32	−1.34
Cable insertion loss for PE300-36 (dB)	0.6	0.625	0.65	0.66	0.89	0.95	1.06
Cable insertion loss for 141-6SM+ (dB)	0.04	0.04	0.05	0.06	0.07	0.07	0.08
Total cable insertion loss CL_{total} (dB)	0.64	0.665	0.7	0.72	0.96	1.02	1.14
LNA gain (dB)	23.10	23.80	25.90	26.00	26.70	25.70	24.80

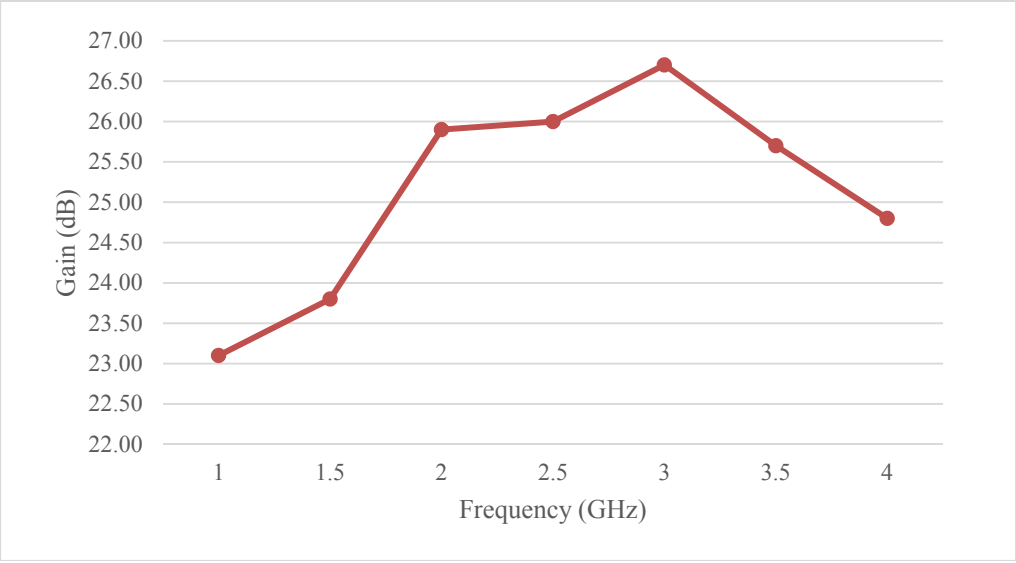

Figure 21. Gain versus Frequency for LNA 8G

c. Linear Response of LNAs

The plot of output power versus input power for an ideal LNA is ideally a straight line with a unit gradient. The power gain of the LNA is computed by taking the ratio of output power to the input power; however, in an actual application, the power gain remains linear only over a limited range of input power, until the output power saturates and the gain is reduced. The linear operating range of the LNA is quantified by finding the power level where the output power is 1.0 dB below the ideal linear unit gradient line. This phenomenon is known as the 1-dB compression point and is denoted by P_{1dB} [26].

To find the P_{1dB} for the LNA, the following measurement procedure was carried out. The output power for each LNA was measured by varying the input signal power from −40 dBm to 0 dBm in increments of 5.0 dBm. The operating frequency used for the input signal was 2.4 GHz. The power transfer function of the LNA 2700 is as shown in Figure 22. The LNA2700 reaches its 1-dB compression of 12.0 dBm when the input power is −9.0 dBm. This result is better than the 1-dB compression performance of 10.0 dBm as shown in the data sheet.

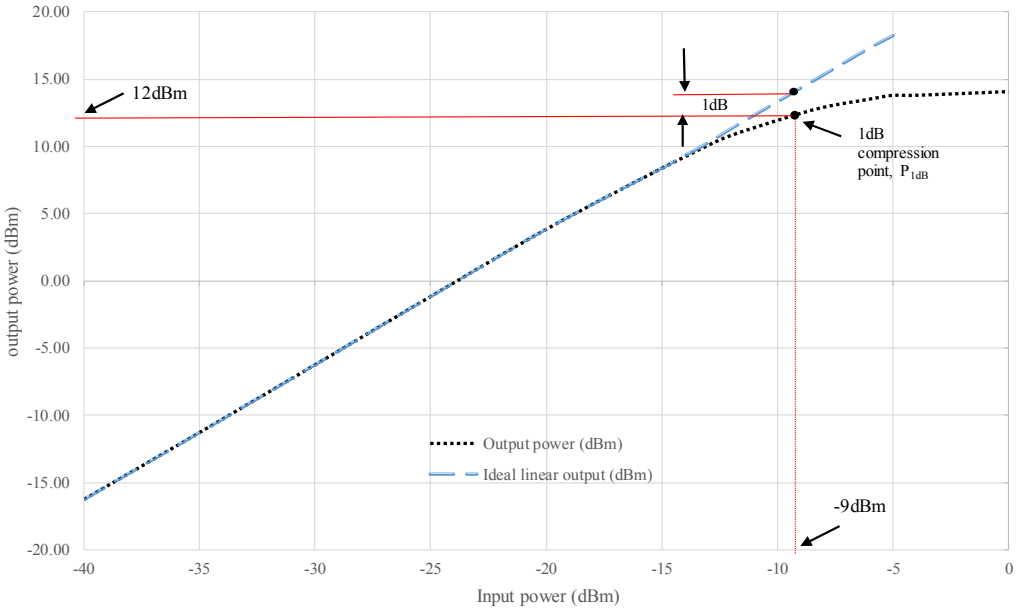

Figure 22. Measured Power Transfer Function of LNA 2700 at 2.4 GHz

The same measurement approach was used on the LNA 8G. The power transfer function of the LNA 8G is as shown in Figure 23. The LNA8G reaches its 1-dB compression of 5.5 dBm when the input power is −17.5 dBm as compared to 5.8 dBm as indicated on the data sheet.

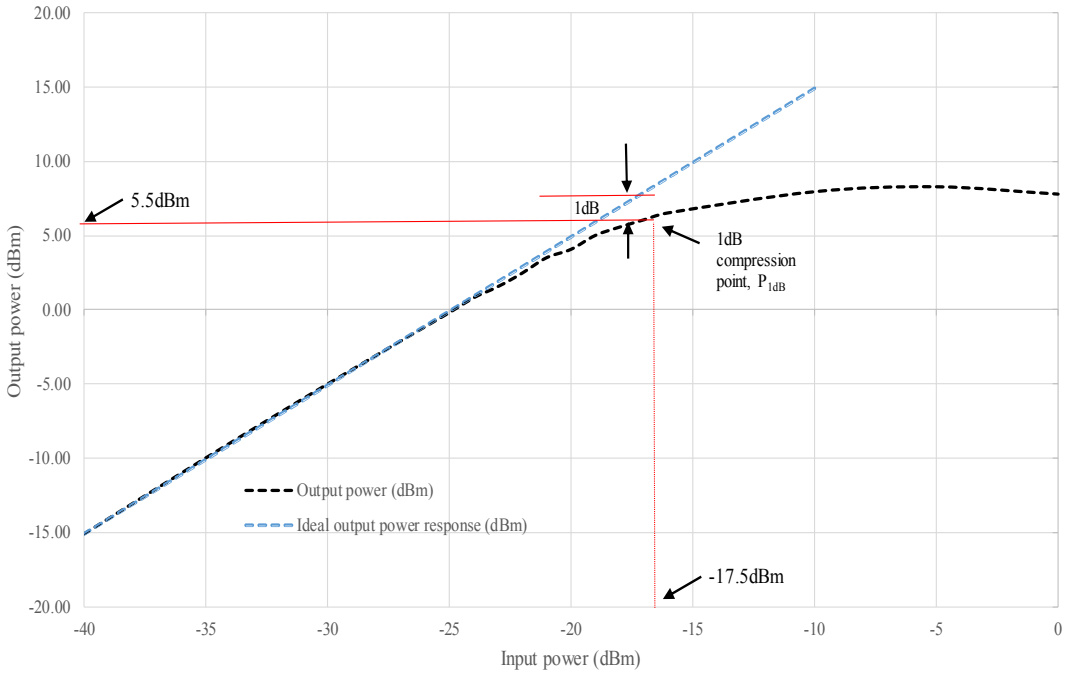

Figure 23. Measured Power Transfer Function for LNA 8G at 2.4 GHz

3. Voltage Variable Attenuator (ZX73-2500+)

The VVA is used to reduce the power of a signal, and the power reduction depends on the level of control voltage $V_{control}$. For our system design, the VVA was connected to the output of the LNA 2700 to attenuate the signal power before it is sent to the input of the LNA 8G. The VVA used is the ZX73-2500+ as shown in Figure 24, and the technical specifications provided by the manufacturer are shown in Table 6.

Figure 24. Voltage Variable Attenuator ZX73-2500+

Table 6. Technical Specifications for VVA ZX73-2500+. Adapted from [27].

Component	Frequency range (MHz)	Insertion loss (dB)	Supply voltage, V+ (V)	Control voltage, $V_{control}$ (V)	Attenuation (dB)	Manufacturer
ZX73-2500+	10-2500	6.2 (max)	3-12	0-17	25 (min)	Mini-circuits

a. Performance Measurements of VVA

The performance measurement for the VVA is shown in Figure 25, and the supply voltage, V+, to the VVA was 12.0 V. To find the level of attenuation with respect to $V_{control}$, the following measurement was carried out. The input signal power to the VVA was varied from 0 dBm to −40 dBm in increments of −10.0 dBm. At each power level, $V_{control}$ was increased from 0 V to 10 V in intervals of 1.0 V. At each $V_{control}$, the power output of the VVA was recorded and plotted as shown in Figure 26. From Figure 26, we observe that consistent high attenuation of 35 to 39 dB is achieved when $V_{control}$ is between 0.0 V and 2.0 V. In addition, variation in attenuation was obtained when the control voltage was between 2.0 V and 5.0 V, and the attenuation level remained fairly flat when $V_{control}$ was beyond 6.0 V, and the level of attenuation is reduced with a decrease in input signal power.

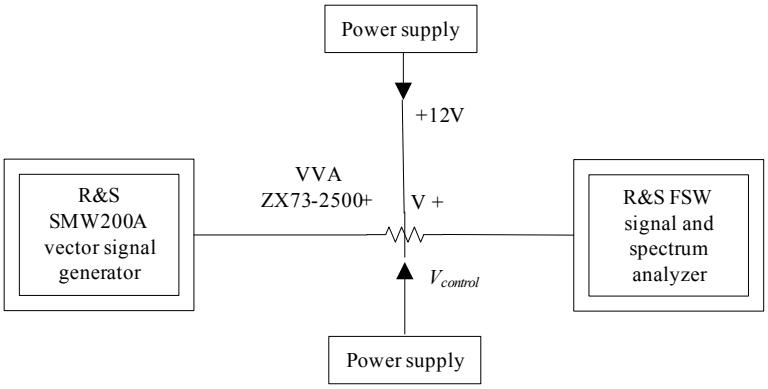

Figure 25. VVA Measurement Setup

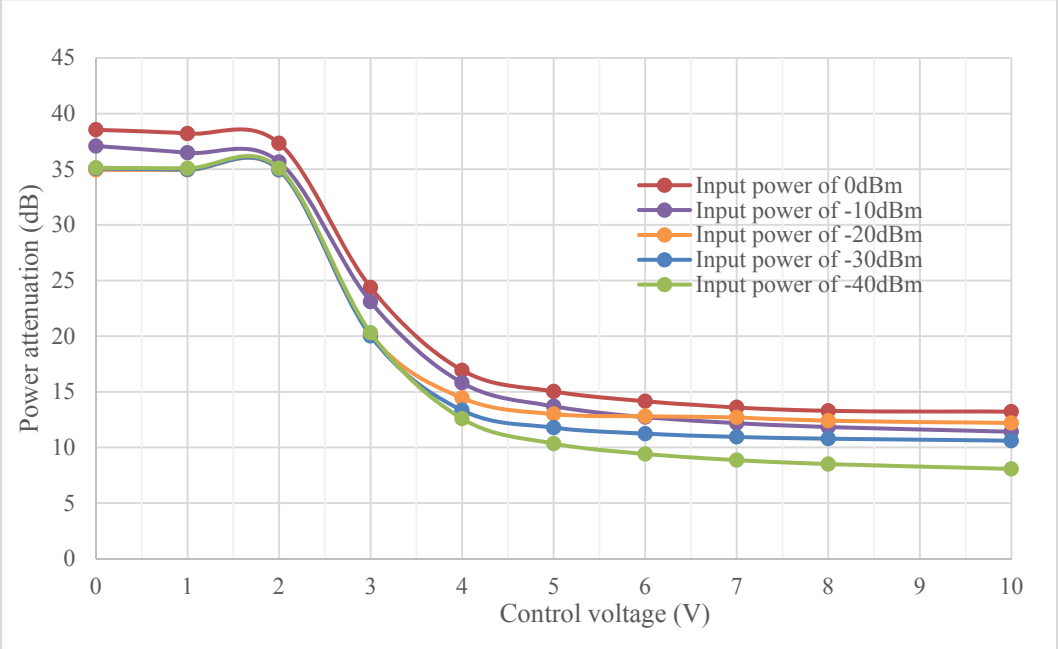

Figure 26. Plot of Power Attenuation by VVA when Varying $V_{control}$ with Supply Voltage V+ =12 V and f = 2.4 GHz

4. Bias Tee (ZFBT-352-FT+)

A bias tee is three-port device through which one input port passes the RF signals, and the DC bias voltage is added through the other input port. The combined inputs produce a DC and RF at the output port. For our system design, the bias tee was added after the LNAs cascade pair so that a DC bias voltage could be added to the RF signals to cause the DE-MZM to operate in the linear region. The bias tee used is the ZFBT-352-

FT+ as shown in Figure 27, and the technical specifications provided by the manufacturer are shown in Table 7.

Figure 27. Bias Tee ZFBT-352-FT+

Table 7. Technical Specifications for ZFBT-352-FT+. Adapted from [28].

Component	Frequency range (MHz)	Amplitude balance (dB)	Phase balance (degrees)	Insertion loss (dB)	Manufacturer
ZFBT-352-FT+	300–3500	± 0.3	± 6	1.1 (max)	Mini-Circuits

a. Performance Measurements of Bias Tee

The setup to measure the performance of the bias tee is as shown in Figure 28. A sinusoidal input signal with a frequency of 2.4 GHz and power of 5.0 dBm was generated using a R&S SMW200A vector signal generator and injected into the bias tee. The signal output power was measured when a stepped DC bias was added from 0.0 V to 3.0 V in increments of 0.5 V.

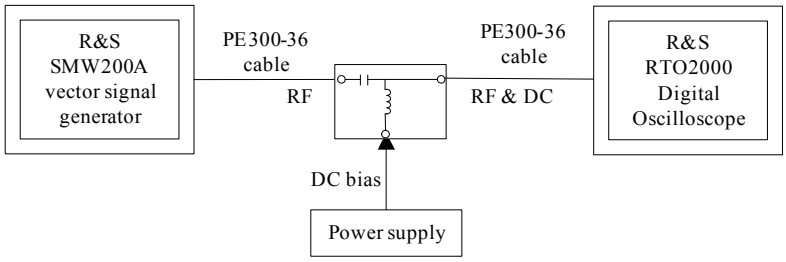

Figure 28. Bias Tee Measurement Setup

Table 8. Data Collected for Measurements Carried Out on Bias Tee

Bias voltage (V)	0	0.5	1	1.5	2	2.5	3
Input power P_{in} (dBm)	5	5	5	5	5	5	5
Output power measured P_{out} (dBm)	2.58	2.54	2.52	2.54	2.57	2.41	2.46
Total cable loss CL_{total} (dB)	1.38	1.38	1.38	1.38	1.38	1.38	1.38
Insertion loss IL (dB)	1.04	1.08	1.10	1.08	1.05	1.21	1.16

Based on the data collected in Table 8, the insertion loss IL using dB quantities is calculated using

$$IL = P_{in} - P_{out} - CL_{total} \tag{3}$$

where P_{in} is the input power, P_{out} is the measured output power, and CL_{total} is the total cable insertion loss. The insertion loss for the bias tee was plotted as shown in Figure 29. From Figure 29, we see that the insertion is between 1.04 dB to 1.21 dB after introducing the bias voltage as compared to 1.1 dB as provided in the data specifications shown in Table 7. Since the introduction of DC bias to the bias tee results in insertion loss, the bias tee was introduced only after the LNA as part of our design consideration.

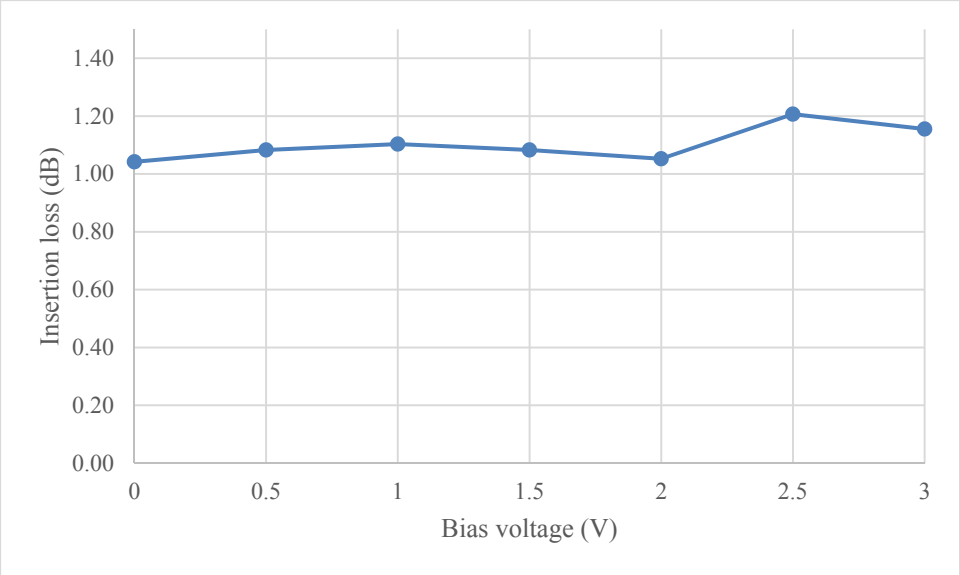

Figure 29. Plot of Insertion Loss by Bias Tee when Bias Voltage is Applied

5. Four-Way Power Combiner/Divider (PE20S0014)

A power combiner/divider can operate in two ways. As a combiner, two, three or four input signals are combined to produce an output signal. As a divider, the input signal is split into two, three or four output signals. Ideally, the power divider produces output signals with equal phase and amplitude. The power combiner/splitter used in our design is shown in Figure 30, and its technical specifications are given in Table 9. The power divider was used to split the reference signal four ways, J2, J3, J4, and J5; however, only three of the outputs were required. Consequently, the fourth output (J5) was terminated with a dummy load. The other three outputs were each connected to one arm electrode of the respective DE-MZM. The other arm of each DE-MZM was connected to measurement channels 1, 2, and 3, respectively.

Figure 30. Four-Way Power Divider PE20S0014

Table 9. Technical Specifications for PE20S0014. Adapted from [29].

Component	Frequency range (MHz)	Amplitude balance (dB)	Phase balance (degrees)	Manufacturer
PE20S0014	1000–6000	± 0.3	± 6	Pasternack

a. Performance Measurements of Four-Way Power Combiner/Divider

The setup to measure the performance of the four-way power divider is shown in Figure 31. An input signal at 2.4 GHz with power of 0.0 dBm was generated and connected the input to J1. The outputs J2 to J5 were connected to CH1 through CH4, respectively, of the oscilloscope, and the screenshot from the oscilloscope is shown in Figure 32.

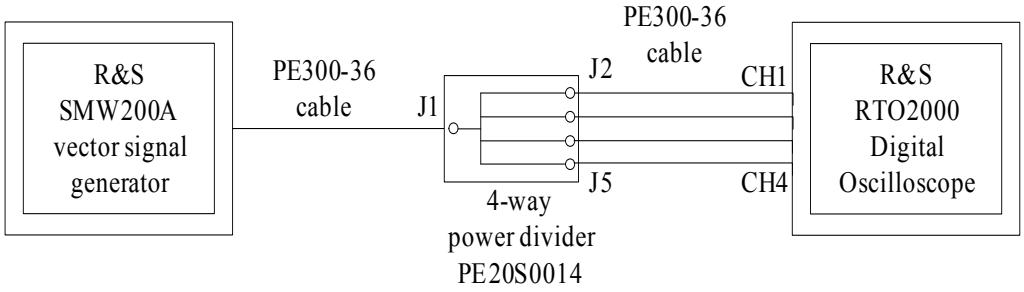

Figure 31. Four-Way Power Divider Measurement Setup

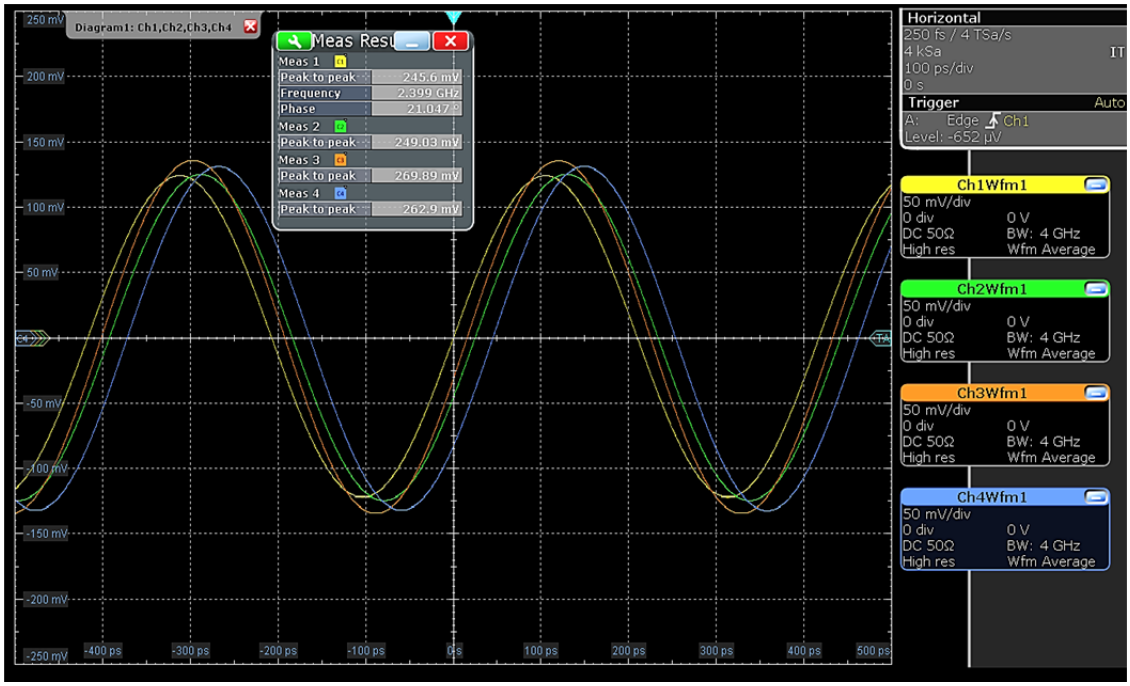

Figure 32. Signals Measured from the Output of Four-Way Power Divider PE20S0014

From Figure 32, we see that the power divider produced four output signals with unequal amplitude and phase. The measured V_{pp} for each channel was recorded in Table 10, and the corresponding output power was calculated using (1).

Table 10. Data Collected for Measurements Carried Out on Four-Way Power Divider

Oscilloscope Channel / (power divider output)	**Measured output voltage, V_{pp} (V)**	**Measured output power P_{out} (dBm)**	**Input power P_{in} (dBm)**	**Total cable insertion loss CL_{total} (dB)**	**Insertion loss IL (dB)**
1 / (J2)	0.2456	−8.2	0	1.38	6.82
2 / (J3)	0.2490	−8.1	0	1.38	6.72
3 / (J4)	0.2699	−7.4	0	1.38	6.02
4 / (J5)	0.2629	−7.62	0	1.38	6.24

The insertion loss IL in Table 10 was calculated using (3). From Table 10, we see that the four-way power divider passes 20.7 % (−6.82 dB) to 25 % (−6.02 dB) of the power to the four output ports.

Amplitude balance measures how evenly the power is split between the two arms of each output pair, J2/J3 and J4/J5, and is calculated by subtracting the output power of one channel from its adjacent channel. In this case, the amplitude imbalance between J2 and J3 is −0.1 dB and 0.22 dB between J4 and J5. These results are better than the given specification of ± 0.3 dB.

The characterization of the RF components used in the system were summarized in this thesis. The key photonic component used in the thesis, the DE-MZM, is discussed in the next chapter.

THIS PAGE INTENTIONALLY LEFT BLANK

V. MACH-ZEHNDER MODULATOR

The MZM, the key component used in this thesis research, is described in this chapter. By understanding how an MZM works, we can integrate it with the front-end RF components to produce the phase difference output measurement from the respective channels with respect to the reference channel.

A. TYPES OF MZM

The MZM has wide applications in MWP, such as microwave generation, delay filter implementation, and optical microwave mixing. The MZM comes in the form of a single- or dual-electrode design, with an internal configuration of X-cut or Z-cut, and the structure is implemented using various types of material. The choice of MZM to be used depends on the application. For the dual drive or DE-MZM, two modulating voltages are applied separately to two optical waveguide electrodes. The key advantage of using a DE-MZM is that two separate voltages can be applied, enabling a host of various applications [30]. The Z-cut configuration offers the best impedance match for MWP applications and requires lower modulating voltages [31].

The most popular type of electro-optic modulator is the lithium niobate ($LiNbO_3$) based MZM as it is a mature technology and is relatively inexpensive to produce as compared to other materials [32]. In addition, the $LiNbO_3$ MZM offers low insertion loss, maximum electro-optic sensitivity, and its application is independent of the wavelength used [33]. The principal mechanism for the modulators is known as linear electro-optic, better known as the Pockel effect. When a CW laser is injected into an MZM, it is split into two interferometer waveguide arms. If an external electric field is introduced onto both arms of the MZM, the refractive index of the two optical waveguide arms changes proportionally. This causes a phase change between the two arms and modulates the CW laser passing through. At the output of the MZM, the modulated laser in the two optical waveguides is recombined. The result is that the amplitude corresponds to the phase difference between the two arms and reflects the amount of constructive and/or destructive interference that exists [34].

B. HOW AN DE-MZM WORKS

The optical modulator used in our design is a Z-cut LiNbO3 DE-MZM with differential input electrodes as shown in Figure 33. The input laser average power is P_i W, and the output power is P_o W.

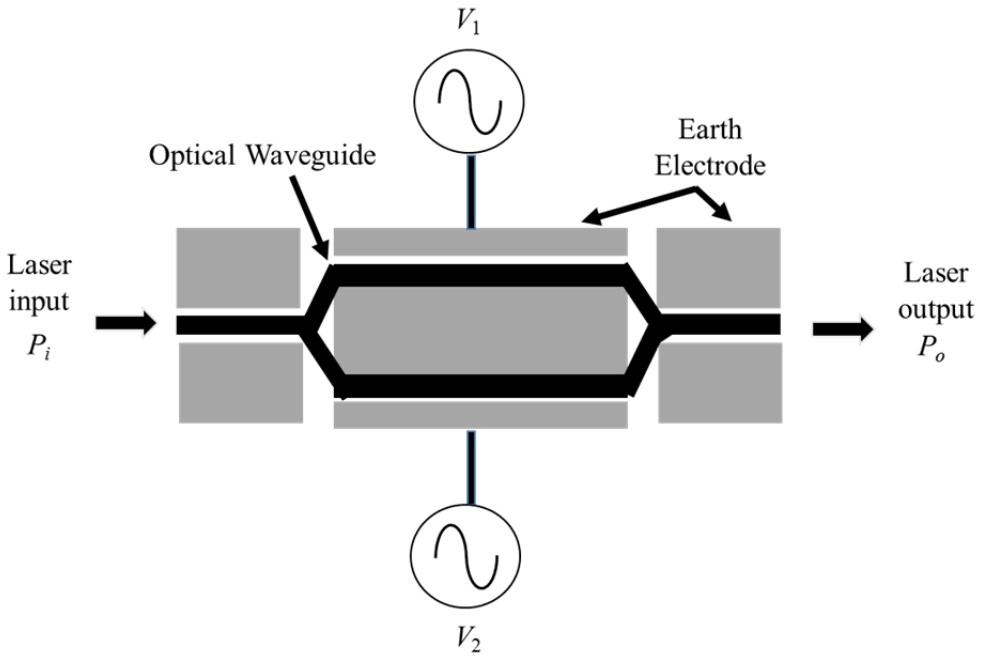

Figure 33. Cross-Sectional View of Dual-Electrode Z-Cut DE-MZM. Adapted from [33].

The laser at the input to the DE-MZM has constant power, which is split between two optical waveguide paths. The laser is modulated by two drive voltages, V_1 and V_2, applied through the two electrodes. The drive voltage V_1 represents the electrical signal converted from the RF wave incident on the reference channel, and V_2 represents the electrical signal converted from the RF wave incident from antenna channel 1, 2, or 3. If there is a phase difference between the two antenna signals, it causes the refractive index in the two optical waveguides to change and reflect the phase accordingly. As a result, the DE-MZM produces an optical output with an amplitude level corresponding to the phase difference between the reference and the measurement channel.

The transfer characteristic of the DE-MZM is [10]

$$\frac{P_o}{P_i} = \frac{1}{2}\left[\,1 + \cos\left(\frac{V_1 - V_2}{V_\pi}\,\pi + \varphi_b\right)\right], \tag{4}$$

where V_1 and V_2 are the voltages applied to the electrodes, V_π is the input voltage that causes a phase shift of 180°, or π radians, between the two electrodes. The phase φ_b represents a constant phase bias

$$\varphi_b = 2\pi\frac{\Delta_n}{\lambda} + \pi\frac{V_{bias}}{V_\pi}, \tag{5}$$

where Δ_n denotes the optical path length mismatch between the two input arms of the DE-MZM, λ is the operating wavelength, and V_{bias} is the bias voltage. If we assume $\varphi_b = 0$, then (4) reduces to

$$\frac{P_o}{P_i} = \frac{1}{2}\left[\,1 + \cos\left(\frac{V_1 - V_2}{V_\pi}\,\pi\right)\right]. \tag{6}$$

If we let

$$\alpha = \left(\frac{V_1 - V_2}{V_\pi}\,\pi\right), \tag{7}$$

then substituting (7) into (6), we get

$$\frac{P_o}{P_i} = \frac{1}{2}\,[\,1 + \cos\alpha\,]. \tag{8}$$

Using the trigonometry identity

$$\cos 2\alpha = 2\cos^2\alpha - 1, \tag{9}$$

we find that (8) reduces to

$$\frac{P_o}{P_i} = \cos^2\left(\frac{\alpha}{2}\right). \tag{10}$$

From (10), the transfer function of the DE-MZM takes on a symmetrical cosine-squared shape and is plotted as shown in Figure 34.

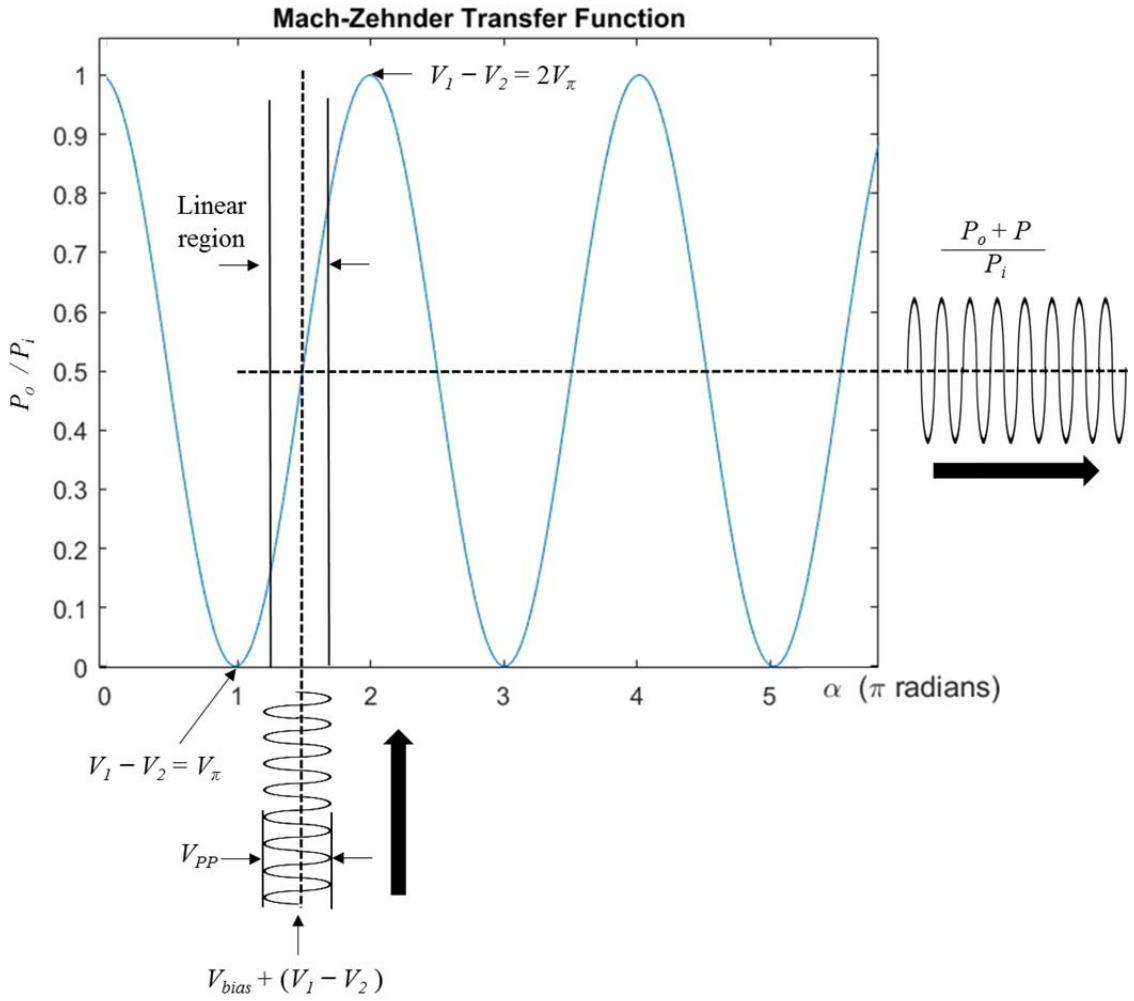

Figure 34. DE-MZM Transfer Function. Adapted from [34].

From Figure 34, we can establish a few relationships for the case where the DE-MZM uses the differential input electrode design. First, if the reference signal is in phase with the measurement channel, where $V_1 - V_2 = V_\pi$, destructive interference occurs and DE-MZM produces a zero output. Second, if the reference signal is 180° out of phase from the measurement channel, constructive interference occurs where $V_1 - V_2 = 2V_\pi$, and the output from the DE-MZM is at its maximum. Third, if there is a phase difference between the reference and measurement channels, the optical output produces a modulated signal, with its amplitude corresponding to the phase difference. In addition, the bias voltage V_{bias}, or DC offset, is applied to appropriately bias the DE-MZM

to operate in the quasi-linear region. Within this quasi-linear region, the DE-MZM applies a linear amplification to the signal on the electrodes across the signal dynamic range V_{pp} as shown in Figure 34 [34]. Typically, the bias voltage is at the midpoint of 0 and V_{π} or at any odd multiple of V_{π} / 2 of the transfer function. This is known as the quadrature point.

C. RESULTS

The DE-MZM used in the system design is shown in Figure 35. This modulator offers a modulation speed of up to 10.7 Gbits/sec and requires low drive voltages. The two electrical signals from the RF appearing at the antenna elements are connected to the dual electrodes of the DE-MZM via an RF Gilbert push-on (GPO) connector [35]. Since the DE-MZM directly modulates the CW laser using the two high frequency electrical signals, any unnecessary losses must be minimized. The unique push-on connector interface offers minimum insertion and mismatch losses even if there is slight misalignment in the connection. This cannot be achieved with the use of threaded connectors.

Figure 35. $LiNbO_3$ Dual Electrode -MZM (FTM7921ER). Adapted from [35].

In Figure 36 to Figure 44, the signals shown in yellow and green represent the reference and measurement channels, respectively. The signal shown in orange is the PD's electrical output signal converted from the DE-MZM optical signal. In addition, the effect of introducing V_{bias} is investigated using Figure 38 to Figure 44. In order to show the phase difference comparison between the two channels and how it affects the DE-

MZM output, the V_{bias} in Figure 38 to Figure 44 was deliberately removed using the oscilloscope settings.

When both the reference and measurement channels are in-phase and have same amplitude level, the resultant output from the DE-MZM is zero, as shown in Figure 36; however, when both the reference and measurement channels are 180° out-of-phase, constructive interference is at its maximum as shown in Figure 37. For both scenarios, V_{bias} was set to 0.0 V.

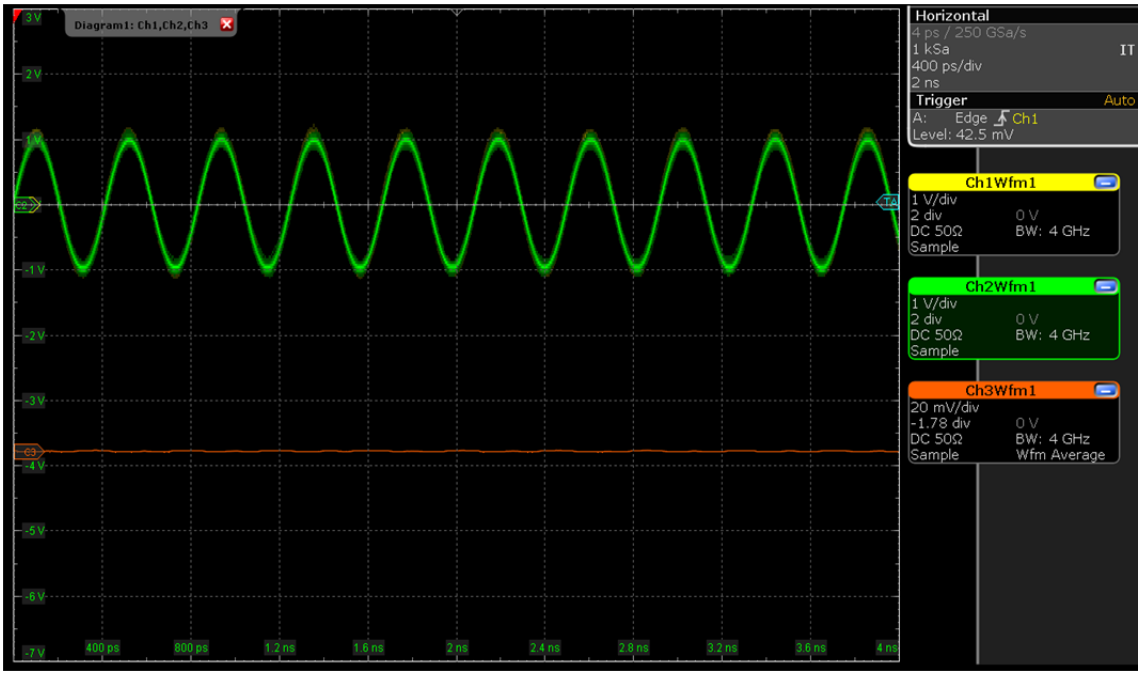

Figure 36. In-Phase Reference and Measurement Channel with V_{bias} = 0.0 V

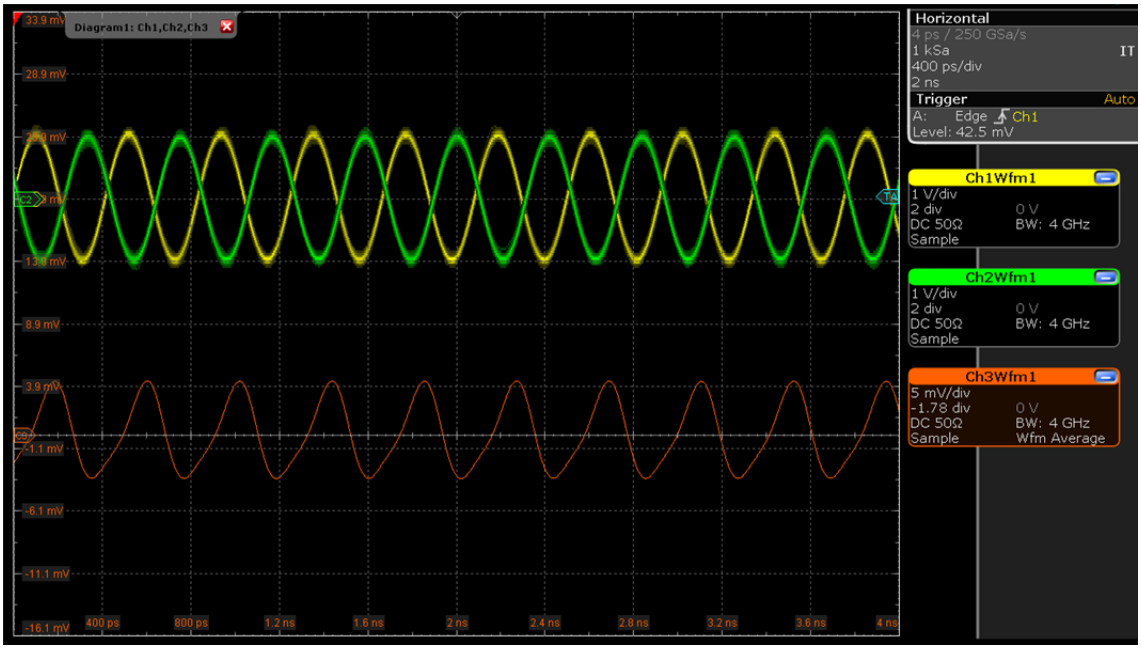

Figure 37. 180° Out of Phase between Reference and Measurement Channel with V_{bias} = 0.0 V

To investigate the effect of bias voltage on the DE-MZM, V_{bias} of 0.5 V was set. Figure 38 to Figure 40 correspond to a phase shift of 0°, 90º, and 180° between the reference and measurement channels, respectively.

In the case where both the reference and measurement channels are in-phase, we see that the DE-MZM produces a residual sinusoidal output with a low amplitude due to a slight mismatch as shown in Figure 38. When compared to Figure 36, where the output is virtually zero, this shows that the bias voltage caused the DE-MZM to be shifted and to operate in the quasi-linear region and cause the output to be slightly amplified. From Figure 39, we see that the increase in phase difference between the reference and measurement channels caused the DE-MZM to produce an output with a higher amplitude. Once again, when both the reference and measurement channels are 180° out of phase, constructive interference is at its maximum as shown in Figure 40.

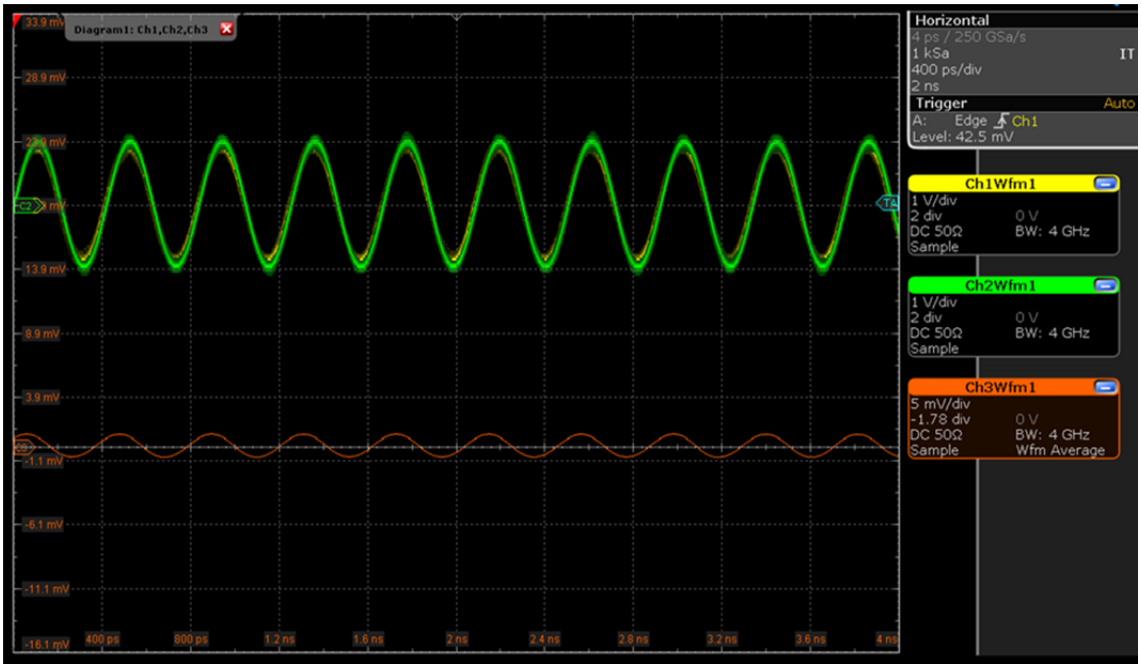

Figure 38. In-Phase between Reference and Measurement Channels with V_{bias} = 0.5 V

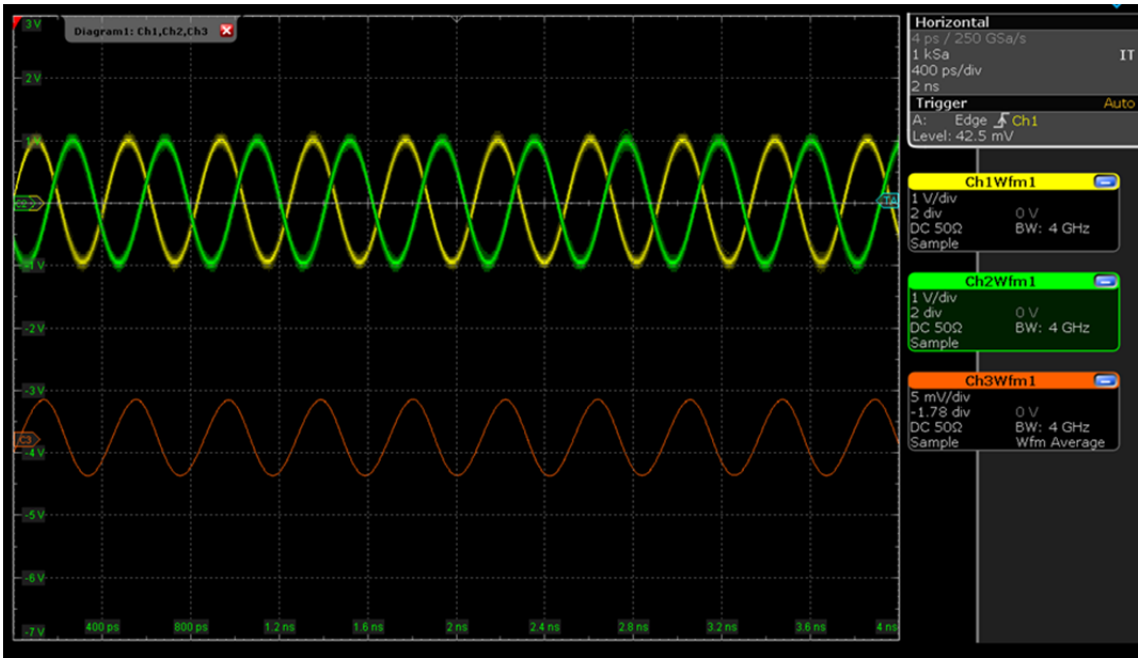

Figure 39. 90° Phase Shift between Reference and Measurement Channels with V_{bias} = 0.5 V

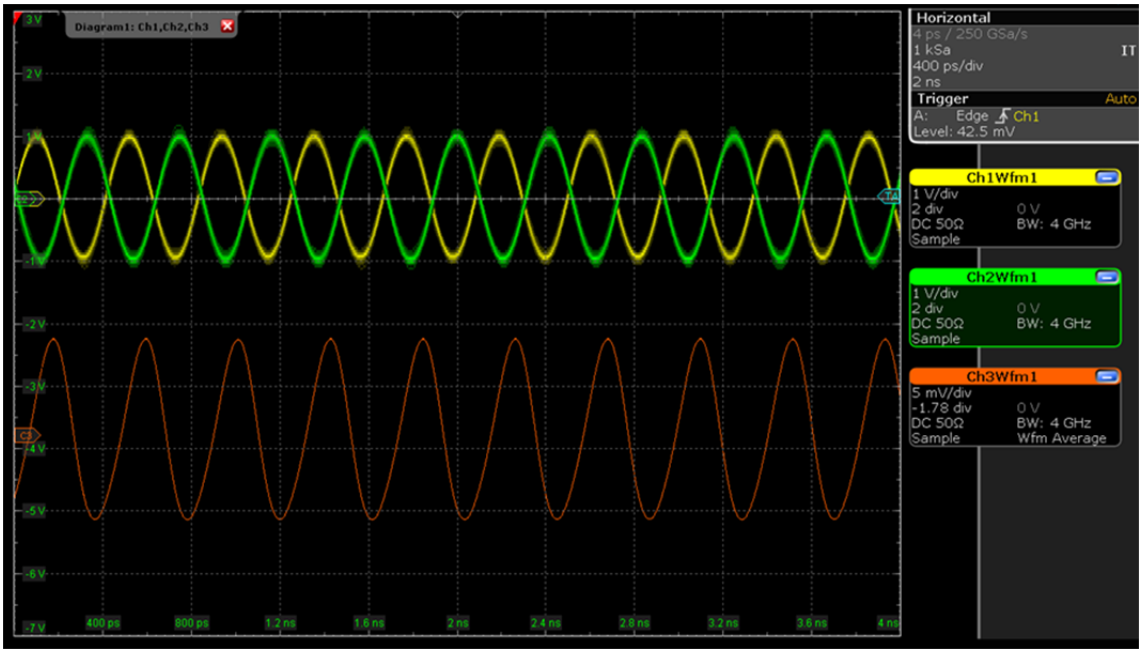

Figure 40. 180° Out of Phase between Reference and Measurement Channels with V_{bias} = 0.5 V

The following measurements were carried out to understand the effect of setting the bias voltage V_{bias} at the quadrature operating point, which occurs at odd multiples of V_{π} / 2 . Since both V_{1peak} and V_{2peak} were at 1.0 V, V_{π} occurred at 2.0 V; therefore, we chose V_{π} / 2 = 1.0 V as the V_{bias} . Figure 41 and Figure 42 correspond to a phase shift of 0° and 180° between the reference and measurement channels, respectively. If we compare Figure 38 with Figure 41 and Figure 40 with Figure 42, we see that there is a significant difference in the output voltage from PD with different V_{bias} .

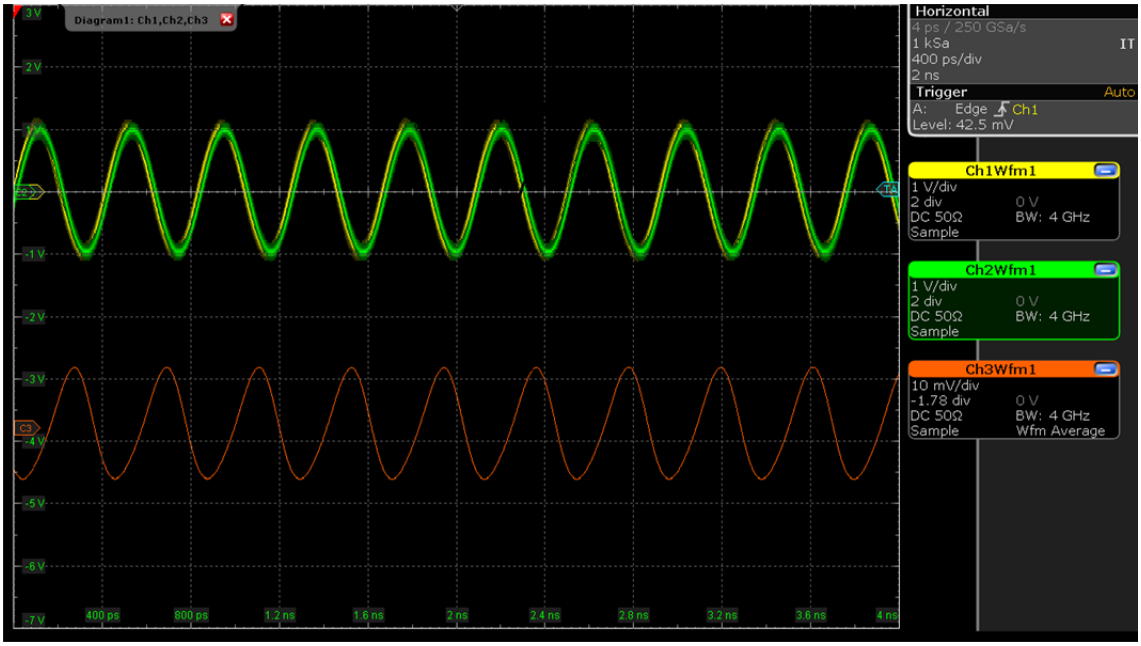

Figure 41. In-Phase between Reference and Measurement Channels with V_{bias} = 1.0 V

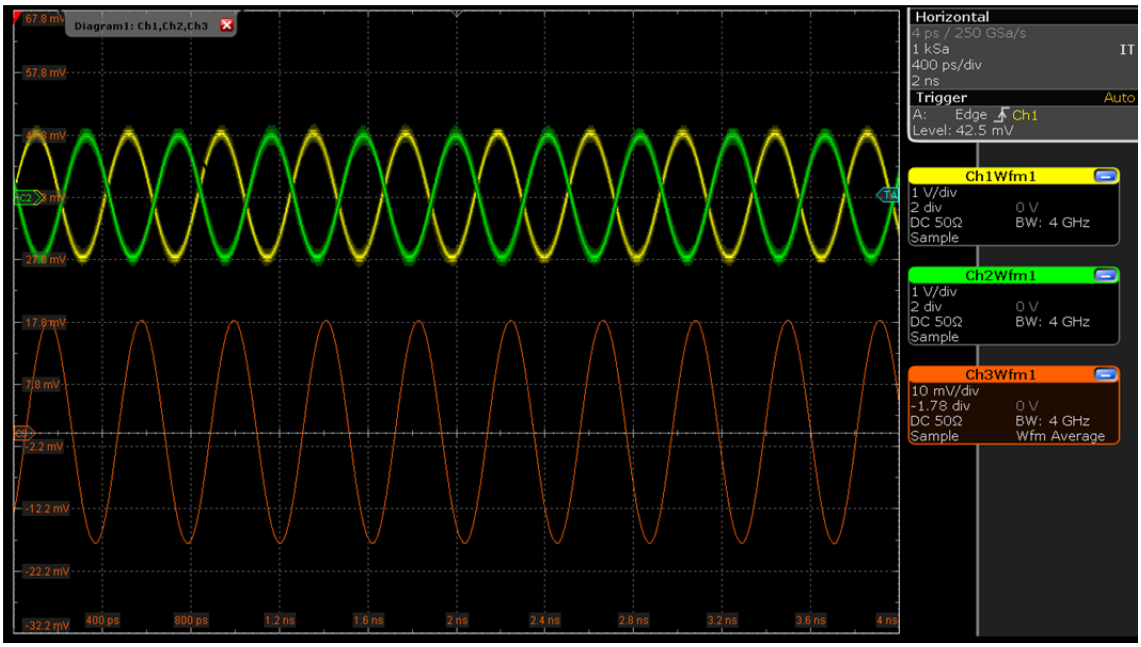

Figure 42. 180° Out of Phase between Reference and Measurement Channels with V_{bias} = 1.0 V

So far, we have used the same amplitude level for both V_1 and V_2 for measurements. The following test measurements were carried out using different amplitude levels for V_1 and V_2 to investigate the response of the DE-MZM. In addition, a phase shift of 0° between the reference and measurement channel was used. Figure 43 and Figure 44 correspond to the use of V_{bias} of 0.5 V and 1 V, respectively. If we compare Figure 38 with Figure 43 and Figure 41 with Figure 44, we see that matched amplitudes at both electrodes are required to obtain an optimum response from the DE-MZM. To achieve matching amplitudes at both electrodes, we calibrate by adjusting the $V_{control}$ to the VVA located in Box 1, as shown in Figure 7.

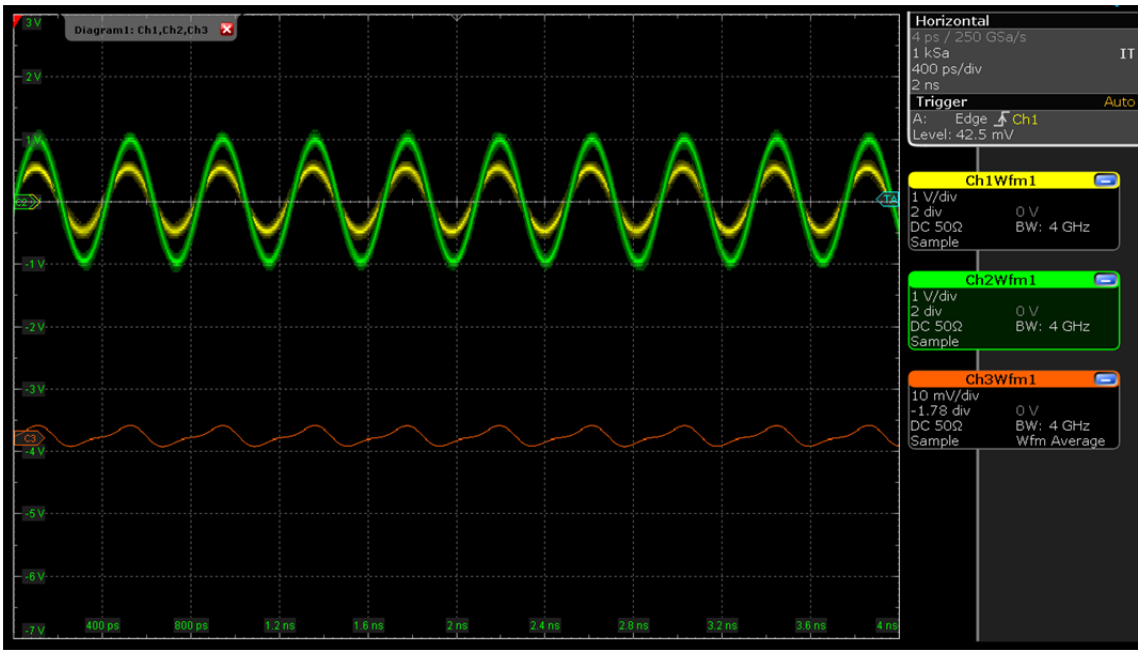

Figure 43. Reference and Measurement Channel In-Phase but with Different Amplitude Levels and with V_{bias} = 0.5 V

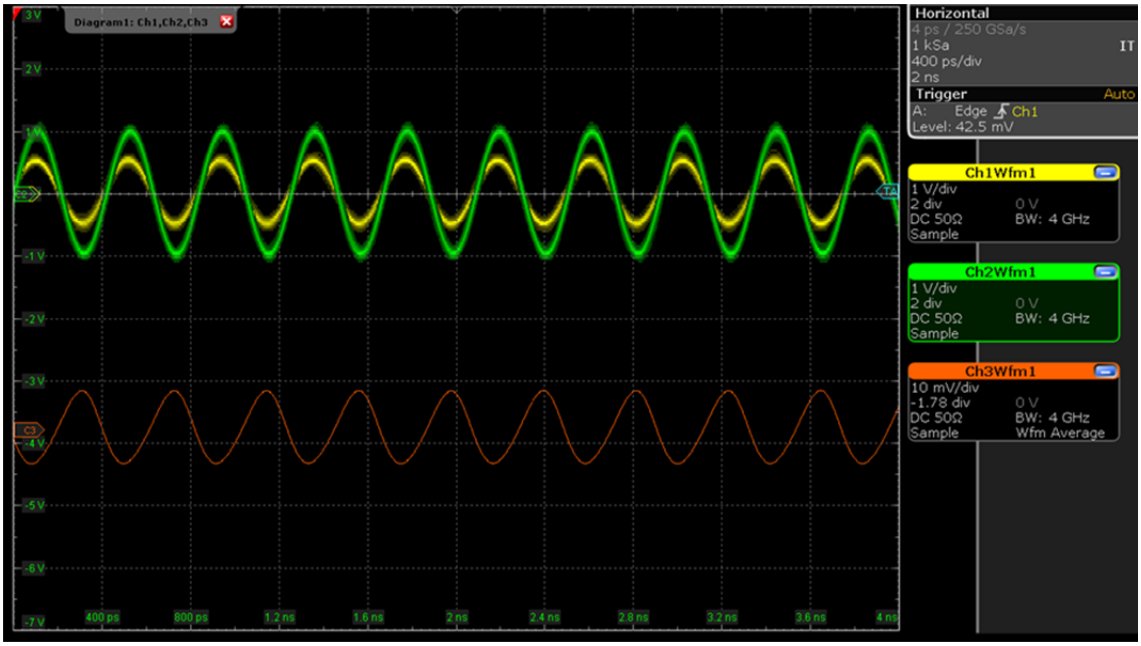

Figure 44. Reference and Measurement Channel In-Phase but with Different Amplitude Levels and with V_{bias} = 1.0 V

From the test measurements carried out with the DE-MZM, three key conclusions were drawn. First, bias voltage is important in operating the DE-MZM in the linear region of the transfer function to obtain more accurate results. The results of 180° out of phase between reference and measurement channels shown in Figure 37, Figure 40, and Figure 42, but using different V_{bias}, are summarized in Table 11. With the correct V_{bias}, the phase difference between the reference and measurement channels is significantly amplified at the DE-MZM optical output; therefore, the system design must incorporate a design where bias voltage can be tuned and introduced into the optical modulators to operate them in the linear region of the transfer function.

Table 11. Effect of Bias Voltage V_{bias} on DE-MZM

V_{bias} (V)	0	0.5	1
Peak voltage measured from output of PD (mV)	8	15	35

Second, the driving voltages from the channels into the two arms of the DE-MZM must be matched to achieve an optimum response from the optical modulators as discussed previously. This can be achieved by performing a calibration on the system prior to any measurement. To match the signal amplitudes, the VVA for the LNAs cascade can be varied to achieve the correct level of signal amplification for all the channels.

Lastly, the RF signals can externally modulate a 1550-nm CW laser source using the DE-MZM. The output amplitude from the DE-MZM corresponds to the phase difference between the two RF channels applied through the electrodes. The use of MWP eliminates complex RF/IF frequency down-conversion architecture.

In the two previous chapters, we discussed the components used in the front-end for the DF system. In the next chapter, we discuss the integration of the system in stages and the measurements necessary to establish a baseline for comparison.

THIS PAGE INTENTIONALLY LEFT BLANK

VI. INTEGRATION AND TESTING

Once the characterization of components in the first stage was concluded, we proceeded with the second stage, the integration of different components to form various functional blocks. The performance of each functional block was measured and calibrated to ensure each signal path could produce consistent and optimal results. The different functional blocks were subsequently integrated to form the complete MWP DF system. Prior to that, we established the level of gain to amplify the received signal by varying the VVA without operating the cascade of front-end LNAs in the 1-dB compression region.

A. FRONT-END LNA CASCADE GAIN CONTROL

Once the antenna elements convert the RF electromagnetic waves into electrical signals, the electrical signals must be amplified before they are further processed. Depending on the electrical signal strength, we adjusted the gain of the LNA to the required level. The design adopted the cascade of two fixed gain LNAs, the LNA 2700 and the LNA8G. The gain of the channel is varied through the VVA. The correct gain control is paramount to ensure the measured phase data is accurate.

The rationale and importance of the LNAs cascade, with the variable gain control VVA, is illustrated in the following three scenarios.

1. Gain for Reference Channels

If the received 2.4 GHz output signal from the antenna element has a power of −20 dBm, then the signal is amplified to 4.0 dBm, or 1.0 V_{pp}, by the LNA 2700 according to the power transfer function, Figure 22. This output voltage is supplied to drive one arm of the DE-MZM. The problem arises with reduction in output voltage of the reference signal after splitting the signals through the four-way power splitter. As a result, an additional LNA 8G was introduced to generate sufficient amplification for the reference channel.

2. Operating LNAs in the Linear Region

In the preceding scenario, with the signal power at 4.0 dBm, the gain of the LNA 2700 must be reduced prior to the input of the LNA 8G. Otherwise, it causes the LNA 8G to operate within the 1-dB compression region, as shown in Figure 23. To overcome this problem, the VVA was inserted between the LNA 2700 and the LNA 8G.

3. Matching Amplitudes for DE-MZM

In addition, from Figure 41, we also determined that the DE-MZM must provide equivalent output amplitudes for both electrode signals to be matched. The VVA is critical in tuning and matching the amplitudes of both signals.

To establish the transfer function of the LNAs cascade, the laboratory setup is shown in Figure 45. The output voltage V_{pp} of the LNA 8G was measured by varying the input signal power to the LNA 2700 from −40.0 dBm to −20.0 dBm in increments of 5.0 dBm. The operating frequency used for the input signal was 2.4 GHz. The power transfer functions for the LNA 2700 and the LNA 8G are given in Figure 22 and Figure 23, respectively.

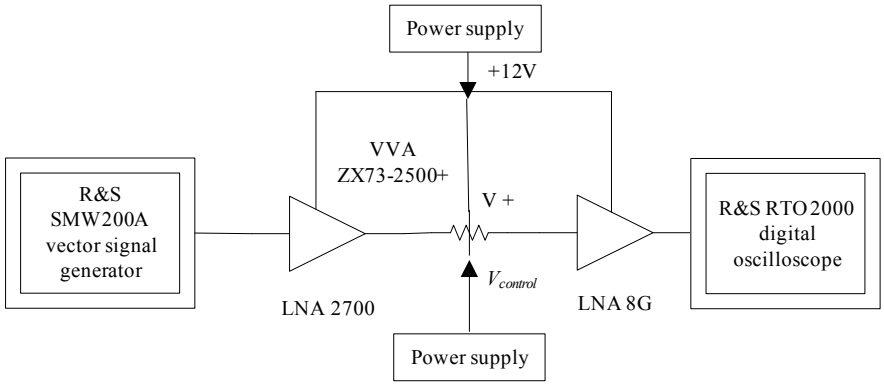

Figure 45. Laboratory Setup to Establish the Transfer Function of the LNAs Cascade

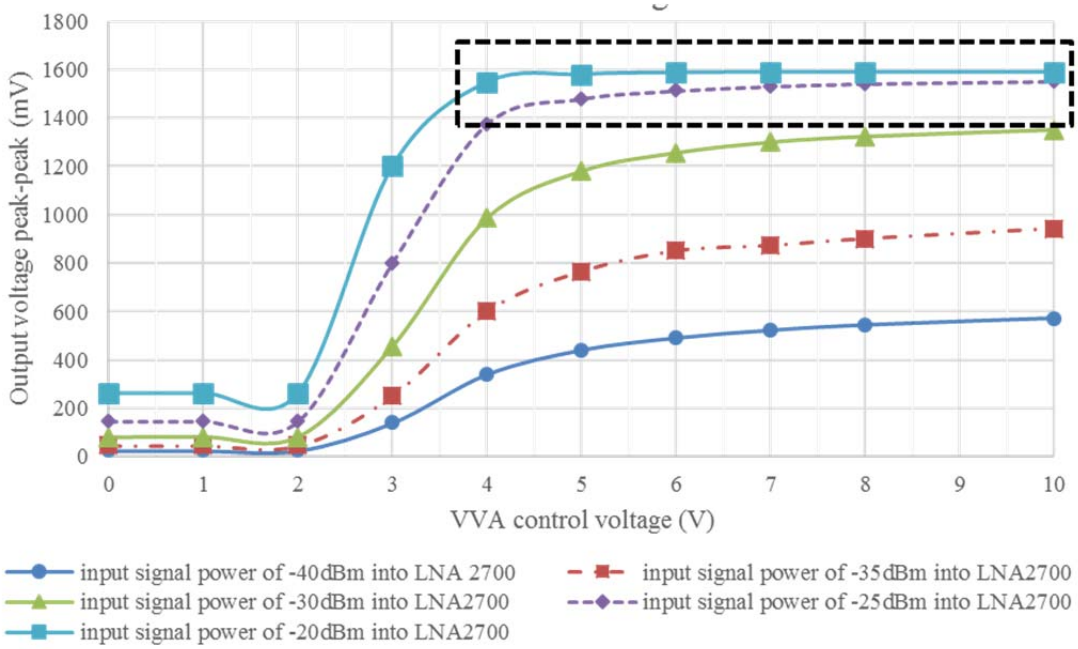

Figure 46. LNAs Cascade Response Measured from Output of LNA 8G against VVA Control Voltage $V_{control}$

In Figure 46, the dotted box shows that the LNA 8G has gone into 1-dB compression. When the input signal power is greater than −25.0 dBm, higher attenuation must be introduced by VVA by setting the $V_{control}$ between 2.0 and 3.5 V.

B. SINGLE CHANNEL AND REFERENCE CHANNEL INTEGRATION

The microwave-photonic front-end of the DF system consists of three measurement channels and a reference channel. Before the entire MWP DF system was assembled, a systematic approach was adopted to construct each channel path. Once an individual channel was constructed as shown in Figure 47, measurement and testing was conducted to record the signal output at different junction locations. These measurements for a single channel served as a basis for construction of the other two channels. Components that deviated significantly from specifications were replaced. Since signal attenuation occurs at connections between cables, components and connectors, having a basis measurement result allowed us to trace the losses for retrofit actions.

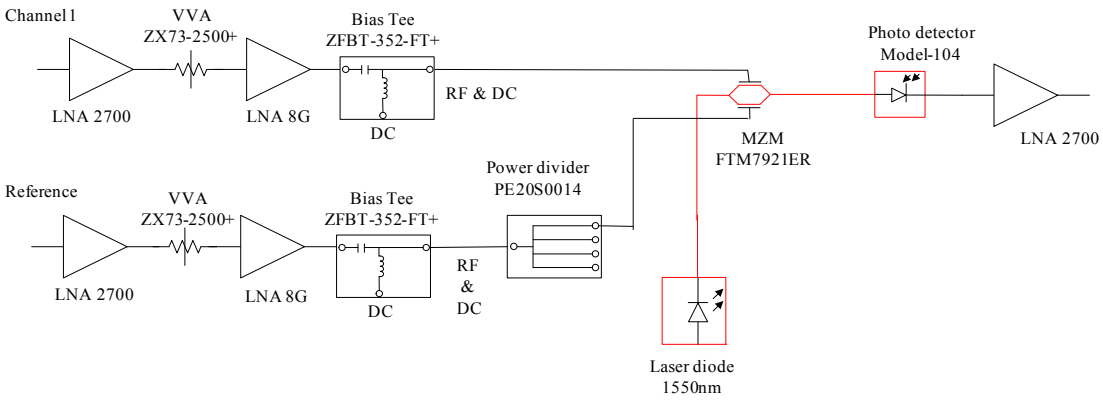

Figure 47. Single Channel and Reference Channel Integration

A sinusoidal input signal of −35.0 dBm at 2.4 GHz was injected into the input of the LNA 2700 for channel 1 and the reference channel. The output measured from the LNA 2700 was 161.87 mV_{pp}, or equivalently −11.9 dBm, which is consistent with what is expected when compared to Figure 22.

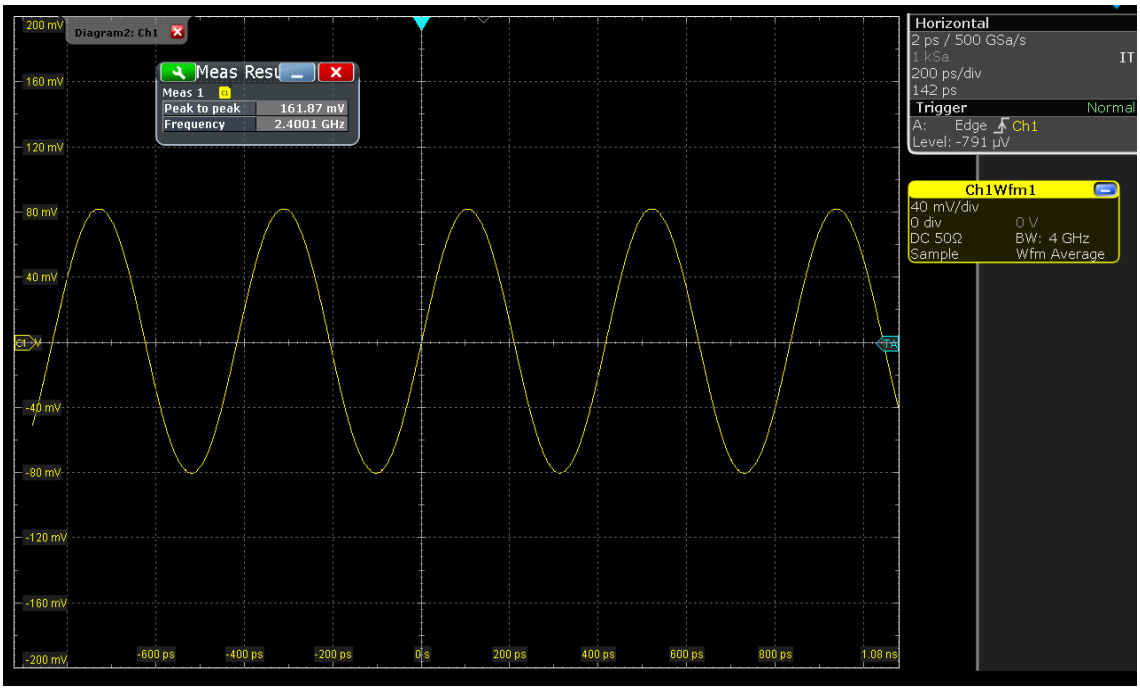

Figure 48. Output Signal Measured after LNA 2700

If the signal at the LNA 2700 output of −11.9 dBm is injected directly into the LNA 8G, the LNA 8G goes into 1-dB compression, as seen in Figure 23. With the relationship shown in Figure 46, the VVA was set at 3.5 V so that the LNAs do not operate in the 1-dB compression mode, giving an output of 0.42 V_{pp}. The output signal measurement recorded after the LNA 8G was 0.46 V_{pp}, as shown in Figure 49, is close to what was expected.

For the reference channel, the VVA control voltage was set to 6.0 V to achieve a 0.8 V_{pp} output signal. From Table 10, we know that the reference signal is split almost equally after passing through the four-way power divider, and the signal amplitude was 0.2 V_{pp}.

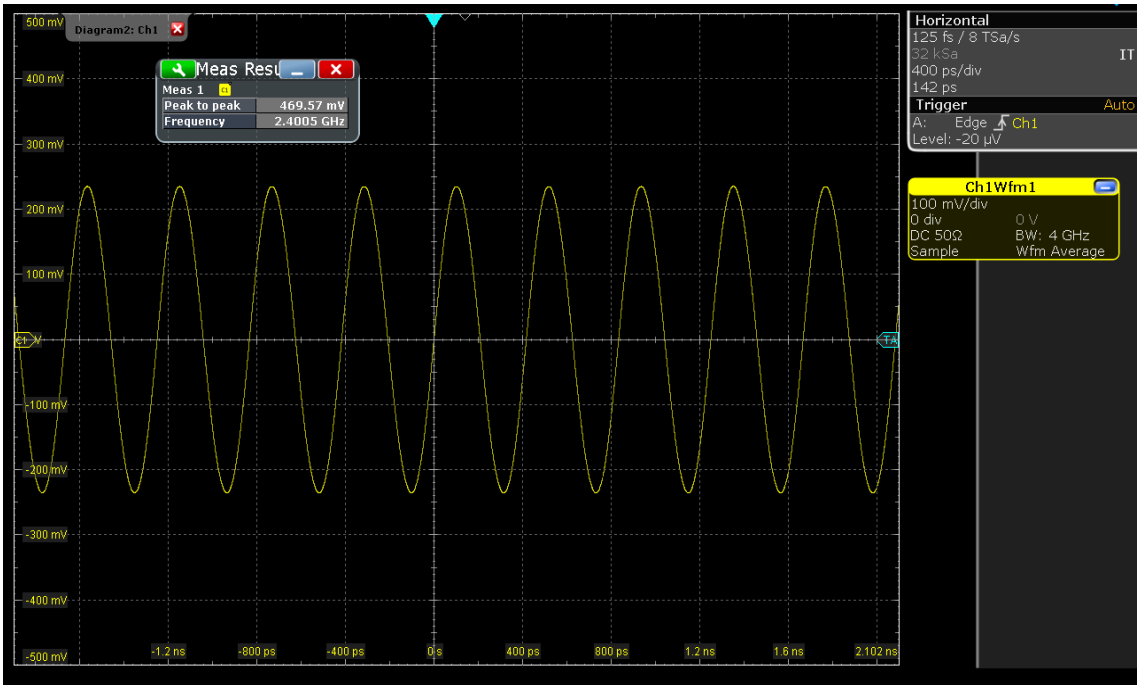

Figure 49. Output Signal Measured after LNA 8G

A bias voltage of 0.6 V was added to channel 1 before being sent to one of the electrode arms of the DE-MZM. The reference signal was connected to the other arm of the DE-MZM. The signal with the 0.6V bias voltage added to it is shown in Figure 50,

and the amplitude of the signal was reduced as expected due to the insertion loss resulting from the introduction of bias voltage as seen from Figure 29.

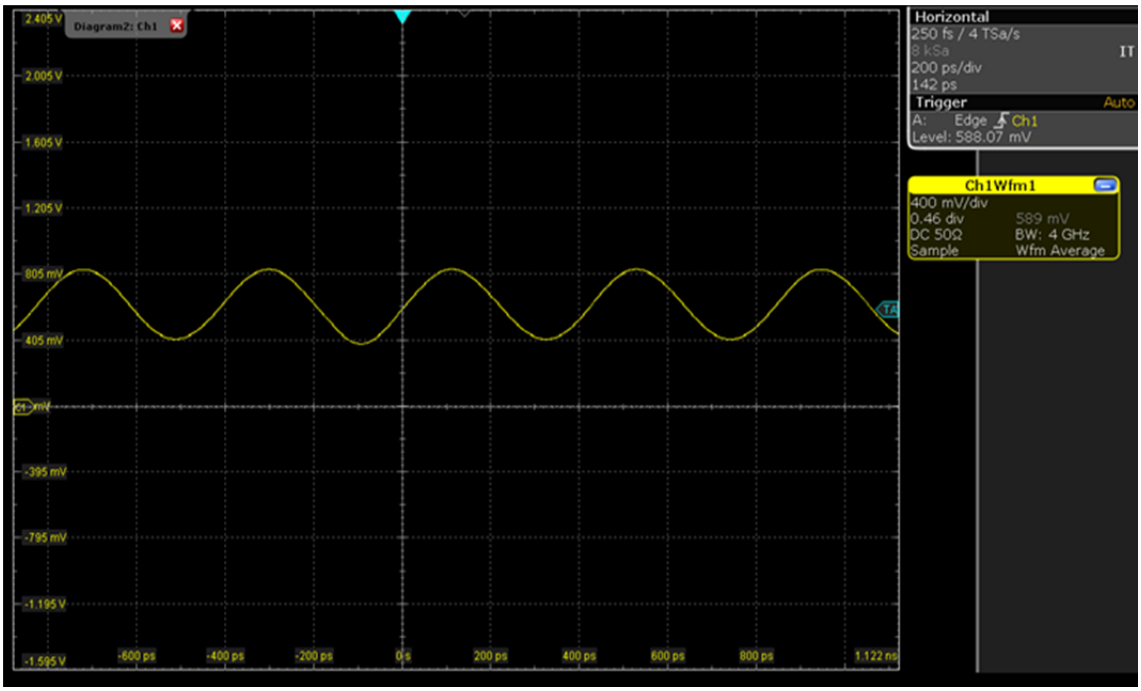

Figure 50. Signal after Bias Tee

The DE-MZM generates a voltage amplitude due to the phase difference between channel 1 and the reference channel. Since the amplitude of the signal was low, the signal was input to the LNA 2700 for amplification, as shown in Figure 51. The amplified signal was sent to the ED to remove the carrier frequency and extract the measured phase difference. A final stage of amplification was carried out by INA114 before supplying it to the CompactRIO for A/D conversion.

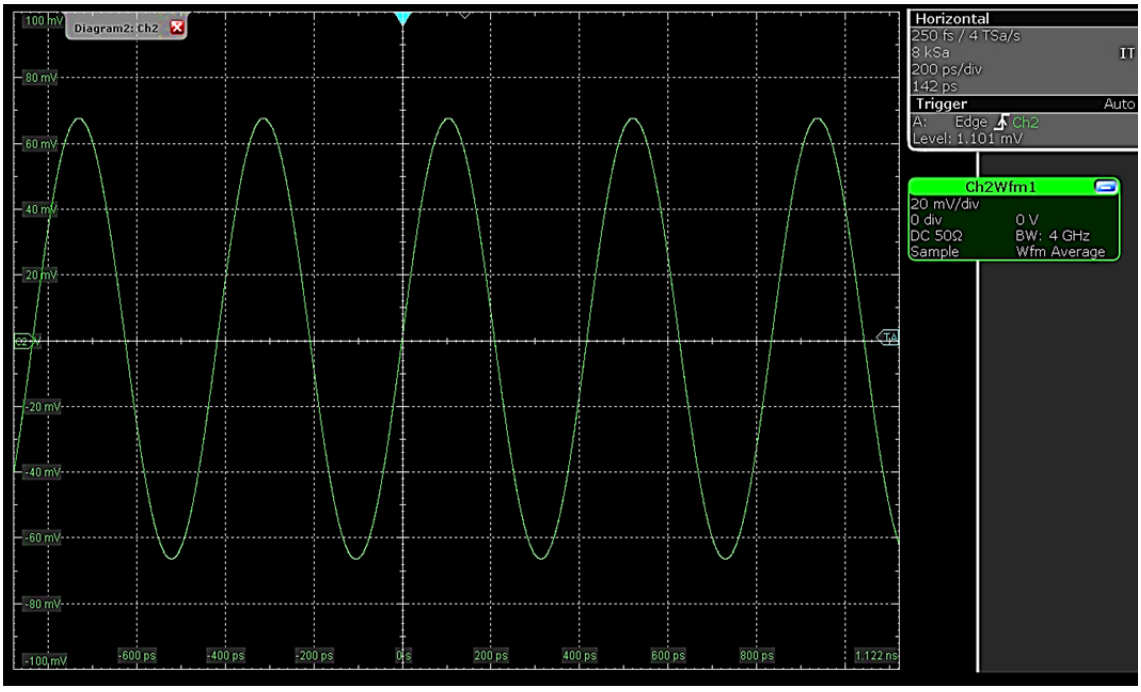

Figure 51. Output Signal Measured after Passing through PD and LNA 2700

Once each channel was constructed and rigorous testing and measurements were completed, they were integrated to form the MWP DF system according to Figure 3.

C. OPERATING FREQUENCY RANGE OF ALL COMPONENTS

During the characterization of components and system integration, we noted that erroneous measurements and data could be collected as a result of testing with signals outside the operating bandwidth. The operating bandwidth is quantified by considering the consolidated operating frequency of each component used in the MWP DF system as shown in Table 12.

Table 12. Operating Frequency Range of Components Used for MWP DF System

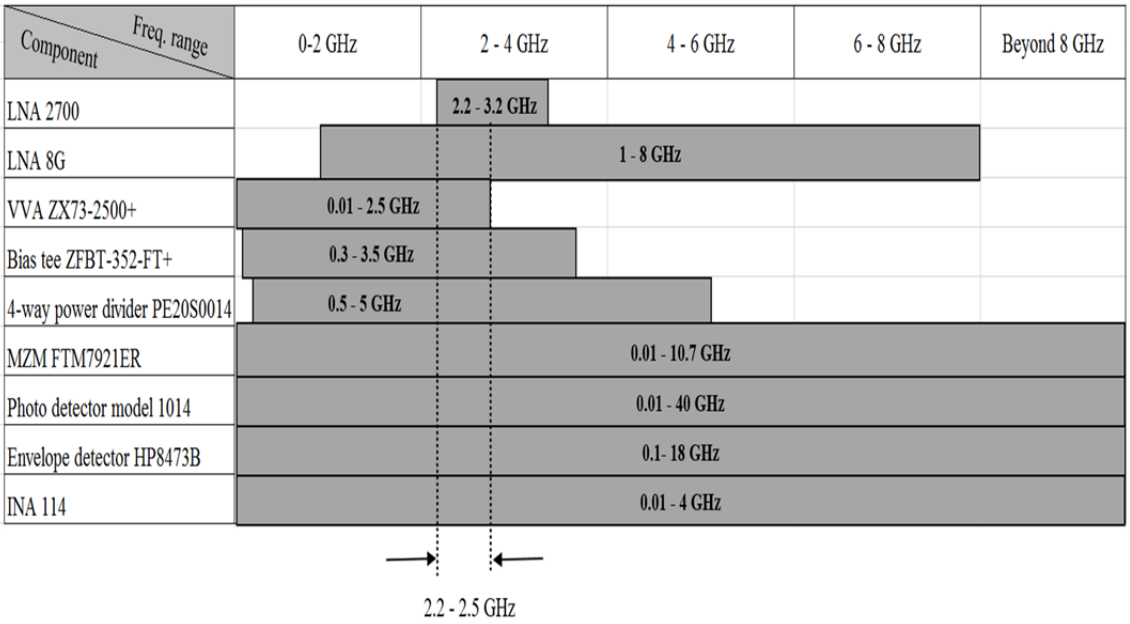

As we can see from Table 12, the existing system is designed to operate in the frequency range of 2.2 GHz to 2.5 GHz due to the limitations of the LNA 2700 and the VVA ZX73-2500+; therefore, most measurements were carried out with a frequency of 2.4 GHz. If we need to operate the system beyond 2.2 GHz to 2.5 GHz, the LNA 2700 and the VVA ZX73-2500+ will have to be replaced with components that offer a wider frequency operating range.

In this chapter, the details of the single channel integration and measurements were discussed. In addition, we also discussed the importance of operating the cascade of fixed gain LNAs to operate in the linear region. The system performance of the integrated MWP DF system which was carried out in the anechoic chamber is discussed in the next chapter.

VII. EXPERIMENTAL RESULTS

Once the MWP DF system was integrated and tested in the laboratory, the system performance was measured in the anechoic chamber. An overview of the anechoic chamber and the setup requirements are provided in this chapter. The procedure to calibrate the MWP DF system prior to any measurement is also discussed. After the calibration, the system was tested using a 2.4 GHz sinusoidal signal, with the signal outputs captured at various measurement points. This provided a better understanding of the expected results as the signal flows through the system. The MWP DF system was eventually tested using LPI signals with the results captured and discussed.

A. ANECHOIC CHAMBER

The performance of the assembled MWP DF system was measured in the anechoic chamber located in Spanagel Hall, Room Sp-604, at the Naval Postgraduate School in Monterey, California. The purpose of the anechoic chamber is to isolate the system from any RF signals from outside the chamber and prevent interference. To minimize reflected RF energy from within the enclosure, radiation absorbent material was used to cover the interior surface.

A transmission antenna (Tecom 201302) was mounted at one end of the chamber, as seen in Figure 52. The MWP DF system was mounted on top of a rotatable pedestal at the other end of the chamber as shown in Figure 53. The distance between the transmission antenna and the receiving antenna was 5.7 m. The computer to control the pedestal's angle of rotation was located outside the chamber.

Ideally, RF measurements are conducted in the far-field region so that the fields radiating from the transmission source appear to be plane waves at the receiver. For the receiver to be in the far-field region, the following three conditions must be met [36]:

$$r > 2D^2 / \lambda , \tag{11}$$

$$r > 1.6\lambda , \tag{12}$$

and

$$r > 5D , \tag{13}$$

where D is the diameter or largest dimension of the transmitting or receiving antenna, and r is the distance between the transmitting and receiving antennas. The test frequency used was f = 2.4 GHz, where λ = 0.125 m. The parameters D and r were measured to be D = 0.3 m for the transmitting antenna, D = 0.22m for the receiving antenna, and r = 5.7 m. Substituting these parameters into (11), (12), and (13), we see that the antennas are in each other's far-field region.

Figure 52. Transmission Antenna (Tecom 201302) Used in Anechoic Chamber

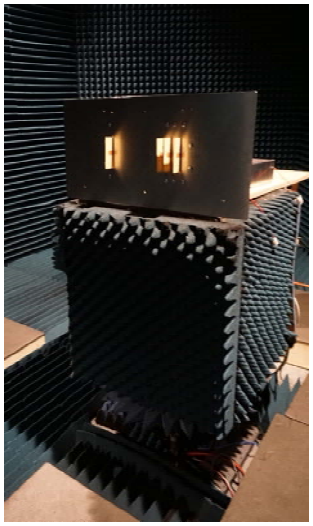

Figure 53. Placement of MWP DF System on Top of the Rotatable Pedestal

The received power P_r at the antenna element in free space can be computed using the one-way Friis equation [37]

$$P_r = \frac{P_t G_t G_r \lambda^2}{(4\pi)^2 r^2 L_t L_r}, \tag{14}$$

where P_t is the transmit power, G_t is the gain of the transmission antenna, G_r is the gain of the receiver antenna, r is the distance between the transmission antenna and the receiving antenna, L_t is the loss from the transmitter to the antenna, and L_r is the loss from receive antenna to receiver. For measurements, depending on the transmit power P_t, the actual received power P_r can be cross referenced using Figure 88 in Appendix A, which is computed using (14).

B. CALIBRATION OF THE SYSTEM

Before commencement of measurement, the MWP DF system had to be calibrated by aligning the MWP DF system 0° relative to the transmission antenna as seen in Figure 54. When the RF signals were transmitted, the antenna elements from Channels 1, 2, 3, and the reference channels converted the received RF into electrical signals with different amplitude levels and phases. Since the thesis research focus is to compare the amplitude difference between the individual antenna channels against the reference channel to determine the AOA, the amplitude for all the antenna channels must be matched. In addition, bias voltages must be set based on the signal amplitudes of the three antenna channels. To achieve calibration, the following steps were carried out:

1. The R&S RTO2000 digital oscilloscope was connected to the output connectors from Box 2 to view the signal outputs from the bias tees.
2. A multimeter was connected to the voltage divider located in Box 1 to measure the voltage level for $V_{control}$. The voltage divider was tuned to achieve the attenuation for the VVA in order to match the amplitudes of all the channels. Figure 46 was used as a reference to ensure the LNA 8G did not operate in the 1-dB compression region.
3. The potentiometer in Box 2 was adjusted to provide the required bias tee voltage for the three channels.

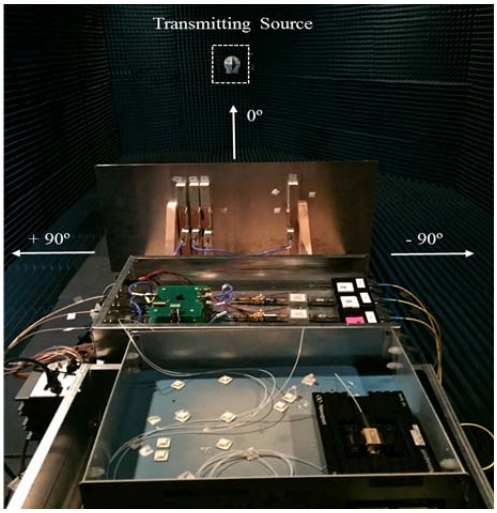

Figure 54. DF System Aligned 0° Relative to the Transmitting Source for Calibration

The calibrated signals for the three channels measured from the output of the bias tee were as shown in Figure 55. Waveforms shown in green, orange, and blue correspond to antenna Channels 1, 2, and 3, respectively. From Figure 55, we see that all the signal amplitudes were matched. The V_{π} for the DE-MZM was approximately 440 mV. For the DE-MZM to operate in the linear region, the V_{bias} should be at the midpoint between 0.0 V and V_{π} or at any odd multiple of V_{π} / 2 of the transfer function. For this particular calibration, we chose V_{bias} to be approximately 700 mV.

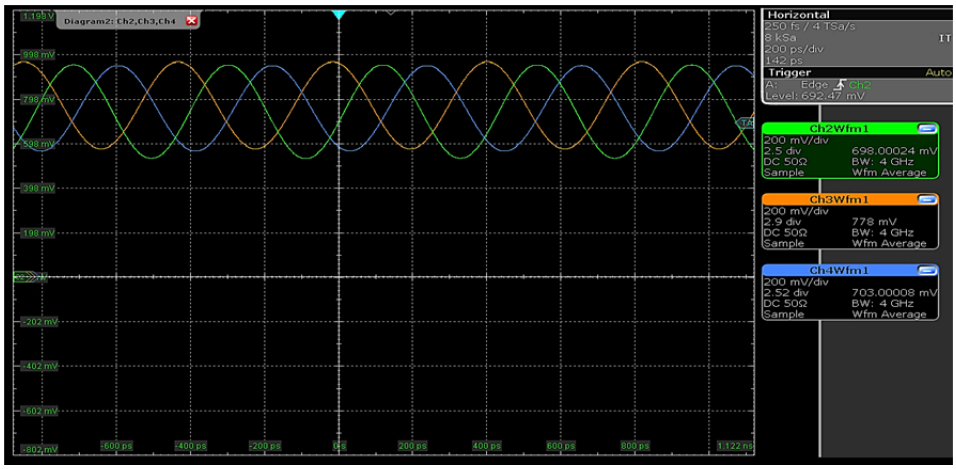

Figure 55. Calibrated Output Measured from Bias Tee

C. TEST MEASUREMENT POINTS

In each test, the signal was measured at four specific locations, as shown in Figure 56. Measurement points 1 and 2 are the output of the LNA 2700 and LNA 8G, respectively. Measurement point 3 is the output from the bias tee for the three signal channels and reference channel. Optical signals were converted into electrical signals after passing through the DE-MZM and PD. The electrical signals were then amplified and measured at measurement point 4.

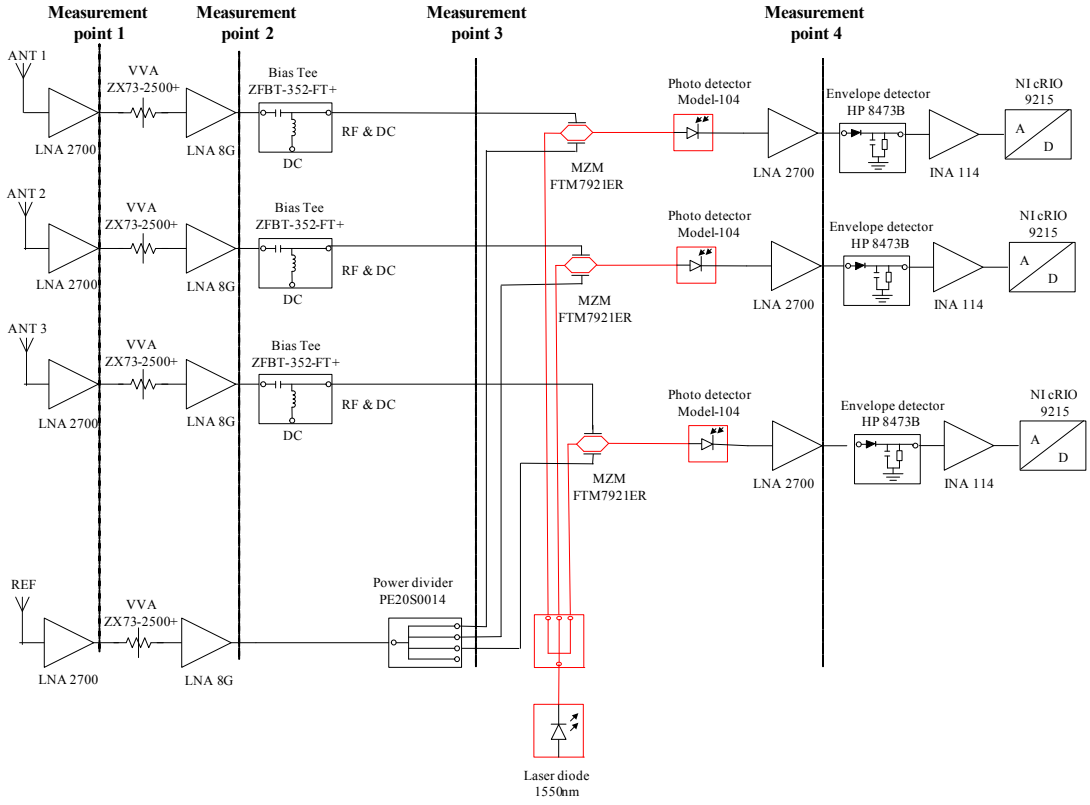

Figure 56. Measurement Points during Testing

D. INTEGRATION AND TESTING USING CW SIGNAL

The signal flow for each single channel was previously described in Figure 48 to Figure 51. The integrated system response for a CW signal is described below.

1. MWP DF System Aligned 0° Relative to Transmission Source

A CW signal with a frequency of 2.4 GHz and power level of 15.0 dBm was generated using the R&S SMW vector signal generator and emitted through the transmission antenna (Tecom 201302). The MWP DF system under test was aligned 0° relative to the transmission source.

The amplified signals at the LNA 2700 output are shown in Figure 57. From Figure 57, we see that the signal amplitude level between the channels was different, especially the signal in orange, which corresponds to antenna element 2. If we refer to Figure 5, antenna element 2 was placed in between antenna element 1 and 3, where mutual interference from antenna elements 1 and 3 resulted in a reduction in the signal amplitude received by antenna element 2.

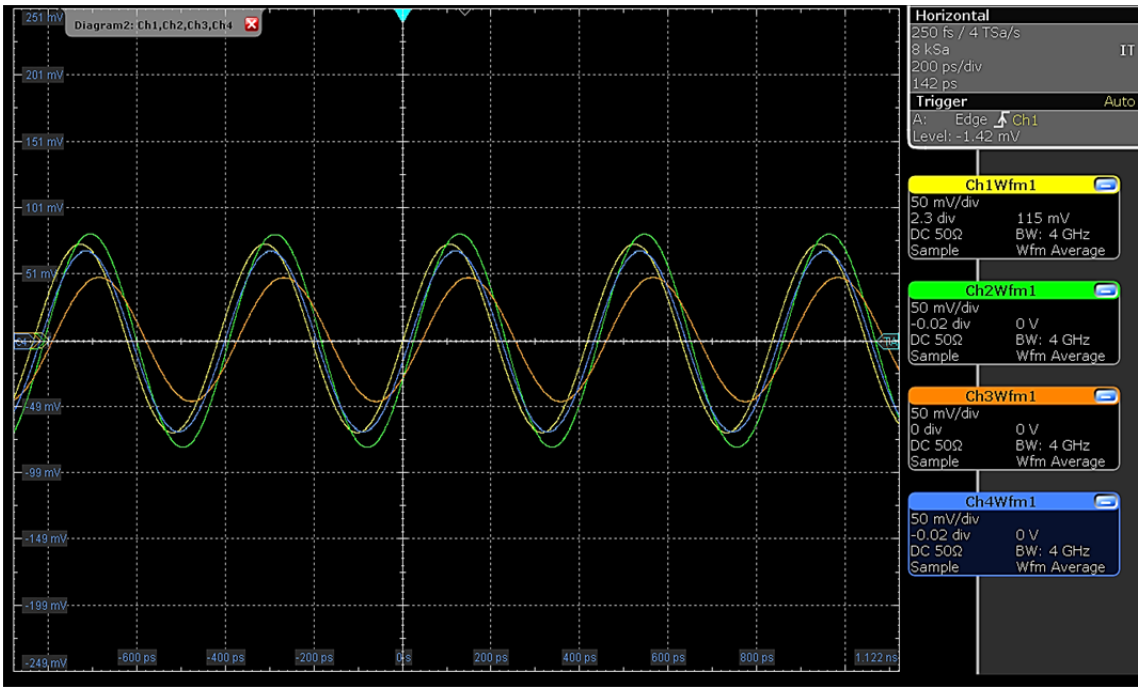

Waveforms shown in yellow, green, orange, and blue correspond to the reference channel and antenna channels 1, 2, and 3, respectively.

Figure 57. Output Signals Measured from Measurement Point 1

All the signals were further amplified after passing through the LNA 8G as shown in Figure 58. The reference channel output was split after passing through the four-way

power divider and the VVA was tuned such that the attenuation to the reference channel was lower as compared to the three signal channels. In addition, the VVA for antenna element 2 was tuned such that its amplitude was matched to antenna element 1 and 3.

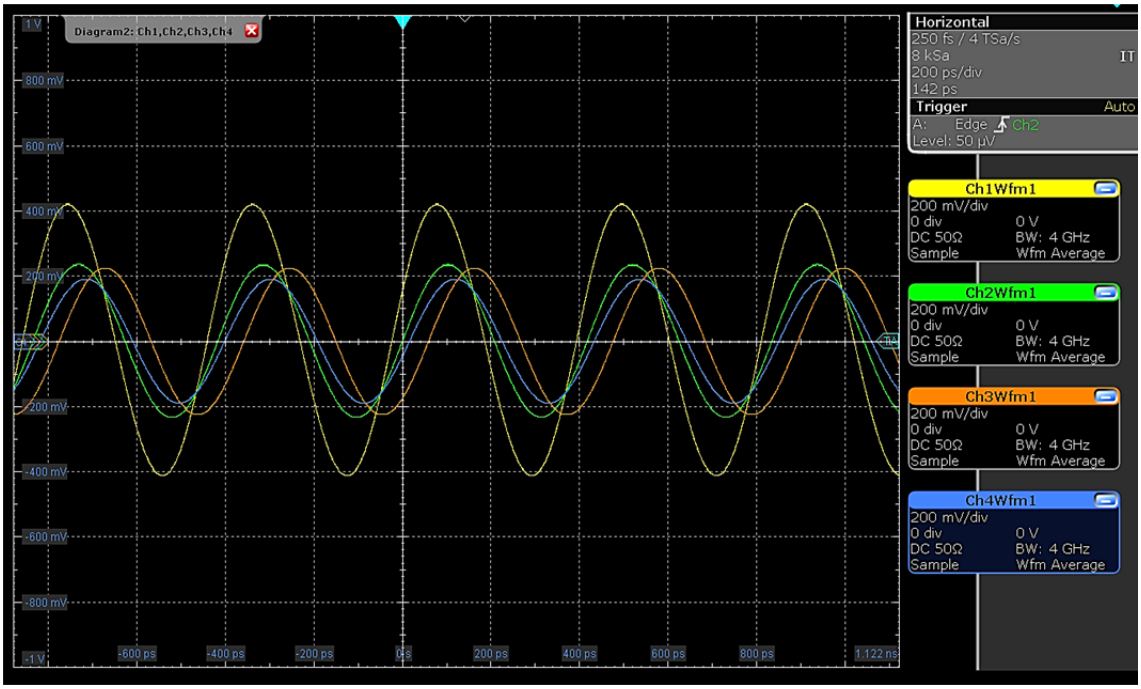

Figure 58. Output Signals Measured from Measurement Point 2

The voltage V_{bias} was introduced to the three channels using the bias tee and was measured at measurement point 3, as shown in Figure 59. All the signal amplitudes were matched to approximately the same level since the DF system baseline was aligned to 0° relative to the transmitting source.

The optical output amplitude from the three DE-MZMs, which corresponded to the phase difference between reference and respective signal channel, were sent to the PD. The optical signals were converted to electrical signals through the PD. Due to the high loss from the conversion process, the signals had to be amplified. The signals captured at measurement point 4 are shown in Figure 60.

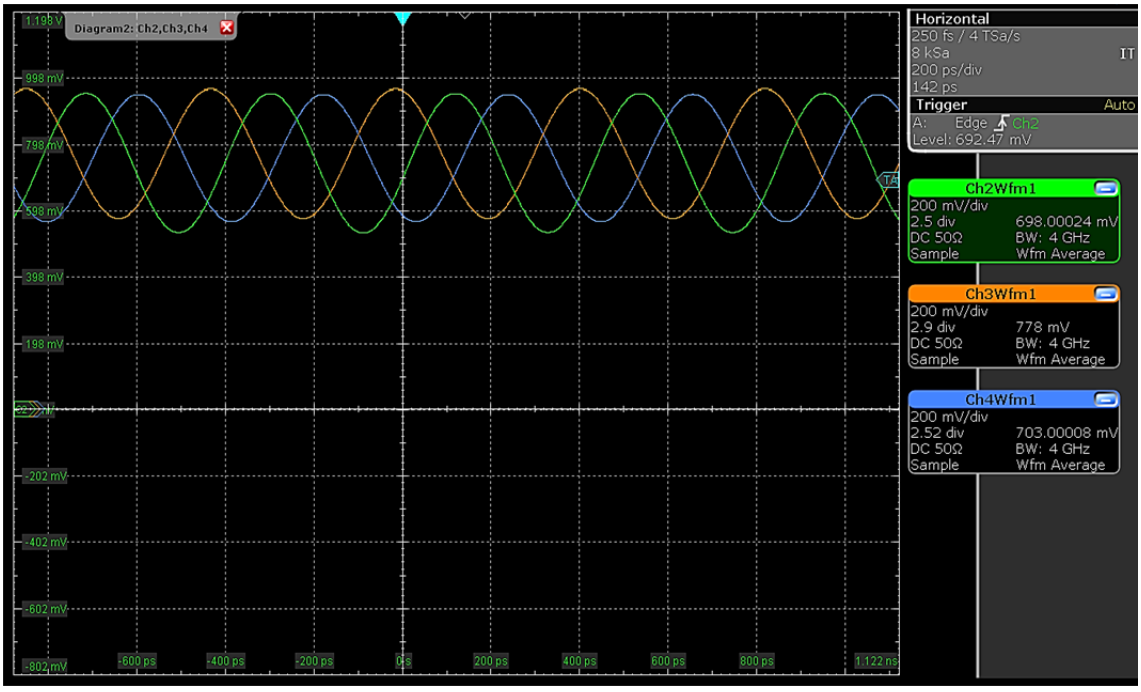

Figure 59. Output Signals Measured from Measurement Point 3

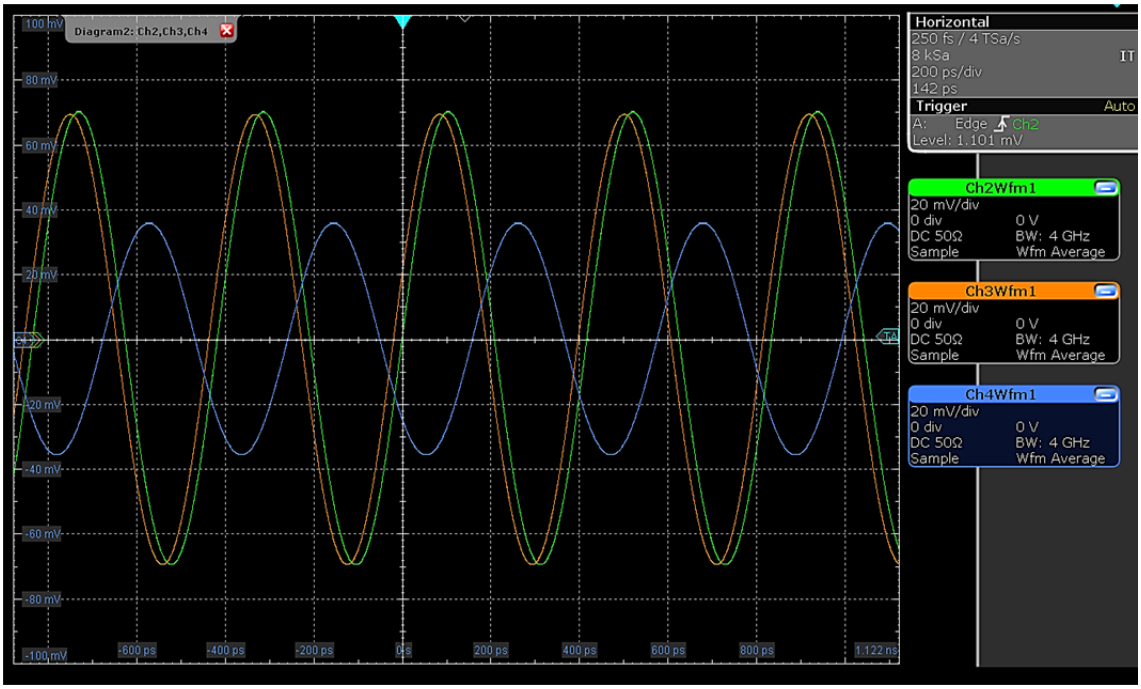

Figure 60. Output Signal Measured from Measurement Point 4

After measurement point 4, the signals were subsequently passed through the ED to extract the envelope amplitude from the PD. These amplitude levels underwent A/D conversion for post processing. The details for post processing minimum Euclidean distance detector for AOA estimation are described in [12].

2. MWP DF System facing −45° and +45° Relative to the Transmission Source

The DF system was rotated to face −45° and +45° relative to the transmission source, and the waveforms measured at measurement point 3 are shown in Figure 61 and Figure 62, respectively. Signals shown in green, orange, and blue correspond to antenna element 1, 2, and 3, respectively. From Figure 61 and Figure 62, we observe that as the DF system rotates from one angle to another relative to the transmission source, the signal strength received by the three antenna elements 1, 2, and 3 varies. The signal amplitudes for the three channels were digitized in the receiver chain to create three values which formed a unique set that corresponded to the AOA from the transmission source. By rotating the pedestal from −90° and +90° relative to the transmission source, we were able to build a database for the AOA for a 180° FOV for the MWP DF system.

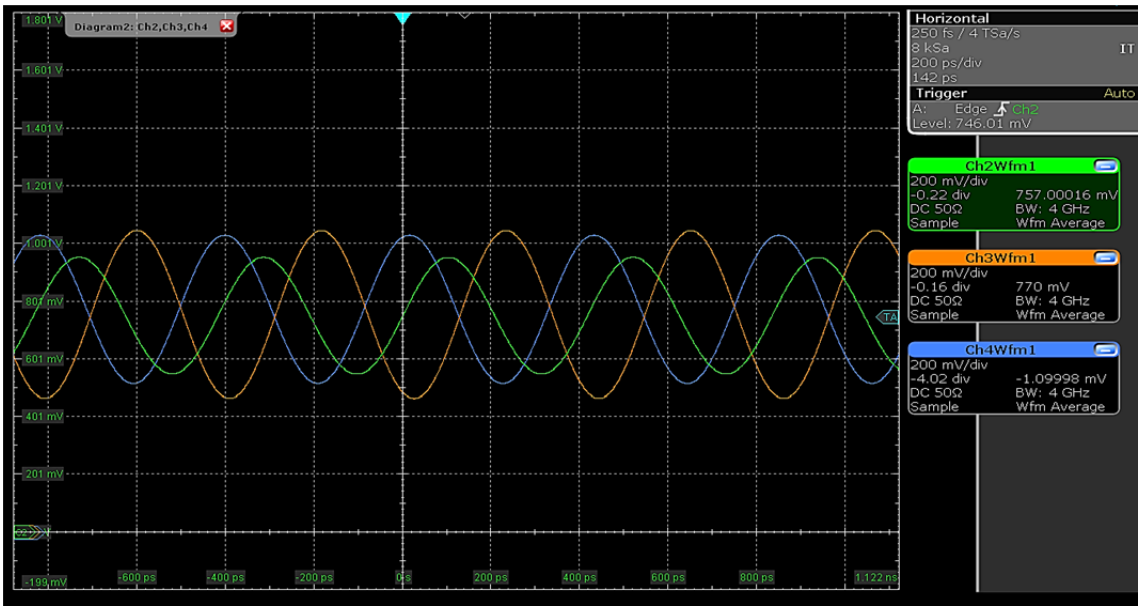

Figure 61. Output Signals Measured from Measurement Point 3 when DF System Faced −45° Relative to Transmission Source

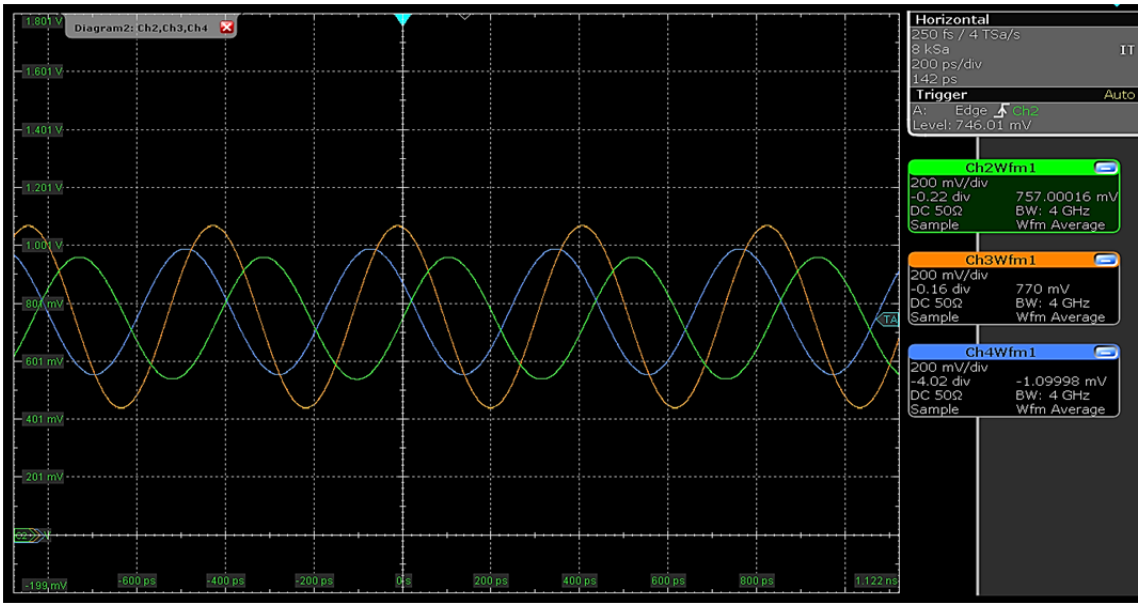

Figure 62. Output Signals Measured from Measurement Point 3 when DF System Faced +45° Relative to Transmission Source

E. TESTS WITH COMPLEX LPI SIGNALS

LPI signals typically possess the characteristics of low power, wide bandwidth, frequency or phase variability, and other design attributes. There are different types of techniques to generate LPI signals. For this thesis research, only two types of techniques are considered. The first is a P4 polyphase modulation, and the second is a frequency-modulated continuous wave (FMCW) signal.

1. P4 Polyphase Modulation

The transmitted complex signal for a phase coded LPI radar is given by [38]

$$s(t) = Ae^{j(2\pi f_c t + \phi_i)}, \tag{15}$$

where A is the amplitude of signal, f_c is the carrier frequency, and ϕ_i is the polyphase modulation. In the case of the P4 codes, the phase ϕ_i of each subcode is computed using

$$\phi_i = \frac{\pi(i-1)^2}{N_c} - \pi(i-1), \tag{16}$$

for subcode i = 1 to N_c where N_c is the number of subcodes within a code period or the processing gain. Using N_c = 64, we plotted the P4 phase ϕ_i versus the subcode index i, shown in Figure 63. From Figure 63, we observe that the phase changes with every subcode change.

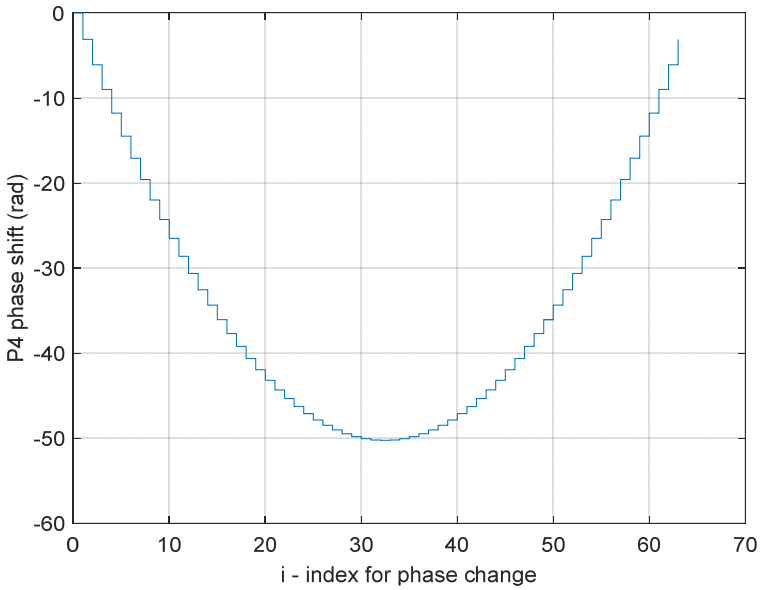

Figure 63. Plot of Phase Sequence ϕ_i versus Index i. Adapted from [38].

a. Test Signal

The P4 test signal was generated using the R&S SMW vector signal generator. The parameters used were f_c = 2.4 GHz with N_c = 64, A = 1, and a signal power of 15.0 dBm. The number of cycles of the carrier frequency per subcode was cpp = 120. A total of 6400 samples were generated for each code period (N_c = 64 phases), and each subcode phase consisted of 100 samples. With a clock rate of 200 MHz and a clock period of 5.0 ns, for 100 samples, a phase change occurs every 500 ns, or 0.5 μs. The in-phase (I) and quadrature (Q) waveforms for the generated P4 signal are shown in Figure 64. As shown in the highlighted red rectangle, the 6400 samples for the 64 phases repeat after one complete cycle.

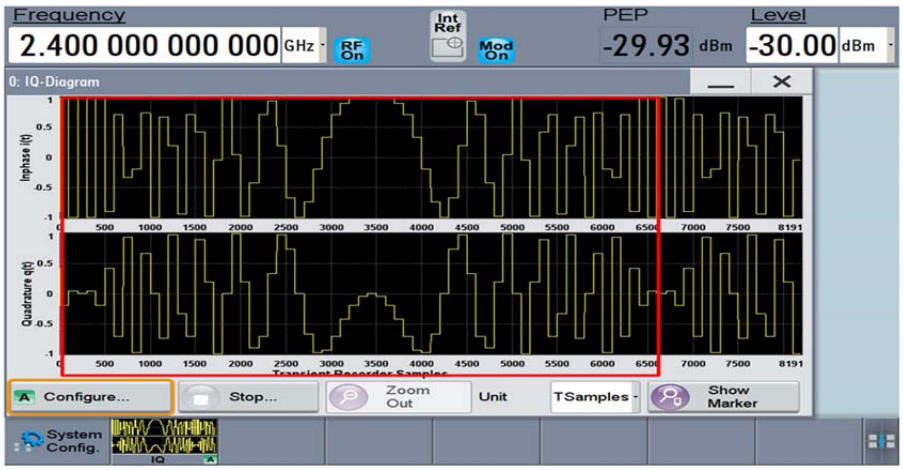

Figure 64. P4 In-Phase and Quadrature Phase Baseband Signals

b. Results

With the DF system aligned to 0° relative to the transmission source during measurement, the signals measured at measurement point 1 are shown in Figure 65, with a phase variation occurring every 500.0 ns, or 0.5 μs. The five times and ten times zoom-in views show the phase variation of the P4 signal, as indicated by the yellow and red dotted boxes, respectively, in Figure 65.

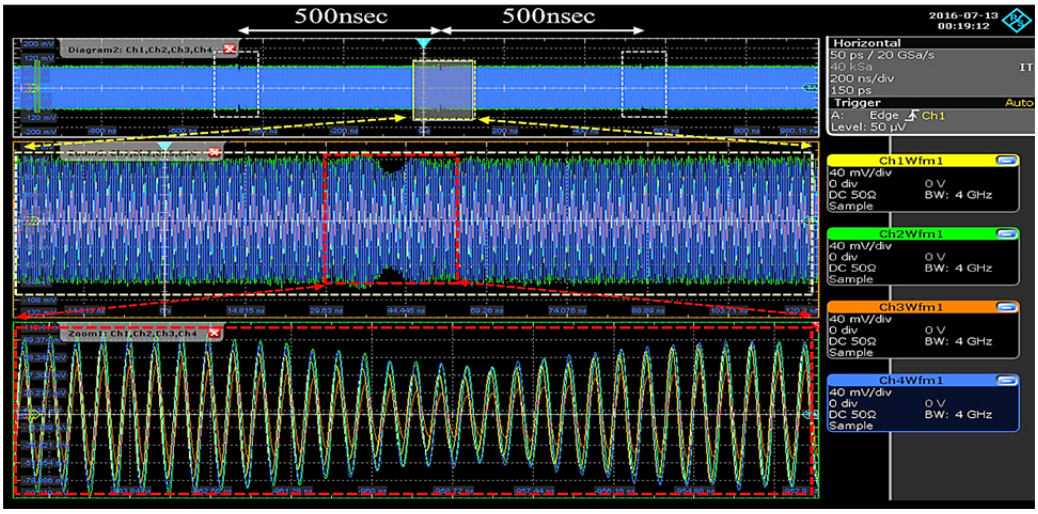

Waveforms shown in yellow, green, orange, and blue correspond to the reference channel and antenna channels 1, 2, and 3, respectively.

Figure 65. P4 Signals Measured from Measurement Point 1

To further investigate the phase variation within the signal, we decluttered Figure 65 to show only the reference channel in Figure 66. From Figure 66, we cannot visually ascertain the polyphase modulation; however, with further post-signal processing, these parameters could be determined.

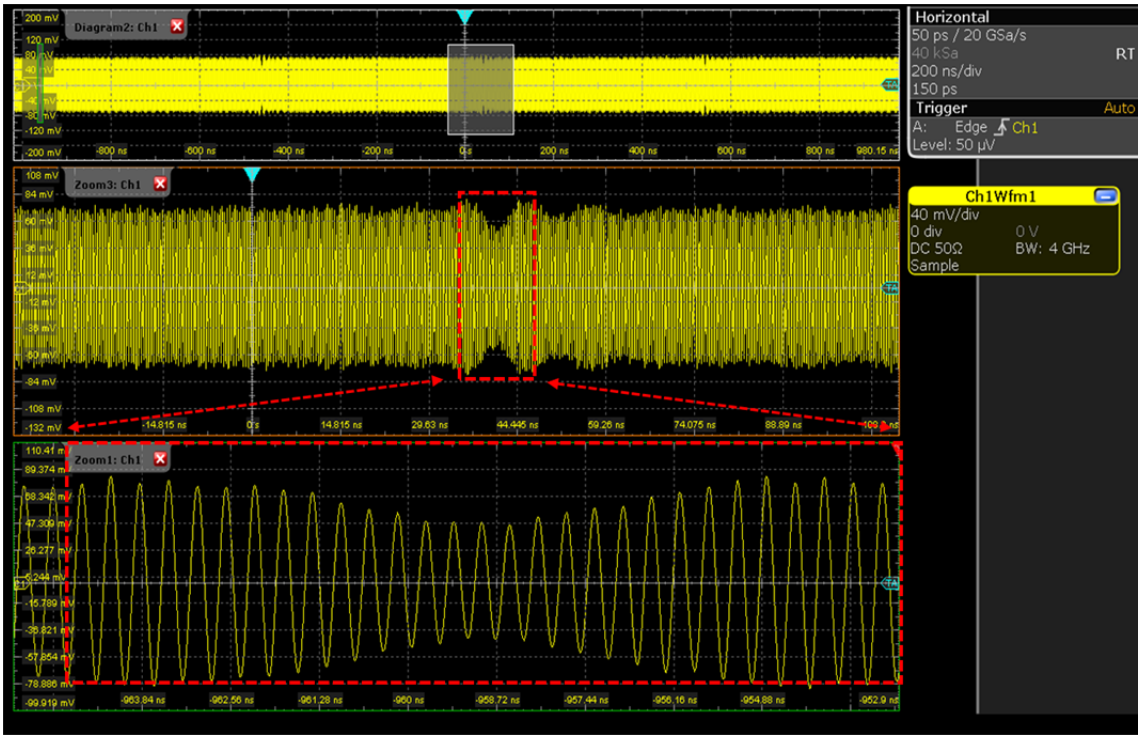

Figure 66. P4 Signal for Reference Channel Measured from Measurement Point 1

Measurement of the P4 signal after the second stage amplification is shown in Figure 67, and the result of after adding the bias voltage the signal is shown in Figure 68. The P4 signals measured at measurement point 4 prior to A/D conversion are shown in Figure 69.

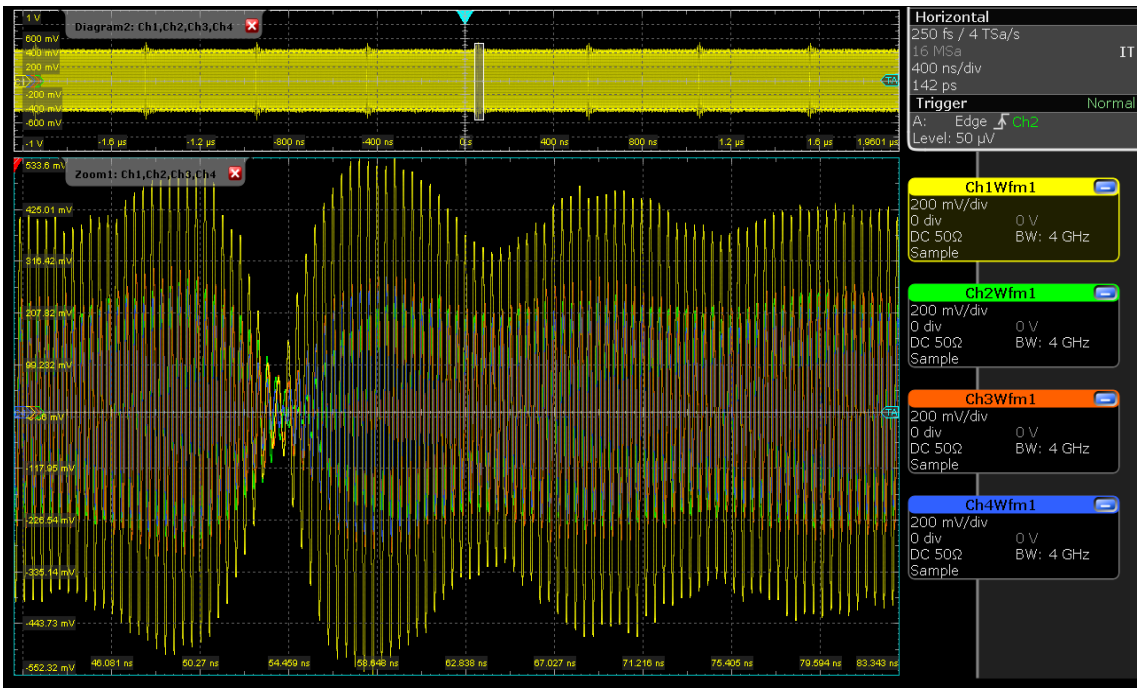

Figure 67. P4 Signals Measured from Measurement Point 2

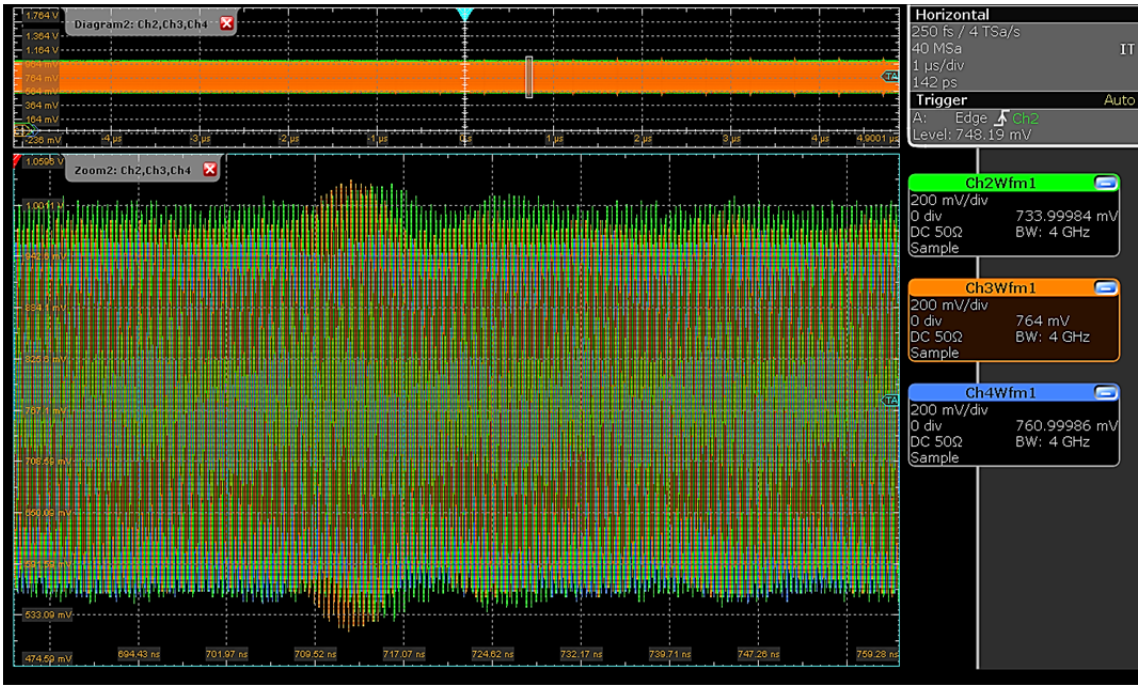

Figure 68. P4 Signals Measured from Measurement Point 3

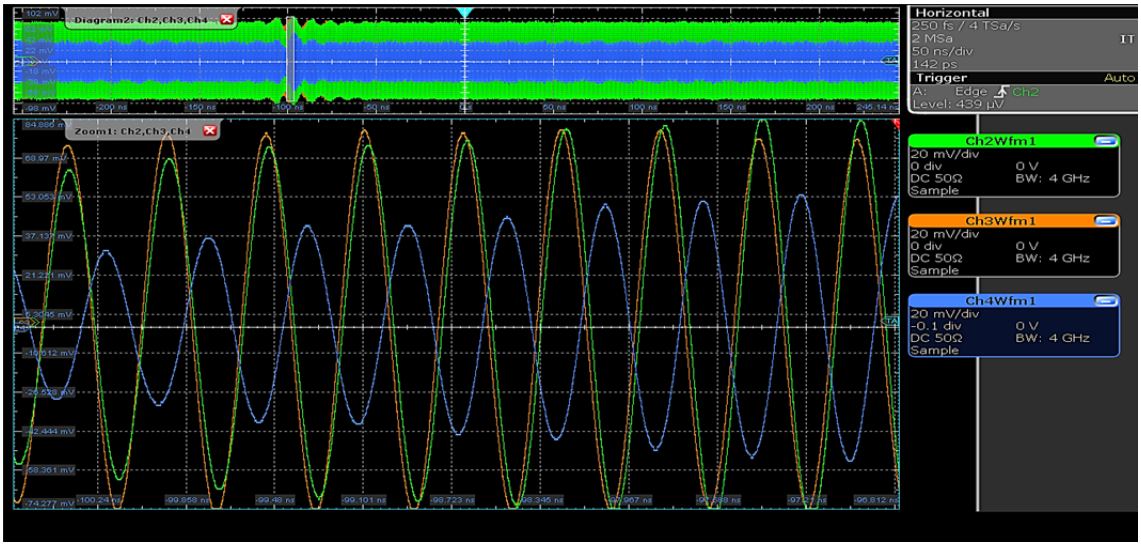

Figure 69. P4 Signals Measured from Measurement Point 4

The post-processed data for the P4 signal after sweeping the MWP DF system from −90° to +90° relative to the transmitting source are shown in Figure 70. From Figure 70, the signal amplitudes for the three channels were digitized to create three values, which formed a unique set that corresponded to the unique AOA of the transmission source. Based on [12], the post analysis using a minimum-Euclidean distance detector for AOA estimation yielded a system capable of detecting the AOA of P4 signals with an RMS accuracy of 0.32°, as shown in Figure 71.

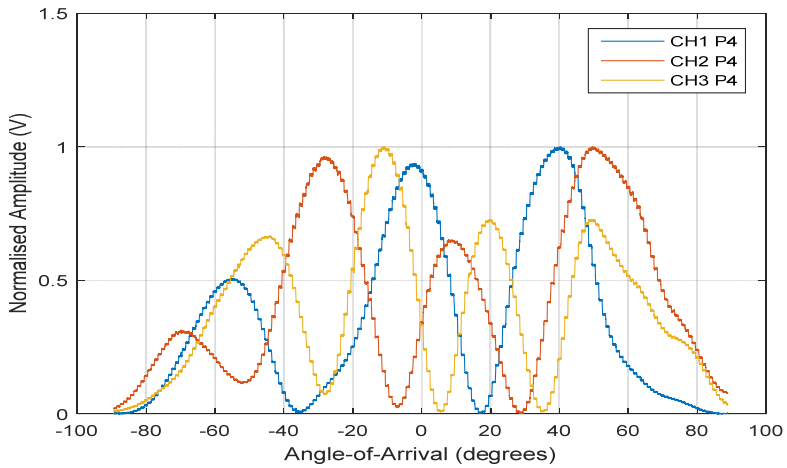

Figure 70. P4 Data after Post Processing and Normalization. Source: [12].

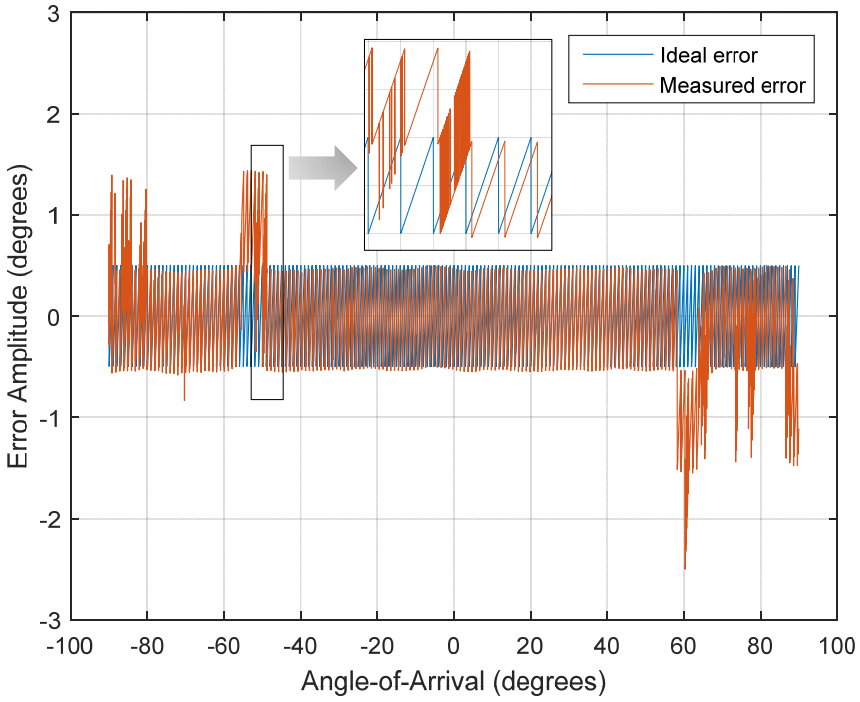

Figure 71. P4 Signal Error Plot. Source: [12].

2. Frequency Modulated Continuous Wave Signal

An FMCW radar works fundamentally like a CW radar in transmitting a continuous power signal, with the exception that the transmission signal is modulated in frequency. By varying the transmit frequency, we can derive the target's range and/or speed based on the frequency of the return signal. Various modulation patterns, such as triangular, sawtooth, square-wave, or stepped modulation, can be used, but for this discussion, the triangular modulation pattern was chosen. For a triangular-modulated FMCW signal, the frequency of the transmitted waveform consists of two parts. The frequency for the first part is [39], [40], [41]

$$f_1(t) = f_c - \frac{\Delta F}{2} + \frac{\Delta F}{t_m} t \ , \tag{17}$$

where f_c is the carrier frequency, ΔF is the transmit modulation bandwidth, and t_m is the modulation period. The frequency for the second part is

$$f_2(t) = f_c + \frac{\Delta F}{2} - \frac{\Delta F}{t_m} t \,. \tag{18}$$

The instantaneous transmitted frequency at any particular time t is shown in Figure 72.

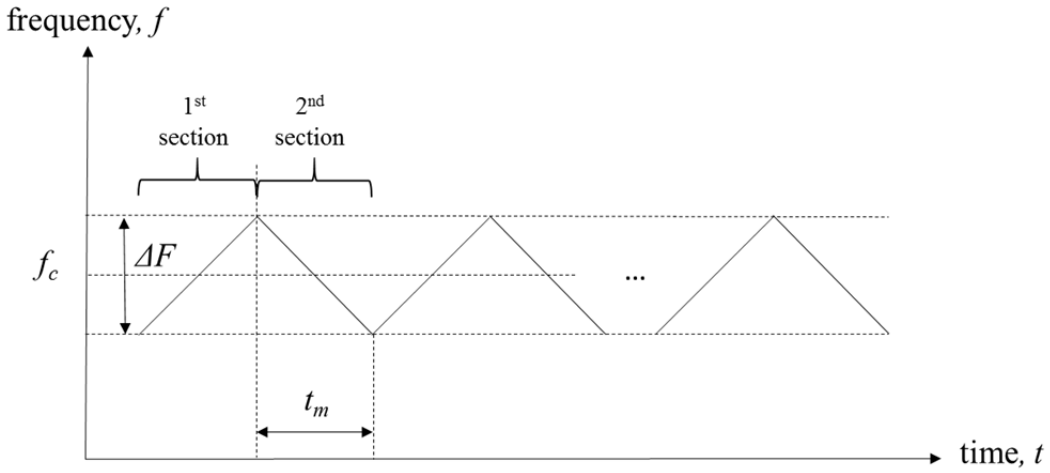

Figure 72. Linear Frequency-Modulated Triangular Waveform. Adapted from [39].

The transmit waveform for the corresponding two parts is:

$$s_1(t) = a_0 \sin 2\pi \left[\left(f_c - \frac{\Delta F}{2} \right) t + \frac{\Delta F}{2t_m} t^2 \right] , \tag{19}$$

and

$$s_2(t) = a_0 \sin 2\pi \left[\left(f_c + \frac{\Delta F}{2} \right) t - \frac{\Delta F}{2t_m} t^2 \right] . \tag{20}$$

a. Test Signal

The FMCW test signal was generated using an R&S SMW vector signal generator. The parameters used were f_c = 2.4 GHz, ΔF = 200.0 kHz, t_m = 100.0 ms, and a signal power of 15.0 dBm. The instantaneous transmission frequency of the transmitted waveforms at two time intervals, $t = t_1$ and $t = t_2$, but with a reduced signal power of

−40.0 dBm as a demonstration, is shown in Figure 73 and Figure 74, respectively. The transmission frequency signal was centered at f_c = 2.4 GHz but was varied within ΔF. The spectrogram in both Figure 73 and Figure 74 displays the linear frequency-modulated triangular waveform, which is similar to Figure 72.

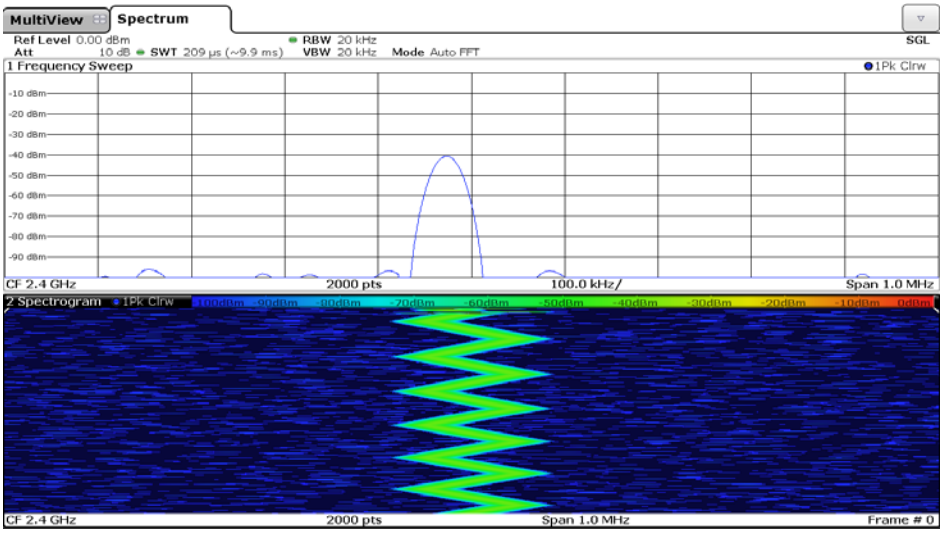

Figure 73. Instantaneous Transmitting Frequency of FMCW Signal in Frequency Domain at $t = t_1$

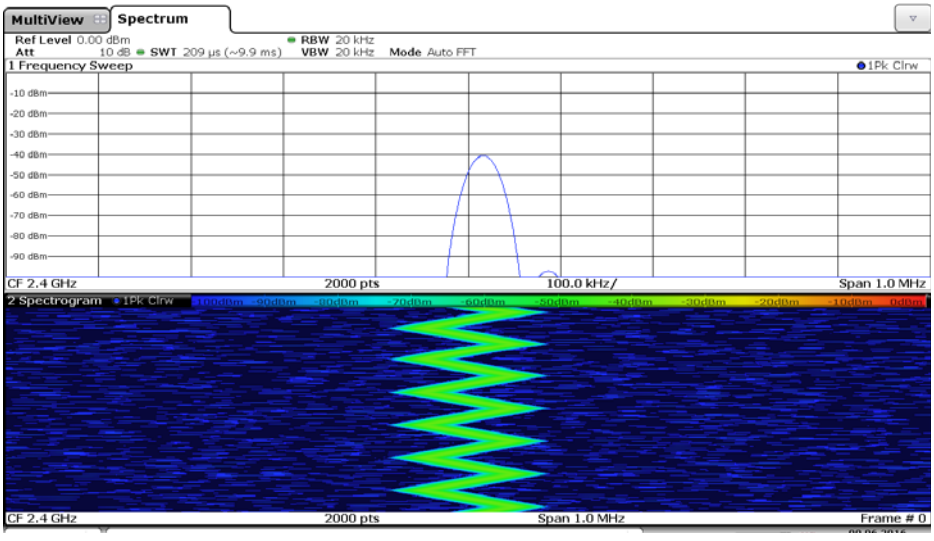

Figure 74. Instantaneous Transmitting Frequency of FMCW Signal in Frequency Domain at $t = t_2$

The time-domain I and Q signals of the FMCW waveforms at $t = t_1$ and $t = t_2$ were generated based on (19) and (20) and are shown in Figure 75 to Figure 76. We observe that the frequency and phase variation between the I and Q waveforms as a result of ΔF and t_m and the combination of both waveforms comprise the instantaneous FMCW signal.

To appreciate what the complete FMCW signal looked like in the time domain, the waveform was captured and is shown in Figure 77.

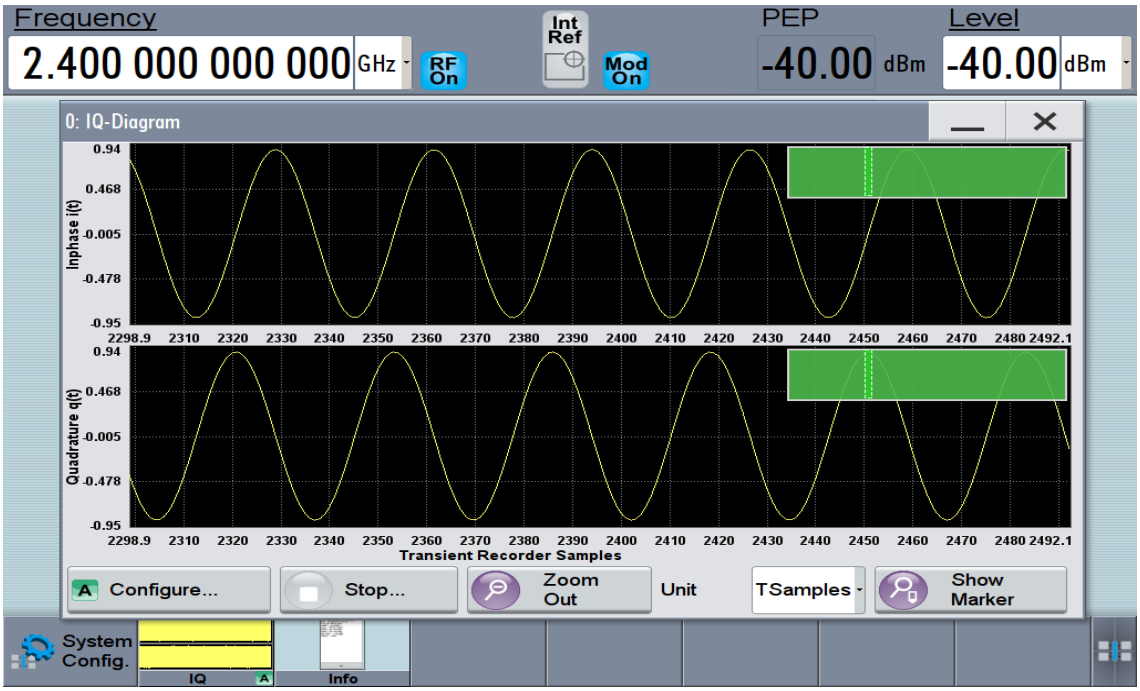

Figure 75. Instantaneous In-phase and Quadrature Waveforms for FMCW Signal at $t = t_1$

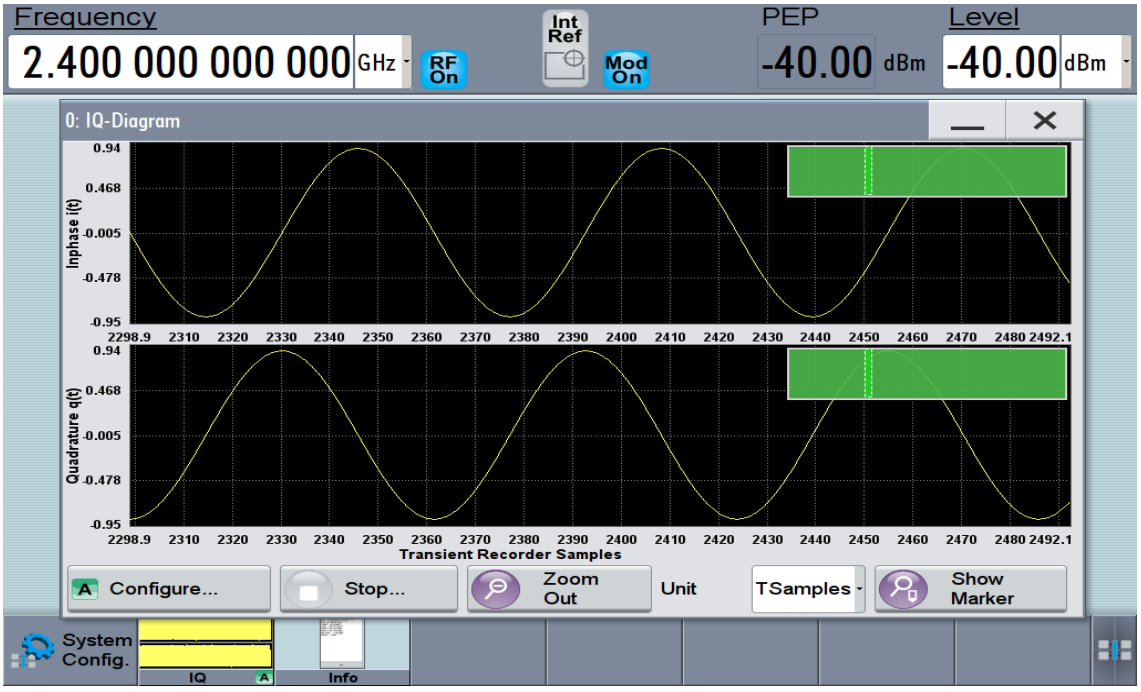

Figure 76. Instantaneous In-phase and Quadrature Waveforms for FMCW Signal at $t = t_2$

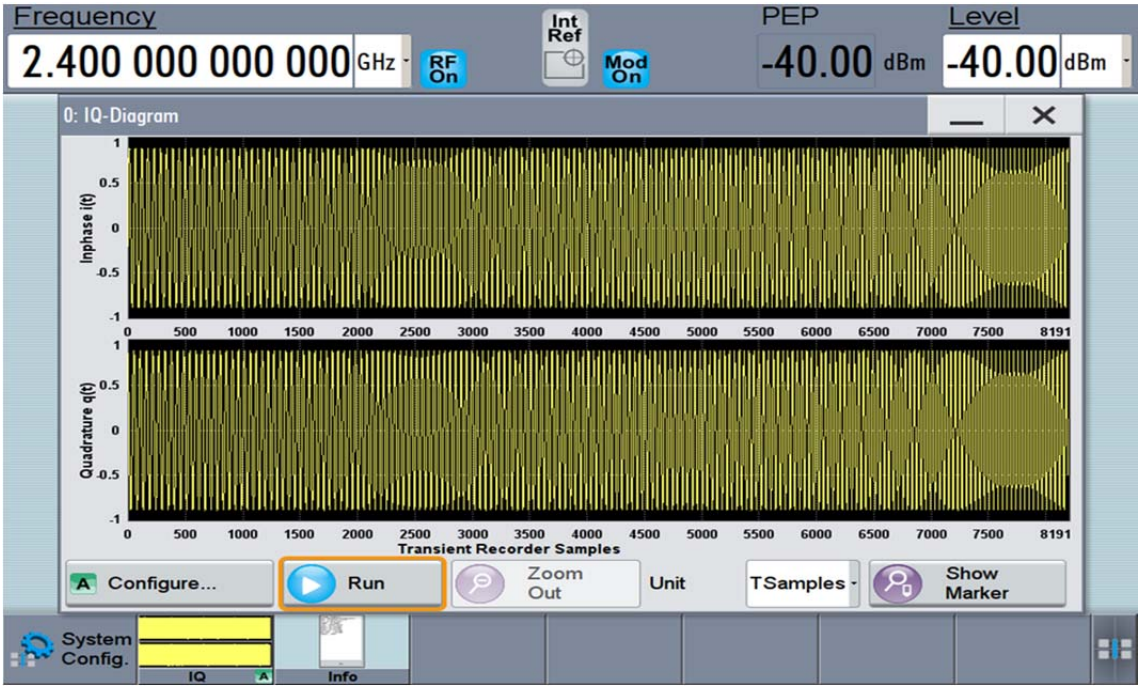

Figure 77. In-phase and Quadrature Waveforms for the FMCW Signal

b. Results

The DF system was aligned to 0° relative to the transmission source during this test. The amplified signals measured at measurement point 1 appeared as a CW signal, as shown in Figure 78. As the test frequency was $f_c = 2.4$ GHz, it was difficult to determine if this was an FMCW with its frequency varying within the transmit modulation bandwidth $\Delta F = \pm 100$ kHz.

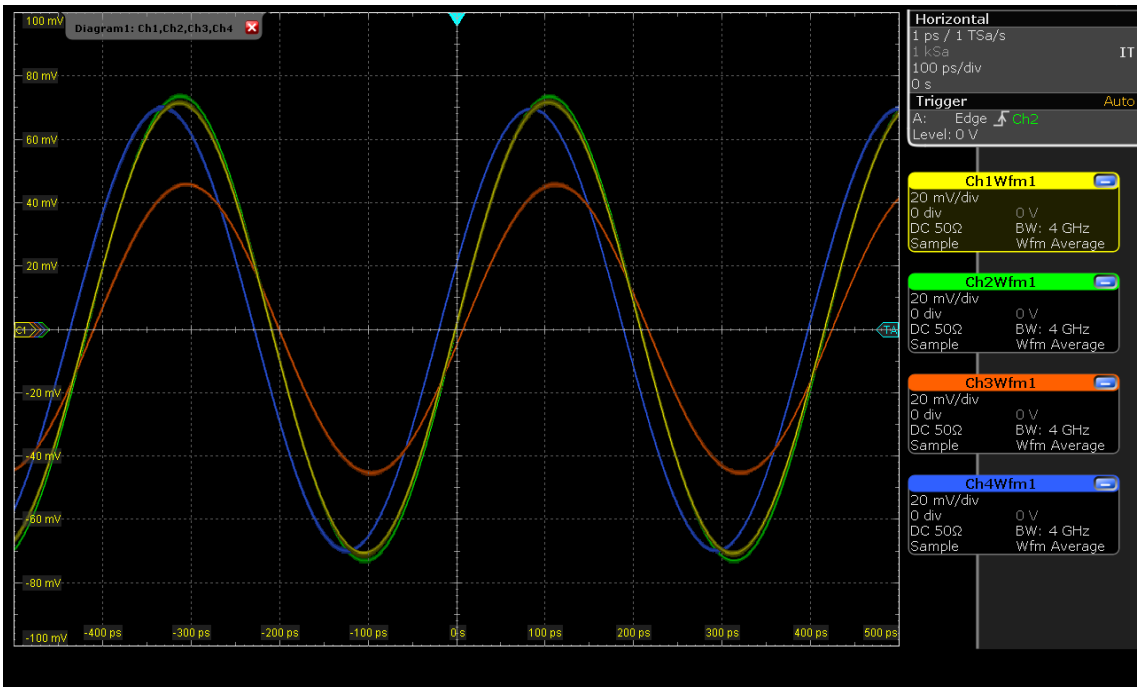

Waveforms shown in yellow, green, orange, and blue correspond to the reference channel and antenna channels 1, 2, and 3, respectively.

Figure 78. FMCW Signal Measured from Measurement Point 1

When we measured the signal in the frequency domain, this slight variation in $\Delta F = \pm 100$ kHz was detected. The reference signal in the frequency domain measured at time $t = t_1$ and $t = t_2$ is shown in Figure 79 and Figure 80, respectively, where we observed the frequency shift of the signal within 100 kHz, with its center frequency at 2.4 GHz.

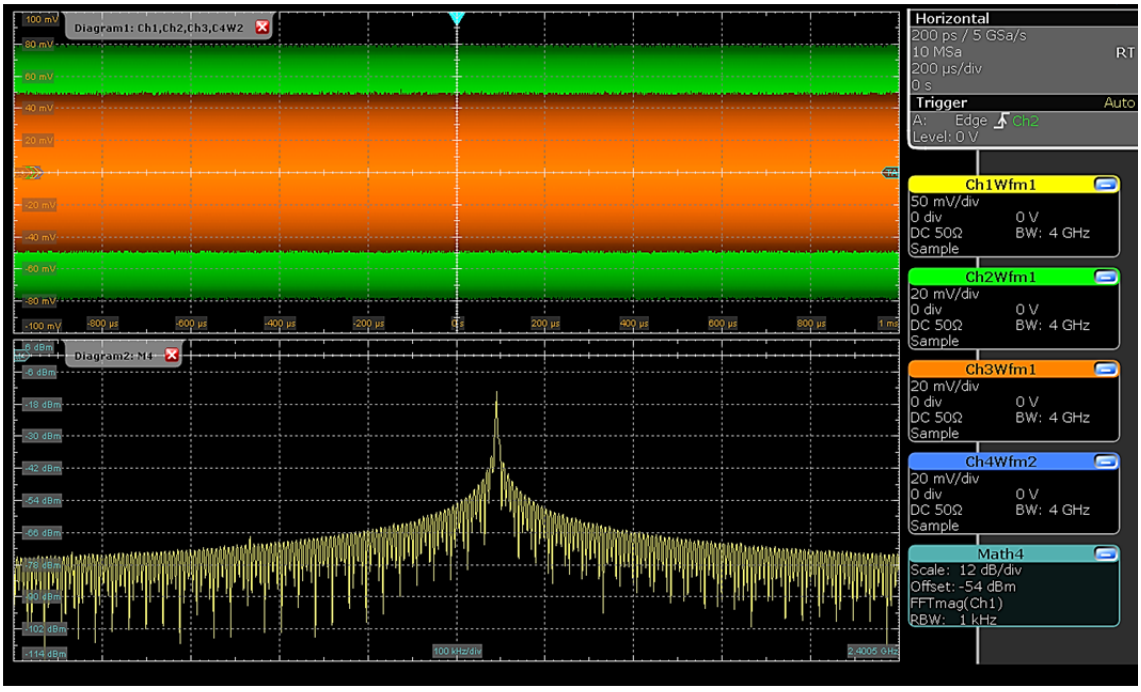

Figure 79. Reference Signal in Frequency Domain Measured from Measurement Point 1 when $t = t_1$

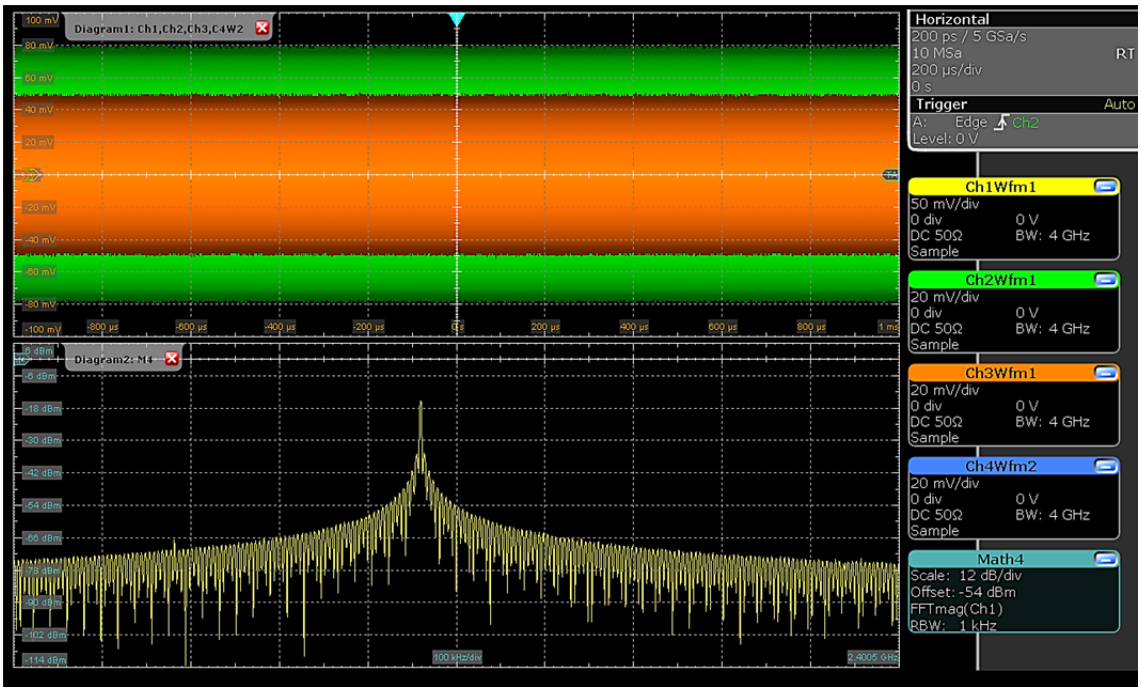

Figure 80. Reference Signal in Frequency Domain Measured from Measurement Point 1 when $t = t_2$

The FMCW signals after the second stage of amplification are shown in Figure 81, and the matched amplitude antenna channels signals captured at measurement point 3 are shown in Figure 82.

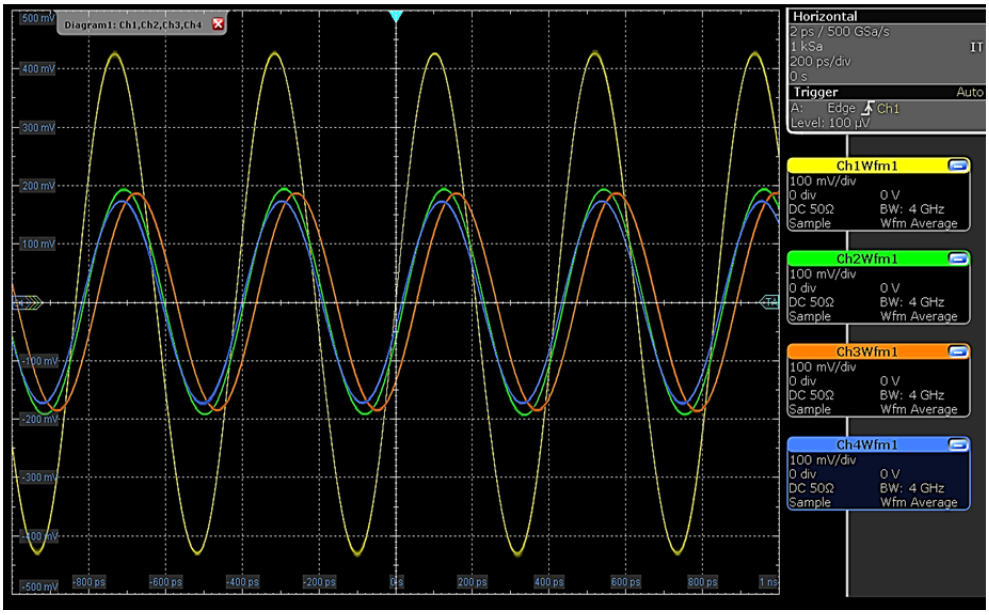

Figure 81. FMCW Signals Measured from Measurement Point 2

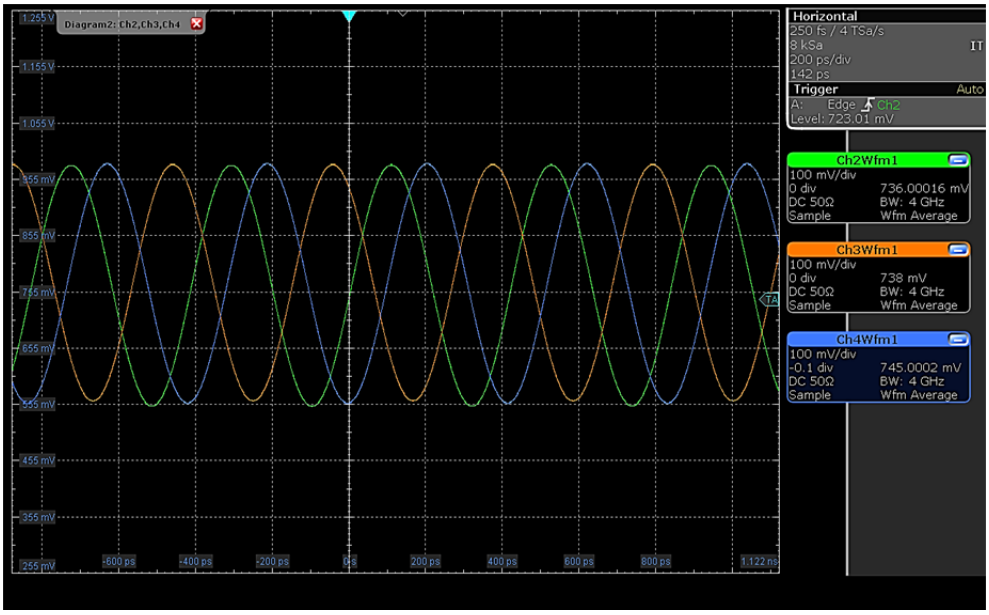

Figure 82. FMCW Signals Measured from Measurement Point 3

The FMCW signals measured at measurement point 4 prior to A/D conversion are shown in Figure 83. The antenna channel 2 response in the frequency domain is shown in Figure 84, where we observe the frequency shifting of the signal within 100 kHz with its center frequency at 2.4 GHz. This reaffirmed the FMCW signal transited through the receiver chain. Apart from that, we were able to confirm that the amplitude measured for antenna channel 2 was 80.0 mV_{pp} in the time-domain signal, as shown in Figure 83, which translates to a signal power of −14.4 dBm in the frequency domain, as shown in Figure 84.

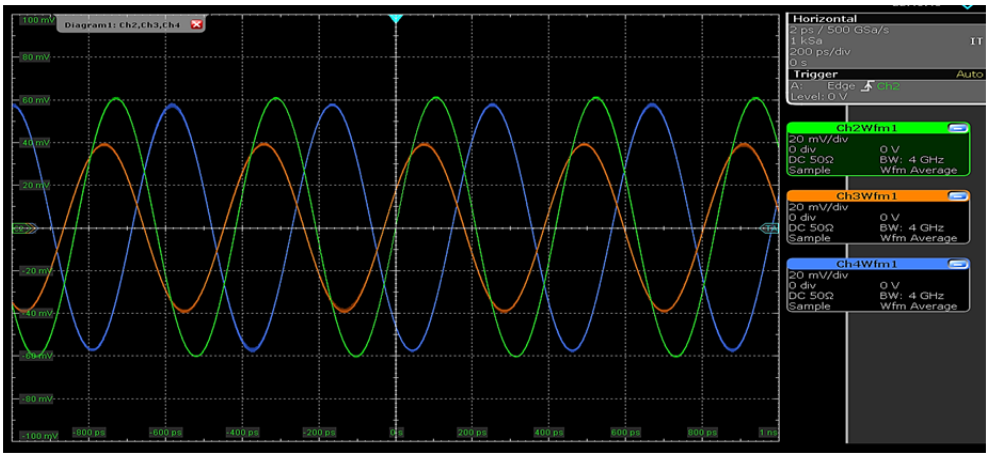

Figure 83. FMCW Signals Measured from Measurement Point 4

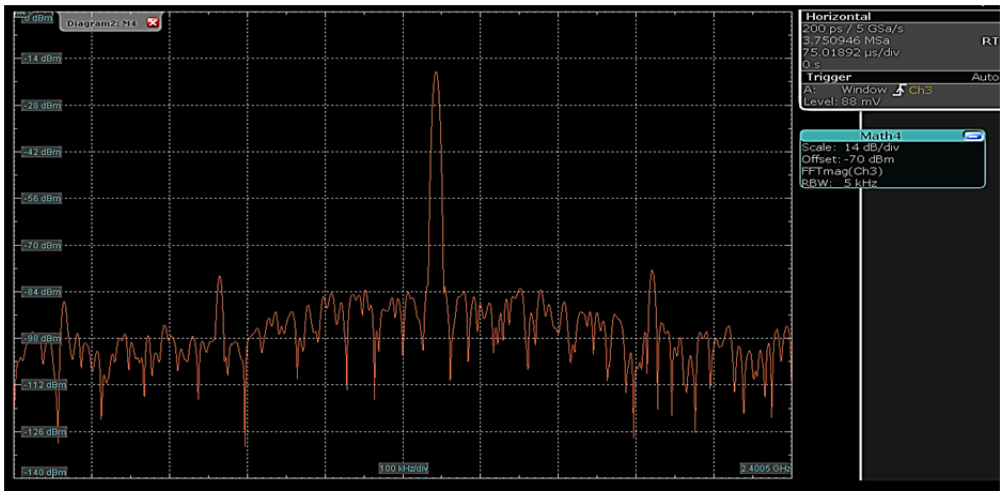

Figure 84. Antenna Channel 2 Frequency Domain Signal from Measurement Point 4

The post-processed data for the FMCW signal after sweeping the MWP DF system from −90° to +90° relative to the transmitting source is shown in Figure 85. Similar to Figure 70, for Figure 85, the signal amplitudes for the three channels were digitized to create three values, which formed a unique set that corresponded to a particular AOA from the transmission source. Based on [12], post analysis using the concept of a minimum-Euclidean distance detector for AOA estimation showed that the system was capable of detecting the AOA of FMCW signals with an RMS accuracy of 0.29°, as shown in Figure 86.

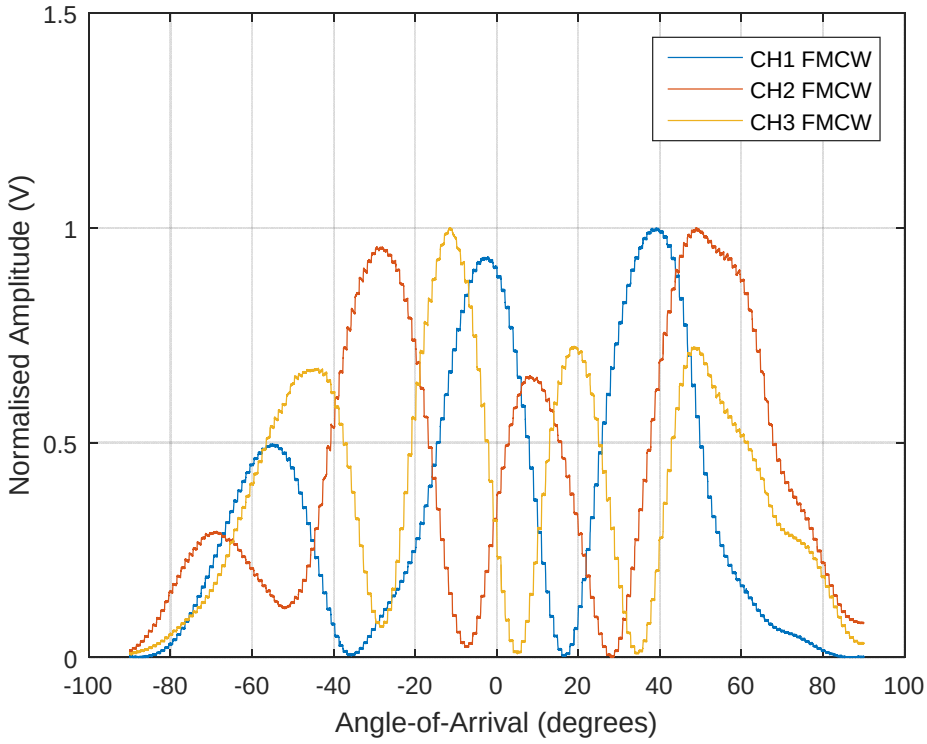

Figure 85. FMCW Data After Post Processing and Normalization. Source: [12].

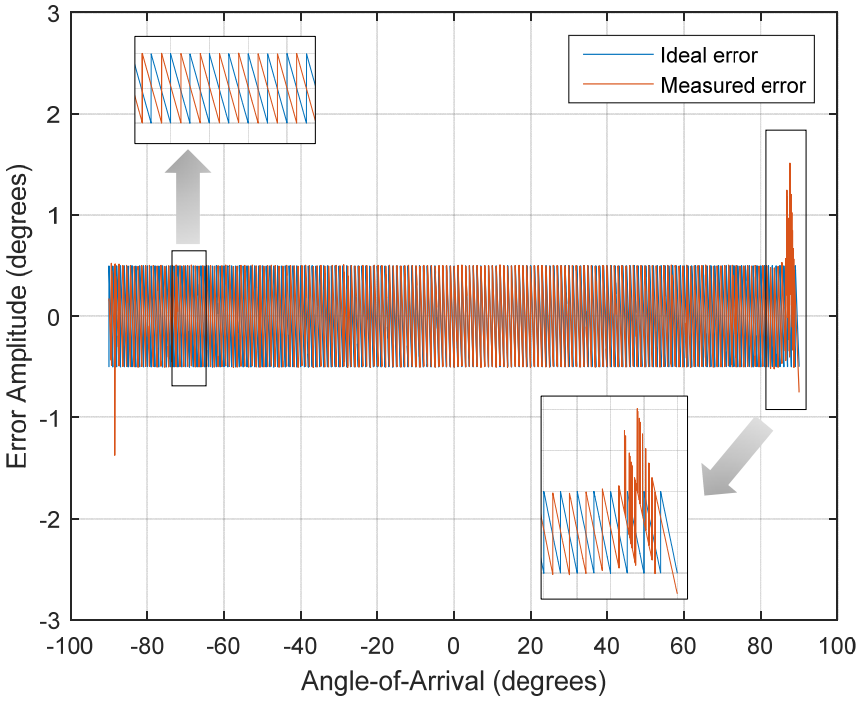

Figure 86. FMCW Signal Error Plot. Source: [12].

VIII. CONCLUDING REMARKS AND FUTURE CONSIDERATIONS

The hardware for the new MWP DF was ruggedized, and the system operates with much more stability as compared to the mock-up system from the previous design. With the detailed characterization of every component, and taking into consideration the cable and interconnection losses, each channel path was integrated in stages to ensure that the maximum performance of the system as a whole was obtained. Deliberate design considerations were made to group components by their functions and modularize them into four aluminum boxes. The modularized design allows the system to be transported easily, enhances the safety of operating the system, and expedites the troubleshooting process. In addition, the detailed investigation to establish the transfer function of the LNA cascade in the front-end allows tuning of the system gain to achieve maximum sensitivity during measurements.

As detailed in this investigation, the system was experimentally evaluated with continuous wave signals, FMCW and phase-coded P4 signals at 2.4 GHz in an anechoic chamber. It was demonstrated that the system is capable of detecting the FMCW centered at 2.4 GHz and varied within $\pm$ 100 kHz from transmit modulation bandwidth ΔF. It was demonstrated that the system is capable of determining P4 signal phase changes occurring every 500.0 ns; however, in the experimental evaluation, the system was unable to resolve the exact amount of phase variation. After post-processing was conducted, it was verified that the system is capable of estimating the AOA for an FMCW signal with an RMS error of 0.29° at a 1° resolution. For a P4-coded CW signal, the RMS error in estimating the AOA was 0.32° at a 1° resolution. In addition, the sensitivity of the system was measured to be -62.96 dBm.

The existing system was constructed using commercially available components, and the modular design was installed in four aluminum boxes for research and test purposes. While the size of the current system is much reduced as compared to the previous mock-up system, its size could be further reduced for possible deployment for miniature air vehicle applications in the future.

Furthermore, the current system only allows test signals to be transmitted in the frequency range of 2.2 GHz to 2.5 GHz due to the narrow operating frequency of the LNA 2700 and VVA ZX73-2500+. If both components are replaced with similar components having a wider frequency range, the system can be evaluated using multiple emitters transmitting at different frequencies.

The gain control for the system is currently achieved by varying the VVA to optimize the amplification of the incoming signals through the cascade of fixed gain LNAs. Calibration is required during each measurement to prevent the LNAs from operating in the 1-dB compression mode. In addition, the V_{bias} must be calibrated to ensure the DE-MZM operates at the linear region. These one-off calibrations are sufficient for controlled measurement in the anechoic chamber; however, for field testing, the environmental conditions are dynamic and unpredictable. It would be impossible to continue calibrating the system during measurements.

To overcome this challenge, the front-end design can be improved by incorporating two real-time feedback control loop circuits as recommended in Figure 87. First, the automatic gain control (AGC) loop could be used to maintain the amplified signals at a specified range regardless of the strength of the received signal [42]. Second, the V_{bias} control loop allows the bias voltage to be adjusted accordingly such that the DE-MZM always operates in the linear region.

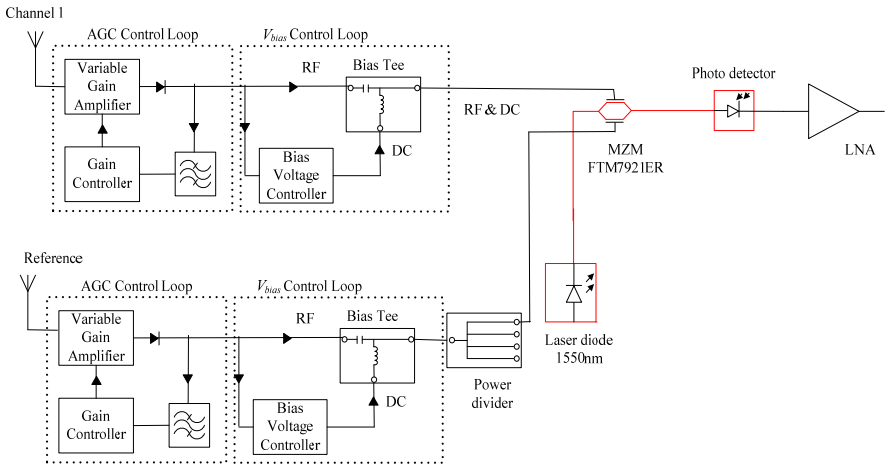

Figure 87. Automated Control Loops for Gain and V_{bias}

APPENDIX A. RECEIVED POWER COMPUTATION USING FRIIS EQUATION

The received power P_r at the antenna element can be computed using the one-way Friis equation given in (14). Several parameters were obtained either from data specifications or through actual measurements. Based on the data specifications, the gain of the transmission antenna and the gain of the receiving antenna are G_t = 5 dB and G_r =1.5 dB, respectively. The distance between the transmission antenna and receiving antenna was measured to be r = 5.7 m. The loss from to tranmistter to the antenna and the loss from receive antenna to receiver were measured to be L_t = 3 dB and L_r = 1.5 dB, respectively. Equation (14) can be expressed in terms of dB as

$$P_r\,(dBm) = P_t(dBm) + G_T(dB) + G_R(dB) + 10\log(\lambda^2) \\ -10\log(4\pi)^2 - 10\log(r^2) - L_t(dB) - L_r(dB). \tag{21}$$

If P_t is varied for a known wavelength λ of the transmitted signal, the received power P_r can be computed and plotted as shown in Figure 88. As seen from Figure 88, the test frequency of 2.4 GHz used in our measurements was plotted along with other frequencies for comparisons. As the test frequency increases, received power P_r decreases for a given transmit power P_t.

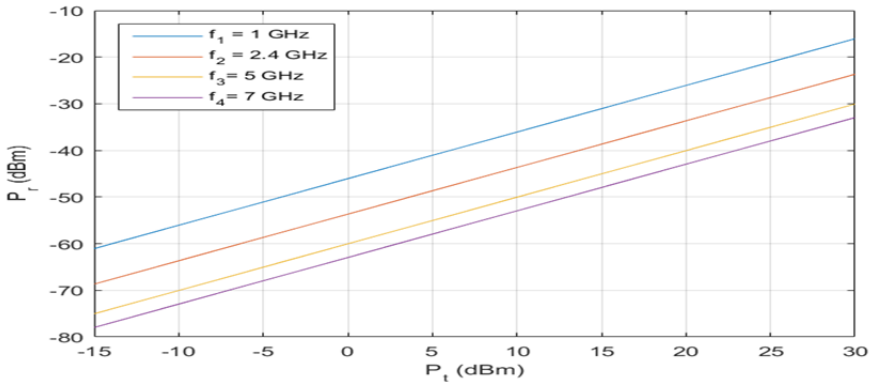

Figure 88. Received Power P_r versus Transmit Power P_t for Different Wavelengths λ

THIS PAGE INTENTIONALLY LEFT BLANK

APPENDIX B. SENSITIVITY OF MWP DF SYSTEM

The sensitivity of the MWP DF system can be expressed as [43]

$$\delta_R = kT_o F_{total} B_{Ri} \left(SNR_{Ri} \right) , \tag{22}$$

where $k =$ 1.38 x 10^{-23} J / K, T_o is the standard noise temperature (T_o = 290 K), F_{total} is the receiver noise factor, B_{Ri} is the input bandwidth of the receiver expressed in Hz, and SNR_{Ri} is the minimum signal-to-noise ratio required for detection at the receiver input. From (22), k and T_o are constants, B_{Ri} can be found using Table 12, and SNR_{Ri} can be measured in the anechoic chamber. As such, we need to establish the value of F_{total} .

The total noise factor F_{total} of the cascade system is determined from [44]

$$F_{total} = F_1 + \frac{F_2 - 1}{G_1} + \frac{F_3 - 1}{G_1 G_2} + \cdots + \frac{F_n - 1}{\sum_{i=1}^{n-1} G_i}, \tag{23}$$

where F_i denotes the noise factor and G_i is the gain of each individual stage. The F_{total} for the MWP DF system is established by modelling the front-end of the system as shown in Figure 89. If we refer to Figure 6, LNA 2700 is directly coupled to the antenna element; as a result, the first noisy network is LNA 2700 and not an RF cable assembly. The gain G_1 and F_1 for LNA 2700 were extracted from Figure 20 and Table 3, respectively. The gain G_2 is the insertion loss for VVA obtained from Table 6. The gain G_3 and F_3 for LNA 8G were obtained using Figure 21 and Table 3, respectively. The gain G_4 was determined from the insertion loss for the bias tee obtained from Figure 29.

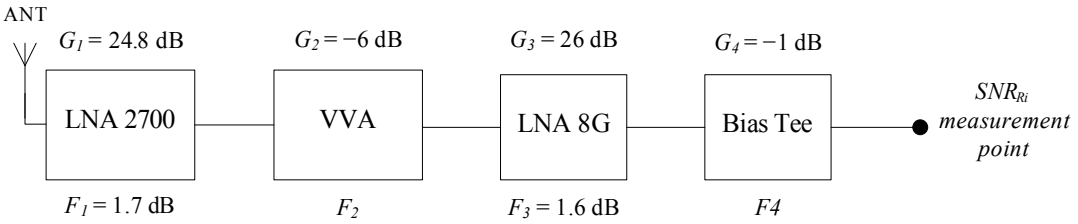

Figure 89. Cascade of LNAs and Bias Tee in Receiver

Although we do not have the data for F_2 and F_4, from (23), if G_1 is sufficiently large, F_{total} can be approximated to be F_1. Using $G_1 = 10^{(G_1\,dB/10)}$, we compute G_1 to be 301.9. If we assume $F_2 = 10$, the second term in (23) gives 0.029. The subsequent terms in (23) also result in a small value due to the high gain of G_1 and G_3. Using $F_1 = 10^{(F_1\,dB/10)}$, we compute F_1 to be 1.48. Therefore, $F_{total} \approx F_1 \approx 1.48$.

From Table 12, the bandwidth of the receiver B_{Ri} is approximately 300 MHz. The SNR_{Ri} in Figure 86 was measured to be 54.54 dBm, or 284.45 W, as shown in Figure 90. Substituting $k = 1.38 \times 10^{-23}$ J / K, $T_o = 290$ K, $F_{total} = 1.48$, $B_{Ri} = 300 \times 10^6$ Hz, and $SNR_{Ri} = 284.45$ into (22) gives $\delta_R = 5.05 \times 10^{-10}$ W, or $\delta_R = -62.96$ dBm.

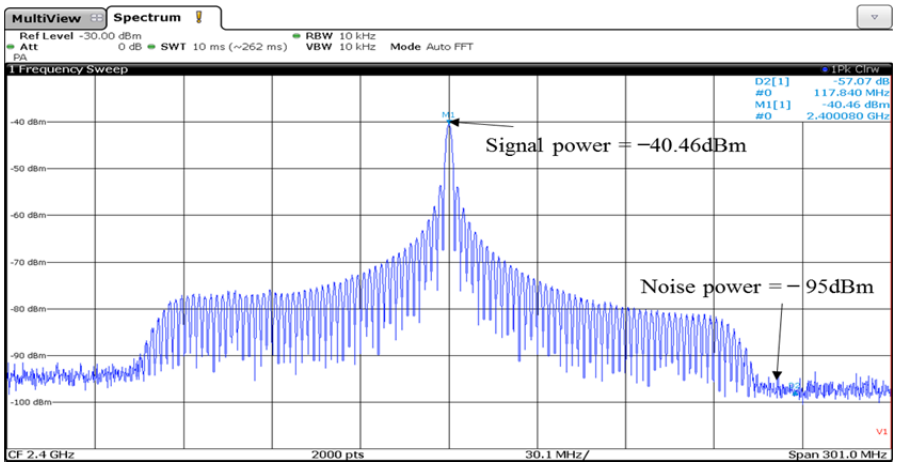

Figure 90. Minimum Discernable Signal and Relative Noise Power for Sensitivity Calculation

LIST OF REFERENCES

[1] R. M. Clark, "Passive RF," in *Intelligence Collection*, 1st ed., M. Ponce, Ed. London, UK: SAGE Publications Ltd., pp. 348–349, 2014.

[2] S. E. Lipsky, "DF receiver theory," in *Microwave Passive Direction Finding*, 2nd ed., Raleigh, NC: Sci. Tech Publishing, Inc., pp. 24–33, 2004.

[3] P. Hajiani, H. Habibi, M. Hakkak, and F. Mazlumi, "Accuracy in wideband direction of arrival system," in *Int. Symp. Electromagnetic Compatibility,* Qingdao, China, Oct. 2007, pp. 394–397.

[4] P. E. Pace, D. Wickersham, D. C. Jenn, and N. S. York, "High-resolution phase sampled interferometry using symmetrical number systems," *IEEE Trans. on Antennas and Propagation,* vol. 49, Oct. 2001, pp. 1411–1423.

[5] S. E. Lipsky, "Interferometer DF techniques," in *Microwave Passive Direction Finding*, 2nd ed., Raleigh, NC: Sci. Tech Publishing, Inc., pp. 167–170, 2004.

[6] J. Yao, "Microwave Photonics," *J. Lightwave Technol.,* vol. 27, Feb. 2009, pp. 314–335.

[7] S. A. Pappert and B. Krantz, "RF photonics for radar front-ends," in *IEEE Radar Conf.,*Boston, MA, Apr. 2007, pp. 965–970.

[8] M. E. Manka, "Microwave photonics for electronic warfare applications," in *International Topical Meeting on Microwave Photonics,* Gold Coast, Qld, Oct. 2008, pp. 275–278.

[9] R. W. Ridgway, J. A. Conway, and C. L. Dohrman, "Microwave photonics: Recent programs at DARPA," in *International Topical Meeting on Microwave Photonics,* Alexandria, VA, Oct. 2013, pp. 286–289.

[10] T. W. Tedesso, J. Calusdian, C. Sewing, and P. E. Pace, "Wideband direction finding using a photonic robust symmetrical number system technique," *Optical Engineering, OPTICE,* vol. 53, Nov. 2014, pp. 1–13.

[11] R. Humeur, "A new high-resolution direction finding architecture using photonics and neural network signal processing for miniature air vehicle application." M.S. thesis, Inform. Warfare Syst. Eng., NPS, Monterey, CA, p. 62, Sep. 2015.

[12] C. K. Ong, "Microwave-Photonic Architecture for Direction Finding of LPI Emitters: Post-Processing for Angle of Arrival Estimation," M.S. thesis, Elect. Eng., NPS, Monterey, CA, Sep. 2016.

[13] E. Jacobs and E. W. Ralston, "Ambiguity resolution in interferometry," *IEEE Trans. Aerosp. Electron. Syst.,* vol. AES-17, Nov. 1981, pp 766-780.

[14] W. L. Stutzman, G.A Thiele, "Monopoles and image theory," in *Antenna Theory and Design*, 3rd ed., W. Ashenberg, Ed. Hoboken, NJ: John Wiley & Sons, p. 75, 2012.

[15] W. A. U. Titze, P. V. Brennan, and R. Benjamin, "The single channel interferometer using a pseudo-doppler direction finding system," *IEEE Trans. Acoust.,Speech, Signal Process.,* vol. 142, Jun. 1995, pp. 130–136.

[16] SMW200A signal vector generator. (n.d.) Rohde & Schwarz. [Online]. Available: https://www.rohde-schwarz.com/us/product/smw200a-productstartpage_63493-38656.html [Accessed: 28 Jul. 2016]

[17] ESW EMI test receiver." (n.d.) Rohde & Schwarz. [Online]. Available: https://www.rohde-schwarz.com/us/product/esw-productstartpage_63493-121280.html. [Accessed: 28 Jul. 2016]

[18] RTO2000 digital oscilloscope. (n.d.) Rohde & Schwarz. [Online]. Available: https://www.rohde-schwarz.com/us/product/rto-productstartpage_63493-10790.html. [Accessed: 28 Jul. 2016]

[19] SMA male to SMA male precision cable 36-inch length using 160 series coax, RoHS, Rev. 1.1. (2014). Pasternack. [Online]. Available: https://www.pasternack.com/images/ProductPDF/PE300-36.pdf. [Accessed: 20 Jul. 2016]

[20] Coaxial cable 141 model series, 141-3SM+ datasheet, Rev. A. (n.d.) Mini-Circuits. [Online]. Available: https://www.minicircuits.com/pdfs/141-3SM+.pdf. [Accessed: 20 Jul. 2016]

[21] Coaxial cable 141 model series, 141-6SM+ datasheet, Rev. A.(n.d) Mini-Circuits. [Online]. Available: https://www.minicircuits.com/pdfs/141-6SM+.pdf. [Accessed: 20 Jul. 2016]

[22] K. B. Schaub, J. Kelly, " Chapter 6: Fundamentals of Analog and Mixed-Signal Testing," in *Production Testing of RF and System-on-a-chip Devices for Wireless Communications*, 1st ed. Norwood, MA: Artech House, pp. 166-167, 2004

[23] M. Golio, "Chapter 1.5.1: Low noise amplifier," in *RF and Microwave Passive and Active Technologies*, 2nd ed., M. Golio and J. Golio, Eds. Boca Raton, FL: CRC Press, p. 17, 2008.

[24] LNA series 2200 – 3200MHz low noise amplifier, LNA-2700 datasheet. (Jan. 2006) RF Bay Inc. [Online]. Available: http://rfbayinc.com/products_pdf/product_109.pdf. [Accessed: 2 Aug. 2016]

[25] LNA series 1-8GHz low noise amplifier, LNA-8G datasheet. (Jan. 2006) RF Bay Inc. [Online]. Available: http://rfbayinc.com/products_pdf/product_122.pdf. [Accessed: 2 Aug. 2016]

[26] D. M. Pozar, "Chapter 10: Noise and nonlinear distortion," in *Microwave Engineering linear Distortion*, 4th ed., A. Melhorn, Ed. Hoboken, NJ: John Wiley & Sons, pp. 512–513, 2012.

[27] Voltage variable attenuator, ZX73-2500+ datasheet, Rev. B. (n.d) Mini-Circuits. [Online]. Available: http://www.minicircuits.com/pdfs/ZX73-2500.pdf. [Accessed: 5 Aug. 2016]

[28] Bias-tee wideband 300-3500MHz, ZFBT-352-FT+ datasheet, Rev. A (n.d) Mini-Circuits. [Online]. Available: https://www.minicircuits.com/pdfs/ZFBT-352-FT+.pdf. [Accessed: 5 Aug. 2016]

[29] 4-way high power broadband combiner from1GHz to 6GHz, PE20S0014 datasheet, Rev 1.1 (2015). Pasternack. [Online]. Available: https://www.pasternack.com/images/ProductPDF/PE20S0014.pdf. [Accessed: 5 Aug. 2016]

[30] V. J. Urick, K. J. Williams, and J. D. McKinney, "External intensity modulation with direct detection," in *Fundamentals of Microwave Photonics*, 1st ed. Hoboken, NJ: John Wiley & Sons, pp. 214–215, 2015.

[31] T. Nakazawa, "Low drive voltage and broad-band $LiNbO_3$ modulator," in *International Topical Meeting on Microwave Photonics,* Awaji-Yumebutai, Japan, Nov. 2002, pp. 45–48.

[32] J. E. Toney, "Introduction," in *Lithium Niobate Photonics*, 1st ed. Norwood, MA: Artech House, pp. 5–6, 2015.

[33] O. Mitomi, K. Noguchi, and H. Miyazawa, "Broadband and low driving-voltage $LiNbO_3$ optical modulators," *IEEE Proc.—Optoelectronics,* vol. 145, Dec. 1998, pp. 360–364.

[34] S. Iezekiel, "Microwave photonics—An introductory overview," in *Microwave Photonics: Devices and Applications*, 1st ed., S. Iezekiel, Ed. Chippenham, Wiltshire: John Wiley & Sons, pp. 16–19, 2009.

[35] Dual drive 10Gb/s LN modulator with monitor PD, FTM7921ER data sheet, Edition 1.1. (Jun. 2002). Fujitsu, [Online]. Available: http://www.lightwavestore.com/product_datasheet/OSC-MOD-10Gb-016C_pdf1.pdf. [Accessed: 8 Aug. 2016]

[36] W. L. Stutzman, G.A Thiele, “Radiation Patterns,” in Antenna Theory and Design, 3rd ed., W. Ashenberg, Ed. Hoboken, NJ: John Wiley & Sons, p. 43, 2012.

[37] R. G. Wiley, “ELINT implications of range equations and radar constraints,” in *ELINT the Interception and Analysis of Radar Signals.* Norwood, MA: Artech House, pp. 9-10, 2006.

[38] P. E. Pace, “Phase shift keying techniques,” in *Detecting and Classifying Low Probability of Intercept Receiver*, 2nd ed. Norwood, MA: Artech House, pp. 157–162, 2009.

[39] P. E. Pace, “FMCW radars,” in *Detecting and Classifying Low Probability of Intercept Receiver*, 2nd ed. Norwood, MA: Artech House, pp. 86–90, 2009.

[40] S. O. Piper, “Receiver frequency resolution for range resolution in homodyne FMCW radar,” in *Proc. Nat. Telesystems Conf., Commercial Applications and Dual-use Technol.,* 1993, pp. 169–173.

[41] S. O. Piper, “Homodyne FMCW radar range resolution effects with sinusoidal nonlinearities in the frequency sweep,” in *Record of the IEEE Int. Radar Conf.,* 1995, pp. 563–567.

[42] A. Golden, “Analytical Models of Tracking Radars,” in *Radar Electronic Warfare*, 1st ed. Washington, DC: AIAA Education Series, pp. 190-192, 1984

[43] P. E. Pace, “FMCW radars,” in *Detecting and Classifying Low Probability of Intercept Receiver*, 2nd ed. Norwood, MA: Artech House, pp. 86–90, 2009.

[44] D. M. Pozar, “Chapter 13: Introduction to Microwave Systems,” in *Microwave Engineering linear Distortion*, 4th ed., A. Melhorn, Ed. Hoboken, NJ: John Wiley & & Sons, pp. 652–654, 2012.

INITIAL DISTRIBUTION LIST

1. Defense Technical Information Center
   Ft. Belvoir, Virginia

2. Dudley Knox Library
   Naval Postgraduate School
   Monterey, California